

## REPORT DOCUMENTATION PAGE

Form Approved  
OMB No. 074-0188

Public reporting burden for this collection of information is estimated to average 1 hour per response, including the time for reviewing instructions, searching existing data sources, gathering and maintaining the data needed, and completing and reviewing this collection of information. Send comments regarding this burden estimate or any other aspect of this collection of information, including suggestions for reducing this burden to Washington Headquarters Services, Directorate for Information Operations and Reports, 1215 Jefferson Davis Highway, Suite 1204, Arlington, VA 22202-4302, and to the Office of Management and Budget, Paperwork Reduction Project (0704-0188), Washington, DC 20503

**NSN 7540-01-280-5500**

**Standard Form 298 (Rev. 2-89)**  
Prescribed by ANSI Std. Z39-18  
**298-102**

20000720 121

Annual Technical Report  
December 1, 1999

## Critical Factors for the Transition from Chromate to Chromate-Free Corrosion Protection

PP-1119  
ARO contract number DACA72-99-C-0002.

A research program conducted by:

The Ohio State University  
Air Force Research Laboratory  
Army Research Laboratory



For:

The Strategic Environmental Research and Development Program



## Table of Contents

Investigator Contacts	2
Project Background	3
Project Objective	4
Overall Project Approach	5
Project Subtasks and Accomplishments:	
<b>Copper Dissolution Phenomena in Al-Cu and Al-Cu-Mg Alloys,</b> R. Boger, R.G. Buchheit, M. Donohue, Ohio State University.	6
<b>Corrosion Resistant Coatings for 2XXX Aluminum Alloys and the Electrochemical Characterization of the S Phase,</b> R.G. Buchheit J. L. Searles, Ohio State University.	15
<b>Influence of Chromate on the Corrosion Behavior of Aluminum Alloys,</b> Q. Meng,, G.S. Frankel, Ohio State University. (24-30)	25
<b>Formation of Chromate Conversion Coatings on Mixed Phases, of Al/Cu/Mg Alloys</b> W. McGovern, R.G. Buchheit, R. L. McCreery, Ohio State University (31-42)	31
<b>Measurement of Intermetallic Electrochemistry,</b> A. Sehgal, R. Leard, R.G. Buchheit, Ohio State University (43-45)	42
<b>Thermal Stability and Aging Characteristics of Chromate Conversion Coatings on Aluminum Alloy 2024-T3,</b> V.N. Laget <sup>†</sup> , C. Jeffcoate <sup>††</sup> , H.S. Isaacs <sup>††</sup> , R.G. Buchheit <sup>†</sup> , <sup>†</sup> Ohio State University, and <sup>††</sup> Brookhaven National Laboratories. (46-54)	46
<b>Vibrational Spectroscopy of Chromate Coatings for Both Characterization and Nondestructive Evaluation,</b> J. Wu, R.L. McCreery, R. G. Buchheit, <sup>†</sup> Department of Chemistry, <sup>††</sup> Department of Materials Science and Engineering, Ohio State University.	55
<b>Life Prediction Tools for Corrosion Protection,</b> M.S.Donley, N.N.Voevodin, AFRL/MLBT, Air Force Research Laboratory	66
<b>Advanced Diagnostics,</b> J.H. Beatty, P.F. Buckley, Metals and Ceramics Research Branch, Weapons and Materials Research Directorate, Army Research Laboratory	80

## Investigator Contacts

John H. Beatty (co-PI)  
Metals & Ceramics Branch Chief  
Weapons and Materials Research Directorate  
Attn: AMSRL WM-MC  
John Beatty  
Bldg. 4600  
Aberdeen Proving Ground, MD 21005  
(410) 306-0869 Tel.  
(410) 306-8029 FAX  
jbeatty@arl.mil

Rudolph G. Buchheit (PI)  
Associate Professor  
Ohio State University  
Department of Materials Science and Eng.  
477 Watts Hall  
2041 College Rd.  
Columbus, OH 43210  
(614) 292-6085 Tel.  
(614) 292-9857 FAX  
buchheit.8@osu.edu

Paul Buckley  
Corrosion Team Leader  
Army Research Laboratory  
Attn: AMSRL-WM-MC  
Paul Buckley  
Bldg. 4600  
Aberdeen Proving Ground, MD 21005  
pbuckley@arl.mil  
(410) 306-0848 Tel.

Michael S. Donley (co-PI)  
Coatings Team Leader  
AFRL/MLBT  
Bld. 654 2941 P Street  
Wright Patterson AFB, OH  
(937) 255-6485 Tel.  
(937) 255-2176 FAX  
donleysm@ml.wpafb.af.mil

Cindy Flores  
FCC Administrative Associate  
Ohio State University  
Department of Materials Science and Eng.  
477 Watts Hall  
2041 College Rd.  
Columbus, OH 43210  
(614) 292-9857 Tel.  
(614) 292-9857 FAX  
flores.1@osu.edu

Gerald S. Frankel (co-PI)  
Associate Professor  
Ohio State University  
Department of Materials Science and Eng.  
477 Watts Hall  
2041 College Rd.

Columbus, OH 43210  
(614) 688-4128 Tel.  
(614) 292-9857 FAX  
frankel.10@osu.edu

Hamish L. Fraser (co-PI)  
Professor  
Ohio State University  
Department of Materials Science and Eng.  
477 Watts Hall  
2041 College Rd.  
Columbus, OH 43210  
(614) 292-2708 Tel.  
(614) 292-1537 FAX  
fraser.3@osu.edu

Valerie Laget  
Post-Doctoral Researcher  
Ohio State University  
Department of Materials Science and Eng.  
477 Watts Hall  
2041 College Rd.  
Columbus, OH 43210  
(614) 292-1694 Tel.  
(614) 292-9857 FAX  
laget.1@osu.edu

Richard L. McCreery (co-PI)  
Professor  
Ohio State University  
Department of Chemistry  
1118 Newman & Wolfram  
100W 18<sup>th</sup> Ave.  
Columbus, OH 43210  
(614) 292-2021 Tel.  
(614) 292-1685 FAX  
mccreery.2@osu.edu

Akshey Sehgal  
Post-Doctoral Researcher  
Ohio State University  
Department of Materials Science and Eng.  
477 Watts Hall  
2041 College Rd.  
Columbus, OH 43210  
(614) 292-1694 Tel.  
(614) 292-9857 FAX  
sehgal.9@osu.edu

Natalia N. Voevodina  
Technical Staff  
WL/MLBT  
Bldg. 654 2941 P Street  
Wright Patterson AFB, OH 45433-7750  
(937) 255-5161 (Tel.)  
(937) 255-2176 (FAX)  
voevodnn@wl.wpafb.af.mil

## **Project Background**

The Department of Defense (DOD) and Department of Energy (DOE) have committed to replace chromate-based metal finishing in present and next generation systems. At issue is whether this change will occur in a timely manner without performance or cost penalties that could compromise operational readiness. Additionally, undue delay in determining and implementing new corrosion protection practices poses enormous risk for existing assets. Faced with the request from the user community for chromate-free corrosion protection, the coatings science and technology community has been unable to deliver. This situation exists, in part, because chromate corrosion protection has some rare, and perhaps unique attributes. It also exists because chromates have been used on many different metals and alloys in a vast range of applications. Consequently, the understanding of chromate corrosion protection is broad but, arguably, not deep. The chromate-replacement problem has clearly exposed the lack of depth in our understanding. For example, we cannot account for, or predict in any quantitative way, the effect of alloy-to-alloy microstructural variations in the effectiveness of chromate or chromate-free corrosion protection. We do not understand how to duplicate self-healing action thought to be key in chromate corrosion protection. We do not understand the range in performance exhibited by chromate coatings as applied in the field. We do not have a suite of test methods that permit quantitative, discriminating, and predictive evaluation suitable for both chromate and chromate-free corrosion protection. Sound, strategic investments in chromate elimination research and development have been made, but these issues require special attention to successfully cross the chromate-free corrosion protection threshold. This proposal is offered as an attempt to address these issues in a way that will permit timely and effective chromate replacement without risk to valuable assets.

## **Project Objective**

The overall objective of this research program is to acquire a fundamental understanding of the chemical and physical processes and mechanisms of corrosion protection by chromate-based coatings applied to metal surfaces with a specific focus on corrosion protection of aluminum alloys. The key functional attributes of chromate coating formation and breakdown must be identified and understood so that ultimately, they might be duplicated using environmentally friendly corrosion protection methods. Environmentally friendly corrosion protection methods must be found to replace chromate corrosion protection methods because environmental regulations are forcing elimination of products and processes (like chromates) whose formulations use or produce toxic substances. Specific objectives of this program are 1) to define as far as possible a set of phenomenological and fundamental rules that describe the role of microstructural heterogeneity in chromate conversion coating formation and breakdown, 2) to define the relationship between chromate conversion coating structure and chemistry, and coating properties for coatings applied under non-ideal conditions such as those that exist during coating applications in manufacturing and military maintenance depot environments, 3) determine the extent to which application method, coating age, and alloy substrate chemistry affect the self-healing nature of chromate coatings, 4) develop rapid, quantitative, and predictive tests to assess properties and performance of chromate conversion coatings. It is a further objective to work interactively with the AFOSR-sponsored MURI which also examines fundamental aspects of corrosion inhibition by chromates.

## Overall Project Approach

This program comprises a four year fundamental research effort conducted jointly by Ohio State University, the Air Force Research Laboratory, and the Army Research Laboratories. Informal technical collaborations are planned with the Air Force Corrosion Program Office, the Aluminum Company of America - Alcoa Technical Center, and the Naval Air Defense Center. Research activities are focussed in three topical areas.

The first research activity focuses on the role of microstructural heterogeneity in the alloy substrate on chromate conversion coating formation and breakdown. The approach for adding new insight to the fundamental understanding of corrosion inhibition of al alloys is to examine and characterize the interaction of important Al-based intermetallic compounds with key coating process chemistries and service environments. Two general experimental approaches will be used in this regard. First, intermetallic compounds will be synthesized in bulk form for characterization by conventional electrochemical and surface analytical techniques. Second, small length scale probes will be used to interrogate coating formation and breakdown processes at relevant microstructural length scales (0.5 to 10  $\mu\text{m}$ ). Small length scale probing techniques that will be used include atomic force microscopy, confocal scanning Raman spectroscopy, and scanning Auger microscopy. These probes will reveal information. This multifaceted approach will ensure that an accurate mechanistic picture is developed for the role of microstructural heterogeneity in coating formation and breakdown.

The second research activity focuses on the relationship between coating structure, chemistry with coating properties and performance when the coating suffers from non-idealities such as advanced age, exposure to conditions that subsequently impair coating corrosion resistance mechanisms, (such as exposure to ultraviolet light), or less-than-ideal application methods. These effects will be studied by examining coatings returned from the field after service and by simulated exposure testing under controlled conditions. Analysis of field return samples will permit bounds to be established on degree of structural and chemical change, as well as on the changes in coating performance. The use of samples subjected to controlled, accelerated exposures will permit quantitative relationships to be established between structure-chemistry and properties-performance.

The third research activity focuses on development of rapid, quantitative, and predictive tests to measure corrosion protection. The approach is based on the use of electrochemical methods, like electrochemical impedance spectroscopy and electrochemical noise to quantitatively detect the onset of chromate coating breakdown. These quantitative assessments will form the basis for rapid, predictive methods for determining coating performance and life. They will also be used to test the effects of environmental factors such as oxygen availability, chloride ion concentration, temperature and pH on coating degradation processes. Finally, results from these test methods will be statistically correlated to test from incumbent test technologies to facilitate the transition from old to new coating evaluation methods.

This report describes technical activities conducted between March 1, 1999 and December, 1, 1999.

## Copper Dissolution Phenomena in Al-Cu and Al-Cu-Mg Alloys

R.G. Buchheit, R.K. Boger, M.W. Donohue, Department of Materials Science and Engineering, Ohio State University, 477 Watts Hall, 2041 College Rd., Columbus, OH 43210. Tel. (614) 292-6085, FAX (614) 292-9857, buchheit.8@osu.edu.

### Abstract

In this study, rotating ring-disk electrode collection of Cu was conducted using corroding Al-Cu and Al-Cu-Mg alloy disks. These experiments were conducted to determine how strongly Cu release depends on the volume fraction of Cu-rich intermetallic compounds (IMCs) in the alloy. Alloy disks were subject to galvanostatic polarization for 1.5 hours in aerated chloride solutions. Collection experiments were conducted with alloy disks of different Cu concentrations and various heat treatments to produce different volume fractions of IMCs. Results showed that Cu release is detected from solution heat treated and quenched alloys indicating that dissolution of the matrix phase releases Cu. Underaging Al-Cu alloys increases the amount of Cu released slightly, and increases the variance in the amount of Cu collected in replicate measurements significantly. Further aging reduce the extent of Cu release. Overall, in these experiments, Cu release is not dominated by IMC dissolution, but rather is determined primarily by the Cu concentration in the matrix phase.

### Introduction

During corrosion of Al-Cu and Al-Cu-Mg alloys, Cu is often observed to be redistributed across an alloy's surface. An example of this is shown in Figure 1, which is a pit formed on a conversion coated 2024-T3 alloy surface after 168 hours of exposure to a 5% salt fog (1). During exposure, solution condensed and flowed across the surface resulting in a corrosion product "tail" downstream from the pit. The corrosion product contains copper in both the oxidized and metallic form. Cu redistribution can also be observed at smaller length scales. Figure 2 shows a backscattered electron image and a companion elemental Cu map of a polished 2024-T3 surface exposed to aerated 0.1 M NaCl solution for 4 hours (1). Pitting is observed around many of the second phase particles, and some of the particles appear to be selectively dissolved. Cu is dispersed around pits where particles appear to be selectively dissolved (center right) indicating redistribution of Cu.

These morphologies suggest that corrosion liberates Cu, which is subsequently reduced or precipitated at other locations. While it is expected that Cu ions would plate-out onto aluminum, how Cu ions can be generated by a corrosion process that is occurring hundreds of millivolts negative of the reduction potential for Cu is less clear.

Recent observations have shown that Cu-rich intermetallic compound (IMC) particles in Al-Cu and Al-Cu-Mg alloys vigorously dealloy in aerated chloride solutions, triggering Cu release (1,2,3). Observations suggest that the porous structure of dealloyed particles decomposes, probably driven by surface energy minimization, causing the formation Cu clusters that are detached from the remnant particle (Figure 3) (1). These clusters are then carried away from the surface by mechanical action of flowing solution or hydrous corrosion product growth. Once the clusters are mechanically detached from the alloy, they are electrically isolated and are no longer constrained to be at the very active corrosion potential of the alloy. In aerated solutions, it is possible that the Cu clusters attain potentials characteristic of the corrosion potential of Cu, which is more positive than the Cu reduction potential. Under these conditions, electrochemical dissolution of the clusters to form Cu ions can occur. The overall Cu release process based on these observations and ideas is shown schematically in Figure 4 (1).

Such a mechanism suggests that Cu release during alloy corrosion is strongly influenced by dealloying and dissolution of Cu-rich IMCs. However, Cu is partitioned into IMCs and into the matrix phase in proportions that are determined by overall alloy Cu concentration and heat treatment. All phases may contribute to Cu release to differing degrees based on their dissolution characteristics, Cu content, and area fraction on the alloy surface. Therefore, the objective of this study was to examine the relative contributions of the matrix phase and IMCs to Cu release during rotating ring-disk collection experiments, and to determine if Cu release from IMCs is the dominant release mode during alloy corrosion.

## Experimental Procedures

**Materials.** Aluminum alloy disk electrodes were prepared from 0.25 inch thick Al-3.98%Cu (referred to as Al-4Cu) sheet, Al-0.2%Cu sheet (referred to as Al-0.2Cu), and from 0.125 inch thick 2024-T3 (Al-4.4Cu-1.5Mg-0.6Mn) sheet. Properly sized disk electrodes were cut from the sheet by electrodischarge machining. Al-4Cu disks were solution heat treated (SHT) at 540°C for 45 minutes then quenched in water. Certain samples were then artificially aged at 190°C for either 12 hours to produce an underaged (UA) temper, or 24 hours to produce a peakaged (PA) temper. To suppress unintended precipitation, all samples were stored at 0° to -5°C except during testing and artificial aging. The samples prepared from 2024-T3 were solution heat treated using the procedures described above. Certain samples were aged at 190°C for either 9 (UA temper), or 16 hours (PA temper).

**Rotating Ring-Disk Collection Experiments.** A rotating ring disk apparatus was used for Cu collection. The rotating arbor, constructed of Teflon™, accommodated a disk, which was an aluminum alloy of the types described above, and a platinum ring. The arbor was rotated at a constant rate of 105 rad/s, and all collection experiments were conducted in

aerated 0.5M NaCl solution. The ring and disk were controlled by separate potentiostats. The disk was controlled using a Princeton Applied Research (PAR) Model 263 potentiostat with a floating working electrode. The ring was controlled using a PAR Model 273 potentiostat with a grounded working electrode. Both potentiostats were operated remotely via computer and software control.

An identical collection protocol was used for all experiments. The disk was galvanostatically polarized at  $10 \mu\text{A}/\text{cm}^2$  for 5400s (1.5 h) to induce alloy dissolution, and Cu was collected at the ring, which was held potentiostatically at  $-0.600\text{V}_{\text{sce}}$ . Oxygen reduction was also occurring on the disk adding to the dissolution current. Cathodic polarization measurements indicated a mass transport-limited reaction rate of  $30\mu\text{A}/\text{cm}^2$ . Therefore the total dissolution current was estimated to be  $40 \mu\text{A}/\text{cm}^2$ .

After collection, the solution was sparged with nitrogen until the ring current dropped to about  $1 \mu\text{A}/\text{cm}^2$ . At that point, Cu was stripped from the ring by sweeping the potential from  $-1.2\text{V}_{\text{sce}}$  to  $+1.2\text{V}_{\text{sce}}$  at a scan rate of 100 mV/sec. The stripping voltammogram for Cu from Pt is characterized by three peaks Figure 5 (4, 5). The area under each of peaks in the current versus time plot was integrated, subtracting the background current, then added to obtain the charge associated with Cu collection. This charge was then divided by the total charge passed on the disk due to dissolution ( $Q_{\text{ring}}/Q_{\text{disk}}$ ).

## Results and Discussion

Copper was collected from all alloys and all heat treatment conditions examined including SHT Al-0.2Cu and Al-4Cu. This indicates that Cu release is not restricted to intermetallic compounds, and Cu can be released by dissolution of the matrix phase in relatively pure alloys (Al-0.2Cu). Multiple  $Q_{\text{ring}}/Q_{\text{disk}}$  measurements were collected for each alloy-heat treatment combination, and data sets with larger populations of replicate measurements exhibited Weibull distributions. Probability plots were constructed to illustrate the effects of alloy Cu content and heat treatment on Cu release.

Figure 6 is a probability plot showing the distribution of  $Q_{\text{ring}}/Q_{\text{disk}}$  measurements for SHT Al-0.2Cu, SHT Al-4Cu, and UA Al-4Cu. Two important observations can be made. First, for SHT alloys, Cu release scales with Cu concentration. Comparison shows that considerably more Cu is collected from Al-4Cu than from Al-0.2Cu. Second, upon artificial aging the variation in Cu release increases. In these plots, decreasing slope indicates increased variation in the measurement population. Artificial aging induces  $\theta$  phase ( $\text{Al}_2\text{Cu}$ ) precipitation and introduces at least one other pathway for Cu release beside matrix dissolution; namely dealloying of the  $\theta$  IMCs. The reason for increase in Cu release variation is not yet clear, but it may reflect the stochastic nature of localized dissolution associated with  $\theta$  particles. For example, in Figure 2 it is clear that some

second phase particles are selectively dissolved releasing Cu, while others of the same chemical type remain intact and presumably do not release as much Cu. While it may be argued that attack in the SHT alloys is also localized, examination of post-exposure optical micrographs suggests that attack is much more uniform on the SHT materials than artificially aged ones (Figure 7 and 8).

Figure 9 is a probability plot showing the distribution of  $Q_{ring}/Q_{disk}$  measurements for Al-4Cu in solution heat treated (SHT), underaged (UA), and peak aged (PA) conditions. A data set combining measurements from 2024 in SHT, UA and PA conditions is also given. Immediately, it is obvious that the slopes for the artificially aged samples are lower than that for SHT Al-4Cu indicating increased variance in the Cu release measurements. It is also evident that the extent of Cu release from Al-4Cu decreases from the underaged to peakaged condition. The trend in Al-4Cu samples suggests that Cu release is decreased as the volume fraction of  $\theta$  phase particles increases (and the matrix Cu content decreases) implying that IMCs can have the effect of binding Cu and prohibiting its release. Cu release decreases further for the combined set of measurements from 2024 samples. Alloy 2024 has 4.4 % Cu, which is slightly more than the Al-4Cu samples. However, some of this Cu is segregated into large constituents during solidification. A fraction of these constituents also contain Fe and Mn, which is known to bind Cu and prevent it from redissolving during solution heat treatment (6). It is possible that the high fraction of constituents in this alloy, some of which are Cu, Fe, Mn-bearing IMCs, may lower the matrix Cu content sufficiently to suppress Cu release compared to Al-4Cu alloys. It is also interesting to note that Cu release data for solution heat treated, underaged and peak aged 2024 all fall along the same fitted line. This behavior indicates that artificial aging has a negligible impact on Cu release in comparison to the effects imposed by the constituent particle population.

The sum of these results clearly shows that matrix dissolution is an important pathway for Cu release in Al-Cu-(Mg) alloys. The effect of Cu-rich IMCs on Cu release is detectable in these experiments as an increase in the variance in replicate measurements. However, the presence of IMCs does not control the “global” Cu release response.

As a cautionary note, it should be recognized that these collection experiments were conducted for relatively long times (1.5 hours) under conditions of forced convection. That the global Cu release response scales with the Cu concentration of the largest volume fraction phase (the matrix phase) is not surprising. Under other exposure conditions, namely short exposure times or quiescent solutions, IMC Cu release may become the dominant component of overall release. Additionally, relevance of these measurements to Cu release and redistribution over the short length scales associated with discrete pits remains to be determined.

## Summary

RRDE collection of Cu from corroding Al-Cu-Mg alloy disks shows that Cu ions are produced even though the corrosion process is occurring hundreds of millivolts negative of the reduction potential for Cu. This result is in agreement with earlier studies that showed Cu release from corrosion of bulk IMCs at very active potentials (3). Cu release is detected for solution heat treated and quenched alloys indicating Cu dissolution from solid solution phases. In general, the amount of Cu collected scales with the Cu concentration in the alloy. The amount of Cu collected is slightly increased by heat treating to the underaged condition, which probably reflects a contribution to Cu release from IMCs. However, further aging reduces the extent of Cu release. Under these experimental conditions, Cu release is more strongly influenced by overall alloy Cu concentration than by volume fraction of Cu-rich IMCs.

## References

- 1) R.G. Buchheit, P.F. Hlava, B. McKenzie, G.L. Zender, *J. Electrochem. Soc.*, 144, 2610 (1997).
- 2) R.G. Buchheit, L.P. Montes, M.A. Martinez, J. Michael, P.F. Hlava, *J. Electrochem. Soc.*, to be published, December (1999).
- 3) R.G. Buchheit, M.A. Martinez, L.P. Montes, *J. Electrochem. Soc.*, to be published, January (2000).
- 4) B.H. Vassos, H.B. Mark, Jr., *Electroanal. Chem. and Interf. Electrochem.*, 13, 1 (1967).
- 5) L.M. Abrantes, L.V. Araujo, M.D. Levi, *Minerals Eng.*, 8, 1467 (1995).
- 6) L.F. Mondolfo, *Aluminum Alloys: Structure and Properties*, p. 695, Butterworths, London (1976).

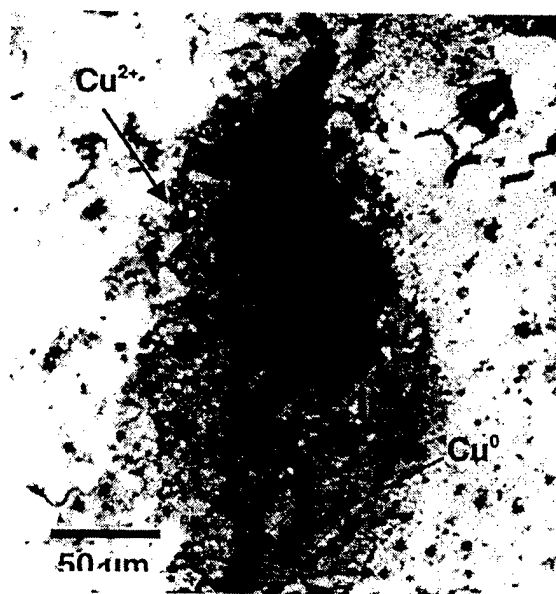


**Figure 1.** A pit on 2024-T3 subjected to 5% NaCl salt fog exposure for 168 h showing evidence of  $\text{Cu}^{2+}$  and  $\text{Cu}^0$  corrosion product. Solution flow is from top to bottom.

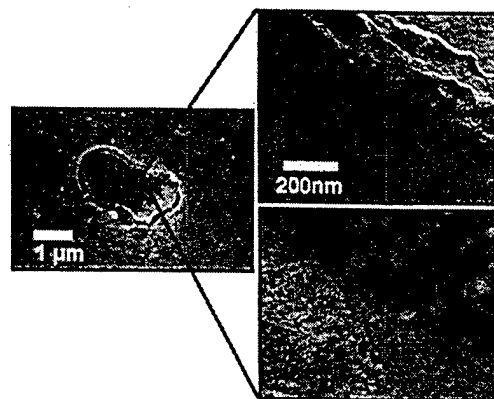


**Figure 3.** Montage of backscatter electron micrographs showing Cu cluster formation associated with dealloying of an S phase particle in 2024-T3 exposed to aerated 0.1 M NaCl solution at pH 4.

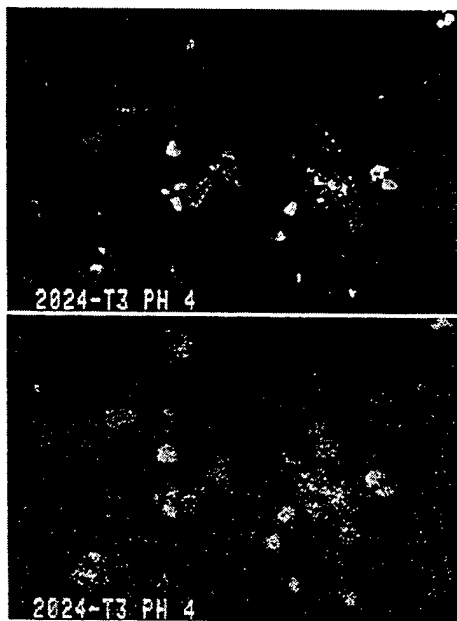


**Figure 2.** Backscatter electron micrograph (top) and Cu x-ray map (lower) showing redistribution of Cu associated with second phase particle dissolution.

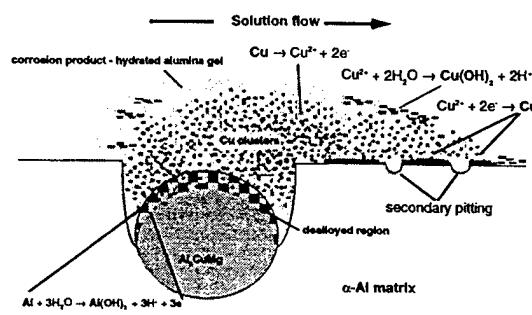


**Figure 4.** Schematic illustration of Cu release from dealloying S phase particles in Al-Cu-Mg alloys.

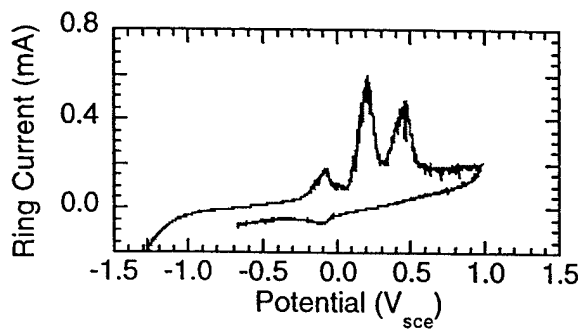


**Figure 5.** The stripping voltammogram for Cu from Pt in deareated 0.5 M NaCl is characterized by 3 peaks.

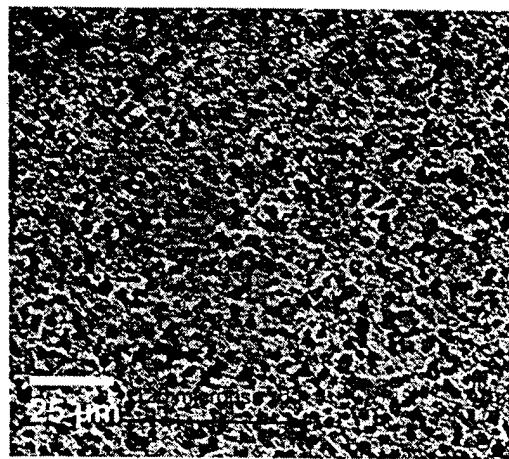


**Figure 7.** Optical micrograph of an Al-4Cu disk electrode after exposure in the RRDE experiment. “Uniform” pitting occurs across the surface of the electrode.

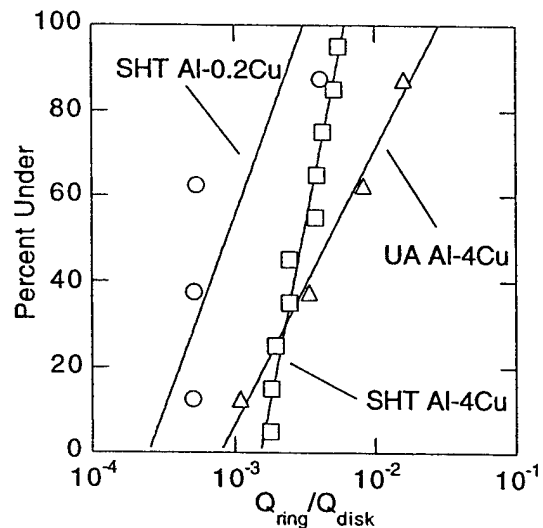


**Figure 6.** Probability plot for Cu collection from SHT Al-0.2Cu, SHT Al-4Cu, and UA Al-4Cu.

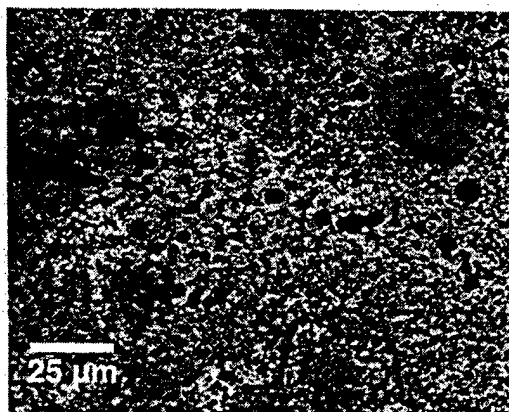


**Figure 8.** Optical micrograph of peak aged Al-4Cu after exposure in the RRDE experiment. Corrosion is localized around second phase particles and at grain boundaries.

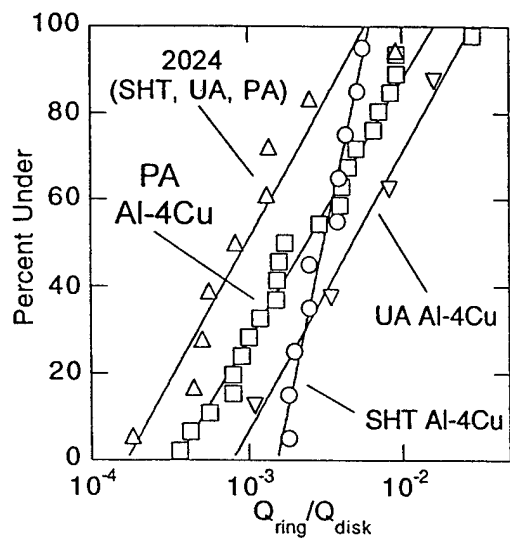


**Figure 9.** Probability plot for Cu collection from 2024, PA Al-4Cu, UA Al-4Cu, and SHT Al-4Cu.

## **Key Words**

aluminum alloys  
Al-Cu  
Al-Cu-Mg  
Al<sub>2</sub>Cu  
Al<sub>2</sub>CuMg  
dealloying  
pitting  
rotating ring disk electrode  
RRDE  
intermetallic compound

## **Corrosion Resistant Coatings for 2XXX Aluminum Alloys and the Electrochemical Characterization of the S-Phase<sup>†</sup>**

R.G. Buchheit and J. L. Searles, Department of Materials Science and Engineering, Ohio State University, 477 Watts Hall, 2041 College Rd., Columbus, OH 43210.  
Tel. (614) 292-6085, FAX (614) 292-9857, buchheit.8@osu.edu

### **Abstract**

Chromate and hydrotalcite conversion coatings were applied to Al2024-T3 panels at potentials ranging between -1000 mV and +150 mV and then tested for corrosion resistance and Cu concentration. For both types of coatings, a minimum in Cu concentration correlated with a maximum in coating corrosion resistance. This maximum fell within the OCP range for the S-phase in each coating bath. These findings suggest that coating Al2024-T3 in the OCP range of the S-phase, Al<sub>2</sub>CuMg, is an effective way to control Cu enrichment of the coatings and thereby increase their corrosion resistance.

### **Background**

Chromate conversion coatings are an important class of corrosion resistant coatings for Al-Cu-Mg alloys. However, the application, removal, and disposal of chromate coatings is environmentally hazardous and poses a serious health risk because chromates are known human carcinogens. An alternative lithium-based hydrotalcite coating has been developed for use on these 2XXX series aluminum alloys, such as Al2024-T3.<sup>1</sup> Though it is non-toxic and easily applied, the corrosion resistance of this coating is not as high as the current chromate coatings. One factor believed to contribute to lower corrosion resistance is Cu enrichment of the surface that occurs during the coating process.

Aluminum alloys of the 2XXX series contain significant amounts of Cu that are added to enhance the mechanical properties of the alloy by partitioning to second phase precipitates. Analysis of Al2024-T3 (Al-4.4Cu-1.5Mg-0.6Mn) has shown that 60% of the second phase particles are Cu-rich Al<sub>2</sub>CuMg, the S-phase, which is more active than the surrounding Al matrix in Cl<sup>-</sup> containing environments.<sup>2</sup> The S-phase is corrodes by dealloying in many aqueous Cl<sup>-</sup> environments. In this process, Al and Mg are preferentially dissolved, leaving Cu from the S-phase to enrich the surface.<sup>3</sup>

This dealloying process is also believed to occur during aqueous processing to form hydrotalcite coatings on Al2024-T3 and similar alloys. During the coating process, panels are immersed in an aqueous bath for a period of time so that the coating can form.

---

<sup>†</sup> This work was supported in part by DARPA under contract no. F49620-96-1-0305.

A possible method for controlling the effects of Cu enrichment is to find a way to keep the S-phase particles from corroding in aqueous environments in the first place.

The corrosion rate of a metal is generally minimum when it is at its open circuit potential (OCP). If the potential is driven positive of the OCP, anodic dissolution will occur.<sup>4</sup> In this process, there is a depletion of electrons in the metal due to the anodic overpotential so the anodic current density increases, and anodic dissolution proceeds. Similarly, the corrosion rate increases as a result of an excess of electrons that drives the cathodic reduction reaction when a cathodic overpotential is applied. Figure 1 illustrates the electrochemical characteristics of a typical metal in an aqueous solution.

If the S-phase OCP is different from the OCP of the bulk alloy, then the particles will corrode under the polarization conditions that are forced upon it by the Al matrix. Polarization in either direction leads to Cu redistribution from the S-phase particles, as shown in Figure 2.

Theoretically, adjusting the potential of the bulk alloy to the OCP of the S-phase during the coating process will prevent the corrosion of the particles and, therefore, reduce the Cu enrichment and increase the corrosion resistance of the coating.

## **Objectives**

The objectives of this work are to electrochemically characterize the Al alloy 2024-T3 and the S-phase, Al<sub>2</sub>CuMg, in the lithium-based hydrotalcite and chromate conversion coating baths and to use this information to decrease the Cu enrichment of the hydrotalcite coating. It is a further objective to determine if any decrease leads to an increase in the corrosion resistance of hydrotalcite coating. The hydrotalcite coating will be compared with the standard chromate conversion coating with respect to these characteristics.

## **Technical Approach**

### **Electrochemical Characterization**

Open circuit and anodic polarization measurements were conducted on the bulk Al2024-T3 and the S-phase, separately, in the hydrotalcite and chromate conversion coating baths at ambient temperature using the Corrware™ software package. The compositions of the coating baths are shown in Table I.

The OCP tests ran for 30 minutes at a scan rate of 0.3 points/second. The intermetallic sample was diamond polished to a 3µm finish and masked with an opaquing pen such that only the S-phase was exposed to the solution. A small rectangle of known area was taped off and photographed. The photograph was scanned into Adobe® Photoshop®

4.0.1 where the percent area was measured based on the contrast between the exposed S-phase area and the masked portions of the sample.

### **Coating and Impedance**

To explore the effect of applied potential on the Cu concentration, coatings were formed at various applied potentials. The information collected from the above testing was used to define a range of potentials that traversed the OCP of both the bulk alloy and the S-phase. A potentiostat was connected to Al2024-T3 panels to control the potential during the coating process in an agitated bath. The panels were not rinsed before drying in air. Hydrotalcite coatings were applied for 30 minutes at potentials ranging from -576mV to -226mV at 50mV increments. Additional potentials from -1000mV to -700mV and -150mV to +150mV were also applied at 100mV increments to complete the range. Chromate coatings were applied for 5 minutes over the same range, -1000mV to +150mV, with 50mV increments between -650mV and -250mV.

The coating corrosion resistance was tested by Electrochemical Impedance Spectroscopy (EIS). Panels were soaked in 0.5M NaCl for 23-25 hours prior to impedance testing. Spectra were collected over a frequency range of 10,000 to 0.01 Hz at a rate of five steps/decade at the open circuit of the coating. The equivalent circuit shown in Figure 3 was used to determine the mean coating resistance,  $R_c$ , in  $\Omega \cdot \text{cm}^2$ . This value was used as the figure of merit to assess the coating corrosion resistance.

### **Cu Surface Enrichment**

Cu surface enrichment was measured using Inductively Coupled Plasma Emission (ICP). In this technique, an aqueous sample is “nebulized” into an aerosol mist and sprayed directly into the center of an argon plasma.<sup>5</sup> Here, the solvent is removed, and the sample is vaporized and atomized so that its electrons can then be excited to higher energy levels by collisions with high energy electrons in the plasma. These transitions emit a characteristic spectra of light from which the composition of the sample can be obtained. The spectra is converted to concentration of the element based on the intensity of the peak. This intensity is compared to a calibration curve that was created from samples of known concentrations to find the concentration of the element in the unknown sample.

Samples were prepared by scraping a quantity of coating from each panel, weighing it, and dissolving it in 10mL of 10%HNO<sub>3</sub> contained in plastic bottles. Reference samples of 10%HNO<sub>3</sub> and uncoated Al2024-T3 were also tested as a baseline.

## Accomplishments

### Electrochemical Characterization

The OCP versus time measurements in Figures 4 and 5 in the hydrotalcite and chromate conversion coating baths, respectively, illustrate the behavior of the S-phase-Al matrix galvanic couple. In the hydrotalcite bath, a 250mV potential difference develops between the S-phase and the Al matrix after 30 minutes, with an even greater difference of more than 400mV observed at the beginning of the test. This large potential difference represents a large driving force for galvanically stimulated dissolution of the S-phase. Dealloying occurs rapidly under these conditions, leaving Cu to enrich the surface where the particle had been. It is suspected that the corrosion resistance of the coating is compromised by this contamination.

However, the potential difference between the S-phase and the matrix is always less than 50mV in the chromate conversion coating. The driving force for galvanically stimulated dissolution in this environment is much lower, indicating that not much Cu is redistributed on the surface. Under such conditions, the corrosion resistance is expected to remain high, even under normal coating conditions.

### Coatings, Impedance, and Cu Concentration

Figure 6 and 7 show the mean coating resistance and Cu concentration profiles, respectively, over the range of potentials for the hydrotalcite coating. The broad trendlines show that the maximum in the coating resistance correlates to a minimum in the Cu concentration. Though the data for the hydrotalcite coating is scattered, the OCP range of the S-phase falls in the middle of the broad maximum in coating resistance where we would expect to find low Cu concentration and high corrosion resistance.

Similarly, Figures 8 and 9 show the mean coating resistance and Cu concentration profiles, respectively, over the range of potentials for the chromate conversion coating. In this case, the data is much less scattered and the trends can clearly be seen. The maximum in coating resistance corresponds to the minimum in the Cu concentration where the OCP range of the S-phase is observed.

These data show that a decrease in Cu enrichment of either coating leads to an increase in the corrosion resistance of that coating. It also suggests that controlling the potential during coating such that it falls in the range of the S-phase OCP will produce this effect because Cu liberation is suspected to be minimized in this potential region.

Coating quality was also evaluated as a function of applied potential based on surface morphology examined in the SEM. Representative micrographs were taken at 1000x, 7000x, and 15000x.

Both the lithium hydrotalcite and the chromate conversion coatings formed over the entire potential range from -1000mV to +150mV. However, the quality of the hydrotalcite coating varied in accordance with the corrosion resistance and Cu concentration measured previously. Figure 10 (a) and (b) shows the variation as a function of potential in the coating morphology. In (a) the measured coating resistance was high while the Cu concentration remained low. The coating is high quality with few inconsistencies. At high Cu concentration and low coating resistance, as in (b), the coating does not form homogeneously and is of poor quality with frequent cracking observed. However, the visual data is still quite scattered for the lithium hydrotalcite coatings.

The chromate conversion coating forms a robust coating at all potentials and Cu concentrations. The coating surface is consistent, showing the characteristic "cracked mud" morphology at all potentials shown in Figure 11 (a) and (b).

## Conclusion

Analysis of the data suggests that controlling the Cu content on the surface of the alloy during the coating process is beneficial in improving the corrosion resistance of coatings applied to Al2024-T3. Further, Cu enrichment of the coatings can be minimized by application of the coatings within the OCP range of the S-phase, Al<sub>2</sub>CuMg. These innovations in the coating process will produce a safer, yet more effective hydrotalcite coating that can eventually replace the current hazardous chromate conversion coatings for application with the 2XXX series aluminum alloys that are commonly used in the aerospace industry.

## References

1. Bode, M.D., Buchheit, R.G., and Stoner, G.E., "Corrosion-Resistant, Chromate-Free Talc Coatings for Aluminum." Corrosion Science, vol. 50, no. 9, March 1994, pg. 205-213.
2. Buchheit, R.G., "Copper Removal During Formation of Corrosion Resistant Alkaline Oxide Coatings on Al-Cu-Mg Alloys." Sandia National Laboratories, pg. 2.
3. Buchheit, R.G., Grant, R.P., and others, "Local Dissolution Phenomena Associated with S-Phase (Al<sub>2</sub>CuMg) Particles in Aluminum Alloy 2024-T3." Journal of the Electrochemical Society, vol. 144, no. 8, August 1997, pg. 2621-2624.
4. Jones, Denny A., Principles and Prevention of Corrosion, 2<sup>nd</sup> Edition, Prentice-Hall, Inc., Upper Saddle River, NJ, 1996, pg. 95-97.
5. Boss, Charles B. and Fredeen, Kenneth J., Concept, Instrumentation, and Techniques in Inductively Coupled Plasma Optical Emission Spectrometry, 2<sup>nd</sup> Edition, Perkin Elmer, [www.perkin-elmer.com/atomic/indexes.html](http://www.perkin-elmer.com/atomic/indexes.html), section 2.

## Tables and Figures

**Table I:** Recipe for coating baths

Hydrotalcite Coating		Chromate Coating	
Chemical Species	g/L DI H <sub>2</sub> O	Chemical Species	g/L DI H <sub>2</sub> O
LiNO <sub>3</sub>	2.2	Alodine 1200S	7.55
KNO <sub>3</sub>	28.3	* Adjust pH to 1.69 with HNO <sub>3</sub>	
45wt% Na <sub>2</sub> Al <sub>2</sub> O <sub>4</sub>	1.78		

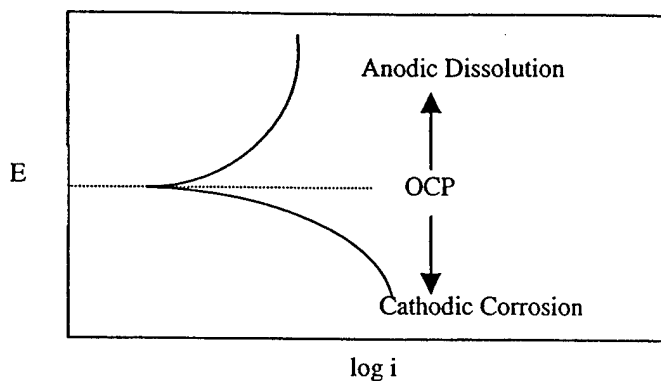


**Figure 1:** Schematic view of the electrochemical characteristics of a metal in an aqueous environment.

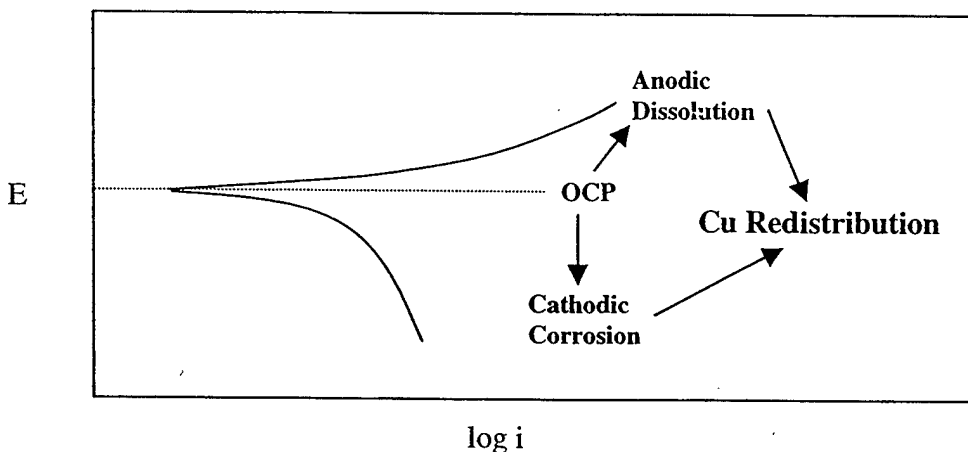


**Figure 2:** Corrosion characteristics of the S-phase in aqueous solutions leading to Cu redistribution under anodic and cathodic polarization conditions.

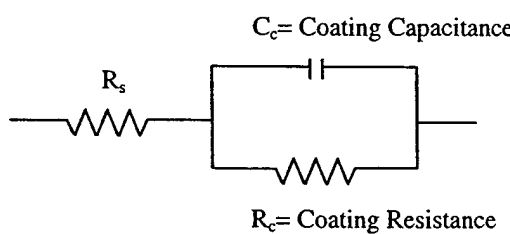


**Figure 3:** Equivalent circuit for measuring coating resistance from impedance data.

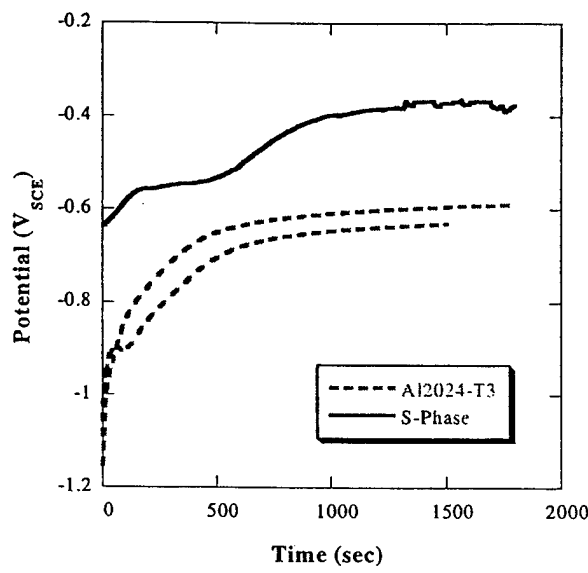


**Figure 4:** OCP for Al2024-T3 and the S-phase in lithium hydrotalcite coating.

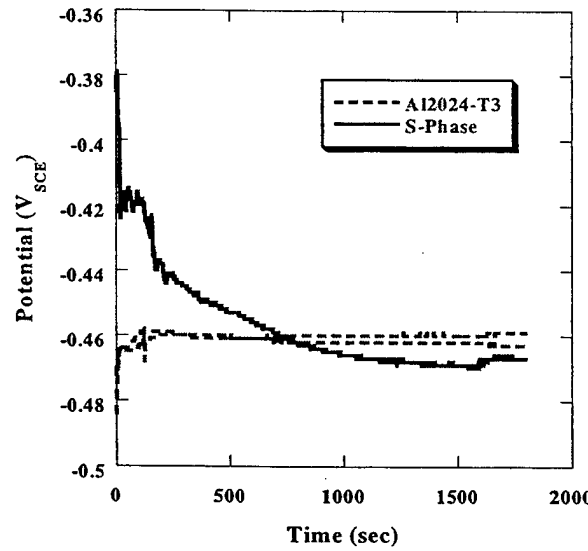


**Figure 5:** OCP for Al2024-T3 and the S-phase in chromate conversion coating.

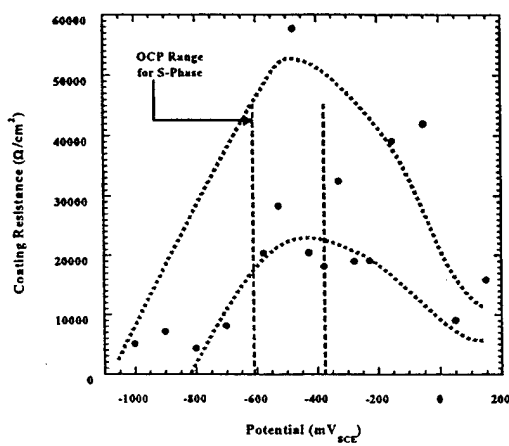


**Figure 6:** Mean coating resistance of lithium hydroxide coating applied at different potentials

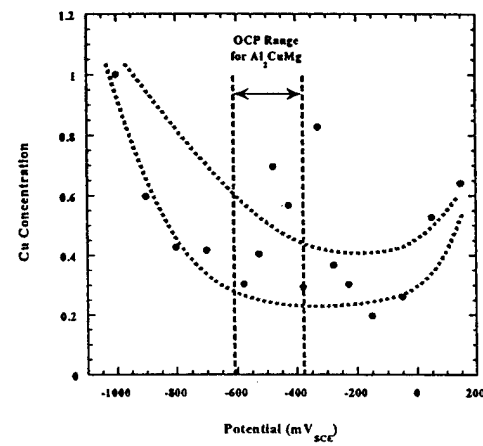


**Figure 7:** Cu concentration of lithium hydroxide coating applied at different potentials

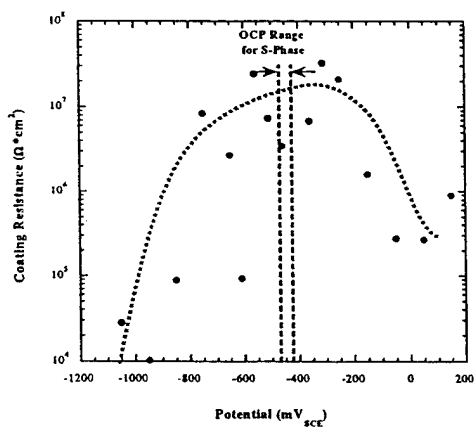


**Figure 8:** Mean coating resistance of chromate conversion coating applied at different potentials.

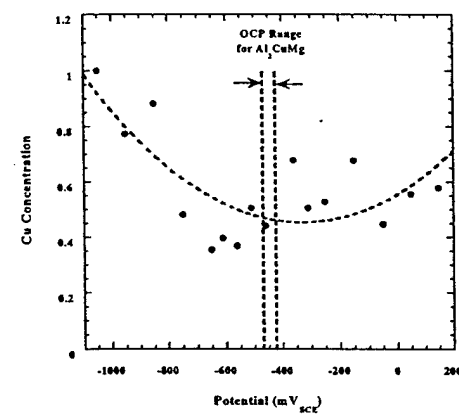
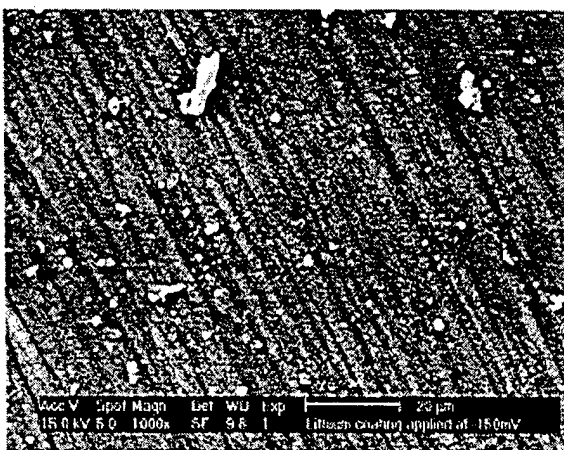


**Figure 9:** Cu concentration of lithium chromate conversion coating applied at different potentials.

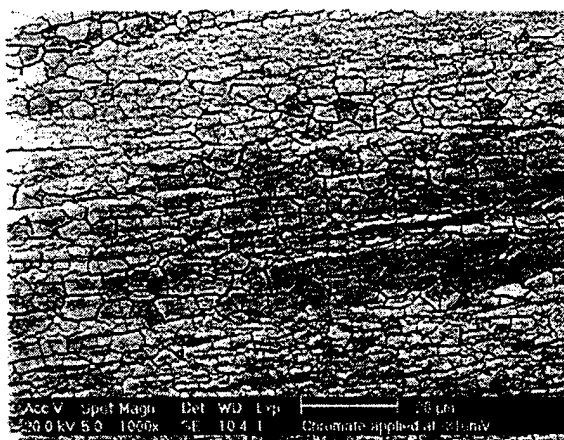


(a) -150mV: low [Cu], high  $R_c$

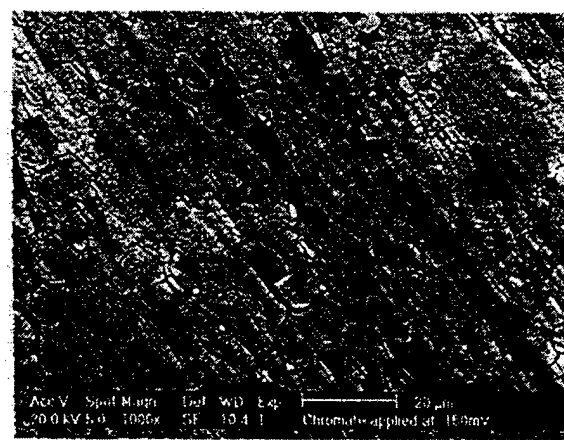


(b) -1000mV: high [Cu], low  $R_c$

**Figure 10:** Surface morphology of lithium hydrotalcite coatings formed at (a) -150mV and (b) -1000mV.



(a) -310mV



(b) -150mV

**Figure 11:** Surface morphology of chromate conversion coatings formed at (a) -310mV and (b) -150mV.

## **Influence of Chromate on the Corrosion Behavior of Aluminum Alloys**

Q. Meng, G. S. Frankel, Fontana Corrosion Center, The Ohio State University

Tel: 614-688-4128, Fax: 614-292-9857, frankel.10@osu.edu

### **Abstract**

As part of the effort to better understand the influence of chromate on the corrosion behavior of Al alloys, a series of experiments has been initiated. In the first part of the work, three alloys of interest to the US Army were identified: AA2519, AA5083, and AA7039.

Subsequent work has focussed on 7xxx alloys with varying Cu content. In particular, the role of Cu in 7xxx alloys on the efficacy of corrosion inhibition by chromates will be investigated. This process has been initiated by the procurement of alloys with varying Cu content.

### **Background**

Localized corrosion of high strength Al alloys (2xxx and 7xxx series) is a major problem that is partially rectified by the use of chromate-containing coatings. In order to understand the mechanism of inhibition by chromates, it is necessary to fully understand the mechanism of localized corrosion. Ultimately, this knowledge will help to guide the development of chromate-free protection systems.

The corrosion susceptibility of these alloys is associated with the heterogeneous microstructure, in particular the presence of intermetallic particles. In 2xxx and 7xxx alloys the intermetallic particles often contain high concentrations of Cu. Understanding how these particles affect localized corrosion and how chromate inhibitors alter that process is critical.

There have been reports that peak aged 7XXX alloys can be well protected by chromate conversion coatings, whereas the same alloys in the overaged condition are not. This phenomenon has not been investigated. For instance, it is not clear if the problem is with the formation of the conversion coating, or if the problem is associated with the susceptibility of the material. The latter is not expected, since overaged alloys are typically more corrosion resistant than peak aged alloys.

### **Objective**

Investigate the role of microstructure of Al alloys on the chromate conversion process and corrosion susceptibility of conversion-coated samples. The focus will be on the effect of Cu concentration and temper on the behavior of 7xxx alloys.

## **Technical Approach**

The approach will be to analyze the microstructure of high strength Al alloys and to investigate how the various microstructural components behave in the absence or presence of chromate. The role of Cu will be a focus.

## **Accomplishments**

The microstructure of three alloys has been investigated: AA2519, AA5083, and AA7039. Figures 1-3 show back-scattered electron images of polished sections of these alloys. The back-scattered mode is very sensitive to differences in Z number, and thus allows for visualization of the microstructure. The shapes, sizes and area fractions of the intermetallic particles were noted by analysis of the micrographs, and the results are shown in Tables I and II. The compositions of the alloys as a whole, the matrix phases, and the large intermetallic particles were determined by EDS, Table III.

The alloy 2519 is a simple Al-Cu binary. It contains theta phase particles of varying size. Theta phase should be  $\text{Al}_2\text{Cu}$ , which is 33 at% Cu. The EDS analysis indicates 50 at%.

Alloy 5083 is a non-heat-treatable alloy containing Mg and Mn, and small amounts of other elements. The large constituent intermetallic particles are enriched in Mn, Fe, and Si. Mg is contained in the smaller particles that are not easily identified in the SEM. The large particles have at least two phases with differing darkness in the back-scattered image, Figure 2. The brighter phase is enriched in all of the alloying elements: Mn, Fe, and Si. The large particle shown in Figure exhibits cracks, which probably formed during cold working of the material.

Alloy 7039 is a low-Cu 7xxx alloy, containing Mg and Zn, with smaller amounts of several other elements. The blocky constituent particle shown in Figure 3 is enriched in Fe, Mn, and Si. It is expected that this alloy contains smaller eta phase intermetallic particles,  $\text{MgZn}_2$ .

Alloy 7039 will be used as the low-Cu 7xxx alloy in future work. It will be compared to medium and high Cu content 7xxx alloys. Candidate alloys include 7129 for the medium Cu content alloy (0.5-0.9 %) and 7075 for the high Cu content alloy (1.2-2.0 %).

Table I. Shapes and sizes of intermetallic particles in the three alloys.

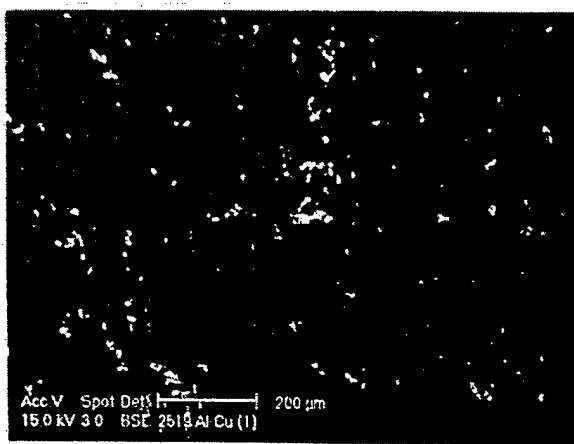
Alloy	Shape of particles	Particle size
AA2519	round	A few $\sim 15\mu\text{m}$ , many $<1\mu\text{m}$
AA5083	Rounded edges	A few $\sim 10\mu\text{m}$ , many $<1\mu\text{m}$
AA7039	Rectangular, sharp corners	A few $\sim 15\text{--}8\mu\text{m}^2$ , many $<1\mu\text{m}$

Table II. Area fraction of intermetallic particles in the three alloys.

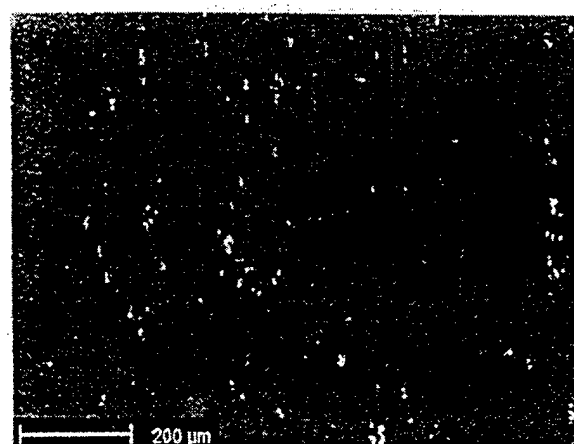
Alloy	L	LT	ST
AA2519	2.24%	0.62%	0.53%
AA5083	1.98%	1.88%	1.36%
AA7039	0.18%	0.11%	0.14%

Table III. Composition of various alloys from handbook and EDS analysis of the alloys and various phases and particles, in at%.

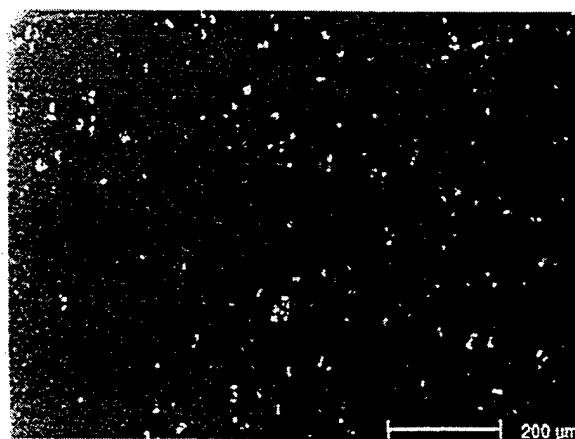
	Si	Fe	Cu	Mn	Mg	Cr	Zn	Al
<b>AA2519</b>								
handbook								
overall			6.78					bal
matrix			6.36					bal
particle			49.74					bal
<b>AA5083</b>								
handbook	0.4	0.4	0.1	0.4-1.0	4.0-4.9	0.05-0.25	0.25	bal
overall					0.76	5.46		bal
matrix						5.25		bal
particle								
bright region	4.3	16.28		12.76				bal
dark region	0.26	12.34		10.74				bal
<b>AA7039</b>								
handbook	0.3	0.4	0.1	0.1-0.4	2.3-3.3	0.15-0.25	3.5-4.5	bal
overall						3.47		bal
matrix						3.39		4.77
particle	3.86	23.32		6.37			1.8	bal



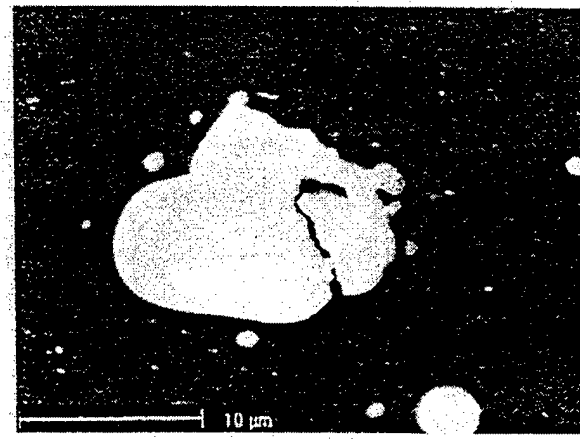
Longitudinal surface of AA2519



Long transverse surface of AA2519

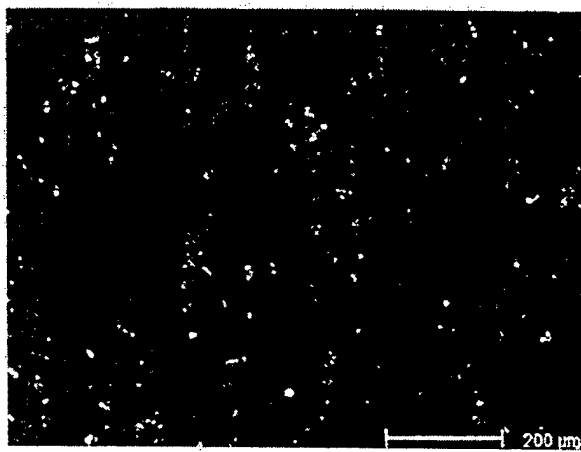


Short transverse surface of AA2519

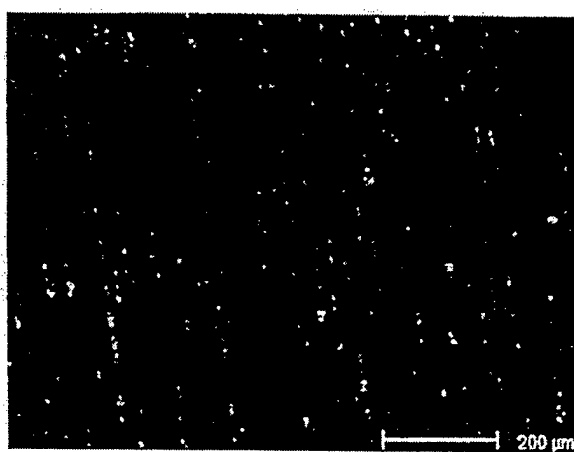


Shape of intermetallic particle in AA2519

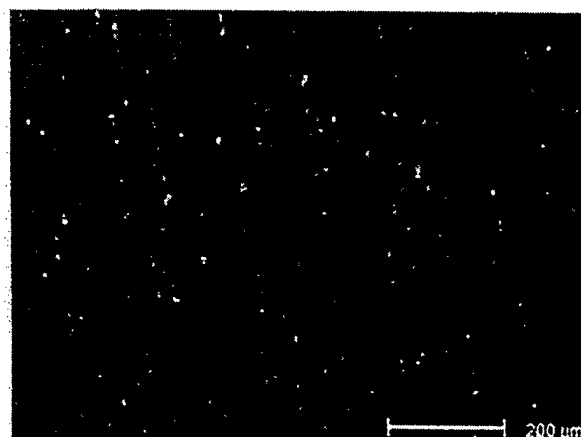
Fig. 1 Back-scattered SEM images for AA2519.



Longitudinal surface of AA5083



Long transverse surface of AA5083

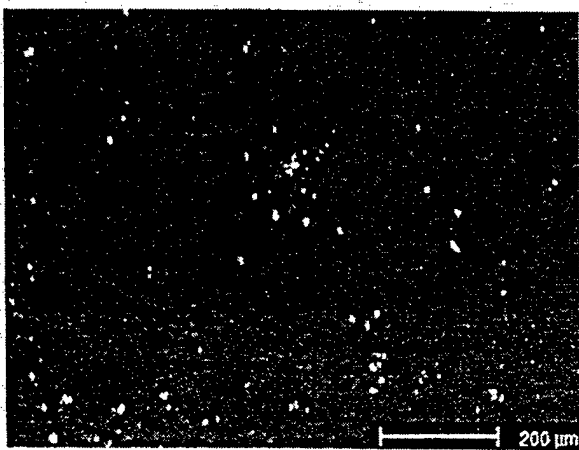


Short transverse surface of AA5083



Shape of intermetallic particle in AA5083

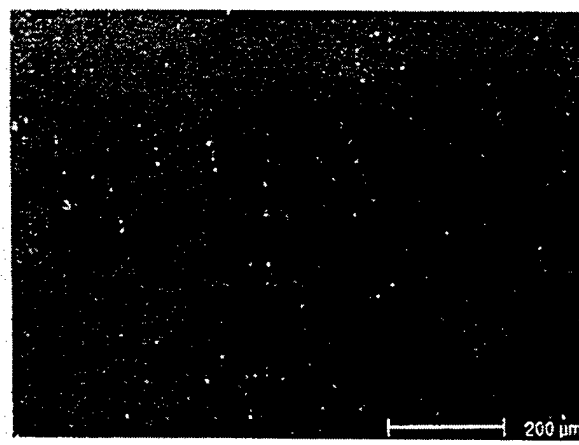
Fig. 2 Back-scattered SEM images for AA5083.



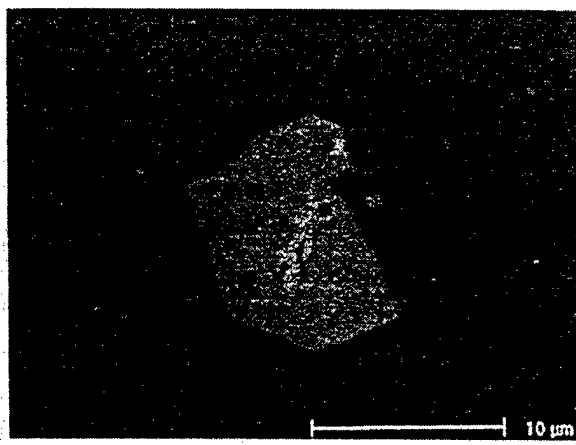
Longitudinal surface of AA7039



Long transverse surface of AA7039



Short transverse surface of AA5083



Shape of intermetallic particle in AA5083

Figure 3. Back-scattered electron images for AA7039.

## Formation of Chromate Conversion Coatings on Mixed Phases of Al/Cu/Mg Alloys

W. McGovern<sup>†</sup>, R. G. Buchheit<sup>††</sup>, R. L. McCreery<sup>†</sup>, <sup>†</sup> Department of Chemistry, <sup>††</sup> Department of Materials Science and Engineering, Ohio State University, 2041 College Rd. Columbus, OH 43210.  
<sup>††</sup>Tel. (614) 292-2021, email mcreery.2@osu.edu.

### Abstract

The interaction of a Alodine 1200S conversion coating solutions with a polyphase ingot containing intermetallic phases AlCuMg, Al<sub>2</sub>CuMg, Al<sub>5</sub>CuMg<sub>4</sub> and two other solid solution phases has been characterized by confocal scanning Raman spectroscopy and Auger electron spectroscopy. Results show that the intensity of conversion coating formation decreases as the concentration of Cu in a phase increases. Conversion coating film thickness also scales inversely with Cu concentration. Raman spectroscopy shows that Fe-(CN)-Cu surface complex forms that inhibits conversion coating formation. The consequences of these results on the corrosion protection of 2024-T3 have also been considered.

### Background

Chromate conversion coatings (CCCs) are used as the foundation layer for coating systems on aluminum alloys used in aerospace applications. The key film-forming reaction, reduction of chromate, proceeds slowly on aluminum. Accelerators like ferricyanide are added to conversion coating formulations to increase the rate of this reaction. Recently, we reported findings from a detailed study of the structure of the film, and the role of ferricyanide during CCC formation from commercial preparations such Alodine 1200 S (1). To summarize briefly, metallic aluminum exposed by the low pH and fluoride ion in the bath reduces Cr(VI) to Cr(III), which then precipitates as Cr(III) hydroxide. Fe(CN)<sub>6</sub><sup>-3/4</sup> acts as a redox mediator for this reduction, and is trapped in the CCC as both physisorbed Fe(CN)<sub>6</sub><sup>-3</sup> and “Berlin Green”, a polymeric Fe-CN-Fe coordination compound. During formation of the polymeric Cr(III) hydroxide, Cr(VI) adsorbs to the oxide matrix, forming Cr(III)-O-Cr(VI) bonds. This chromium (III)/(VI) mixed oxide acts as a storage site for Cr(VI), which may be released later in the field. The release and migration of soluble Cr(VI) to defect sites is likely to underlie the mechanism of “self-healing” of CCC treated surfaces.

Since CCCs form by interaction of the alloy with the solution, the type and amount of alloying elements greatly affects conversion coating formation. For example, copper and magnesium added to strengthen aluminum alloys, are segregated into second phase particles that tend to inhibit coating formation. Al/Fe/Mn, and other combinations form intermetallic compounds (IMCs) may also complicate conversion coating and usually serve as sites for coating breakdown.

This study has addressed the question of the effect of IMCs on CCC formation from Alodine 1200 S solutions. An ingot containing five distinct phases including three Al-Cu-Mg IMCs was treated with Alodine, then the distribution of CCC components was determined with Raman microscopy. Samples of 2024-T3 were treated in the same manner, and IMC particles were analyzed with Raman to reveal possible variations in CCC composition and thickness. Since Raman spectroscopy is sensitive to the molecular structure of the CCC, it reveals the effects of IMCs on the final coating properties. The consequences of these results on the corrosion protection of 2024-T3 have also been considered.

## Results

In these experiments, CCCs were formed on a cast polyphase ingot containing the intermetallic compounds AlCuMg, Al<sub>2</sub>CuMg, Al<sub>5</sub>Mg<sub>4</sub>Cu and two solid solution phases. The compositions of these phases is indicated in Table I. Figure 1 is an optical micrograph showing the coarse structure of the ingot, and the distribution of the various phases. The intermetallic compounds, which solidified first as dendrites or needles, exhibit globular or lenticular morphologies in this metallographic cross section. These regions are 10 or more micrometers in width and can be several millimeters in length. The solid solution phases solidified last in the interdendritic spaces. These regions are tens of micrometers in width and length except for small regions where the two phases appeared to solidify with a eutectic-like morphology. Overall, this ingot consists of discrete, coarse phases with widely varying compositions. Since the phase dimensions are at least on the order of 10  $\mu\text{m}$ , this sample is well-suited for Raman imaging studies.

The water polished cross section of the ingot shown in Fig. 1 was Alodine treated for 5 minutes at room temperature, then subject to Raman imaging. Figure 2, a false color intensity map of the Raman scattering in the 750-1000  $\text{cm}^{-1}$  range, is superimposed on the micrograph of Fig. 1. In this spectral range, a scattering peak, centered at 860  $\text{cm}^{-1}$ , exists that is characteristic of the Cr(III)/Cr(IV) mixed oxide in Alodine CCCs. The 860  $\text{cm}^{-1}$  band is most intense on the Al-Mg solid solution phase and least intense on AlCuMg. The 860  $\text{cm}^{-1}$  band intensity is generally intermediate between those observed on Al<sub>2</sub>CuMg, Al<sub>5</sub>Mg<sub>4</sub>Cu, and the eutectic phase. Figure 2 also shows individual Raman spectra obtained at various points on the polished face. In general, the intensity of the 860  $\text{cm}^{-1}$  band varies inversely with the Cu content of the phase on which the measurement is made.

To determine if CCC film thickness was related to 860  $\text{cm}^{-1}$  intensity, a separate experiment was carried out. In this experiment, an Alodine coating was applied to 2024-T3 and the sample was examined both by profilometry and Raman spectroscopy. The 860  $\text{cm}^{-1}$  intensity was then compared to the local thickness. Figure 3 shows three superimposed profilometer traces across the interface between epoxy and AA-2024-T3, after polishing and Alodine treatment (1 minute, room temperature). The CCC thickness increases with distance from the epoxy, and presumably

becomes constant at some point beyond the range of the profilometer. Raman spectra with  $\sim 1 \mu\text{m}$  spatial resolution were obtained at many distances from the epoxy/alloy junction (some of which are indicated in Figure 3), and the  $860 \text{ cm}^{-1}$  peak area was determined at each distance. A plot of Raman peak area versus observed CCC thickness is shown in Figure 4. Although the data are scattered, a positive linear relationship reasonably describes the relationship between  $860 \text{ cm}^{-1}$  intensity and film thickness. These results support the notion that the  $860 \text{ cm}^{-1}$  band area is proportional to film thickness, though variations in focus, power density, and collection parameters would make it difficult to directly determine thickness from a given Raman intensity, unless the conditions of Figure 4 are reproduced exactly.

Auger sputter depth profiles of conversion coatings on the various phases in the ingot confirm that conversion coatings are thinner on Cu-rich phases. CCC coatings were formed on the ingot, using a 3 second Alodine treatment at room temperature. Profiles of atomic composition as a function of sputtering time are shown in Figure 10 for phases 1, 2, 3 and 5. Phase 4 is not shown due to its heterogeneous composition. All four phases show chromium and oxygen on the surface, indicating some chromium oxide deposition over the entire surface. The chromium concentration peaks at about 20% in each case, but the oxide thicknesses vary from phase to phase. Phase 1 has a relatively thin layer of Cr, with the chromium largely absent after 5 minutes of  $\text{Ar}^+$  sputtering. On phases 3 and 5, however, the Cr signal persists much longer, at least 10-15 minutes. The sputtering time at which the Cr atom percentage decreases to half of its maximum value is approximately 4.5 minutes, 7.5 minutes, 11.5 minutes and 13.5 minutes for phases 1, 2, 3 and 5, respectively. These results indicate a thicker chromium containing film over phases 3 and 5 than over phases 1 and 2.

Raman imaging also shows that CCC formation is inhibited over IMCS present in 2024-T3. Figure 6 shows a typical distribution of constituent IMCs in 2024-T3. Large  $\text{Al}_6(\text{Fe}, \text{Cu}, \text{Mn})$  and smaller S-phase particles,  $\text{Al}_2(\text{Cu}, \text{Mg})$ , are readily detected. Figures 7 and 8 show companion optical micrographs and superimposed Raman  $860 \text{ cm}^{-1}$  maps collected in the vicinity of  $\text{Al}_6(\text{Cu}, \text{Mn}, \text{Fe})$  and  $\text{Al}_2\text{CuMg}$  particles respectively. The  $860 \text{ cm}^{-1}$  intensity is much weaker over  $\text{Al}_2\text{CuMg}$  particle as expected based on the preceding results. The  $\text{Al}_6(\text{Cu}, \text{Mn}, \text{Fe})$  phase was not present in the ingot discussed above, but the decrease in  $860 \text{ cm}^{-1}$  intensity over the particle in the 2024-T3 sample indicates CCC formation is inhibited over this phase also.

Raman spectra of CCC films show features in the CN stretching region ( $2000\text{-}2200 \text{ cm}^{-1}$ ), which are associated with presence of  $\text{Fe}(\text{CN})_6^{3/4-}$  on coated surfaces. There are significant differences in the CN stretch region of spectra collected from each of the phases as shown in Figure 5. The eutectic phase and the Al-Mg solid solution phase exhibit the  $2095$  and  $2145 \text{ cm}^{-1}$  bands, which are observed for a CCC on AA-2024 and correspond to physisorbed  $\text{Fe}(\text{CN})_6^{-3}$ . In contrast,  $\text{AlCuMg}$  and  $\text{Al}_5\text{Mg}_4\text{Cu}$  exhibit a distinct  $2175 \text{ cm}^{-1}$  band similar to that observed when pure copper is exposed to  $\text{Fe}(\text{CN})_6^{-3}$ . In this respect, the presence of the  $2171\text{-}2175 \text{ cm}^{-1}$  band distinguishes the film formed on  $\text{AlCuMg}$ ,  $\text{Al}_2\text{CuMg}$ , and  $\text{Al}_5\text{Mg}_4\text{Cu}$  after exposure to  $\text{Fe}(\text{CN})_6^{-3}$ .

Similarly the presence of the 2095 and 2145  $\text{cm}^{-1}$  bands on the Al-rich phases characterizes the surface films on those phases. Overall, these results are taken to indicate that CCC formation is inhibited on Cu-rich IMCs compared to formation on Al-rich phases. The Raman spectra of Figure 5 indicate that a distinct cyano surface species forms when the Cu-rich phases and pure Cu are exposed to the Alodine solution. This Raman feature is interpreted as a  $\text{Cu-Fe}(\text{CN})_6$  material, which forms when  $\text{Fe}(\text{CN})_6$  chemisorbs on copper. It is suspected that this material suppresses CCC formation resulting in the weak 860  $\text{cm}^{-1}$  intensity observed on Cu-rich phases. To explore the possibility that chemisorb  $\text{Fe}(\text{CN})_6$  forms a passivating layer that inhibits CCC formation on Cu-rich phases, a mixed phase ingot was treated with a synthetic Alodine solution containing all components except Cr(VI). After a one minute treatment, the ingot was rinsed and dried for 2 days, then exposed to conventional Alodine solution for five minutes. After this treatment, a CCC was not formed. Instead, a black film, which did not adhere to the surface, was detected. Open circuit potential measurements also suggested that the Cr(IV)-free pretreatment resulted in sample passivation. Figure 9 compares the open circuit potential for the ingot during Alodine treatment with and without the  $\text{Fe}(\text{CN})_6^{3-}$  pretreatment. The OCP is much more positive if the ingot was exposed to  $\text{Fe}(\text{CN})_6^{3-}$  before Alodine treatment. A sample of AA-2024 treated similarly did not show the same effect, with its OCP, and CCC formation apparently unaffected by  $\text{Fe}(\text{CN})_6^{3-}$  pretreatment.

### Mechanism and Implications

Ferricyanide additions constitute no more than 15% by weight of the solid ingredients used to make-up Alodine 1200S (2). As such, ferricyanide is fairly categorized as a minor chemical addition. However, in the presence of  $\text{Fe}(\text{CN})_6^{3-}$ , the coating formation rate is greatly increased with a concomitant decrease in processing time (3). Therefore, its use in CCC formulations designed for Al alloys carries great practical advantage.

It has been known for many years that Cu-bearing Al alloys are highly susceptible to corrosion. Even the best chromated corrosion protection systems do not always provide acceptable levels of corrosion protection on alloys that contain 4 to 6% Cu or more. The results of this study suggest that part of the reason may lie with the fact that there is a negative interaction between a minority ingredient in CCC formulations, ferricyanide, and minority phases in Al-Cu-X alloys, Cu-rich IMCs, which significantly undermines the effectiveness of this corrosion protection strategy.

Before proposing a mechanism to explain the effects of IMCs on CCC formation, several observations deserve special note. First, the weak 860  $\text{cm}^{-1}$  band intensity over phases 1, 2, and 3 in the ingot and over the IMC inclusions in 2024-T3 indicate either 1) that a CCC film is not forming on these phases, or 2) that a film is forming which does not contain levels of Cr(III)/Cr(VI) mixed oxide observable by Raman. Second, AES depth profiling indicates a Cr-containing film over all phases of the ingot, but the film is significantly thinner over  $\text{AlCuMg}$ , and  $\text{Al}_2\text{CuMg}$  compared to copper-poor solid solution phases. If the Cr present over phase 1 is in the

form of Cr(III)/Cr(IV) mixed oxide, its level is below the Raman detection limit. Third, cyano species are observed on Cu-rich IMC phases even in the absence of chromate. The cyanide stretch was observed on pure copper treated with  $\text{Fe}(\text{CN})_6^{-3}$ , and its frequency corresponds to a Cu-CN vibration at  $2172 \text{ cm}^{-1}$ . This band is completely distinguishable from the CN stretches observed in a CCC. Fourth, pretreatment of the ingot with a solution containing  $\text{Fe}(\text{CN})_6$  has a dramatic effect on subsequent Alodine treatment, preventing CCC formation and causing a  $\sim 400 \text{ mV}$  positive shift in the open circuit potential during Alodine treatment.

Previous investigations concluded that CCC formation requires at least two steps: reduction of Cr(VI) to insoluble Cr(III) oxy/hydroxide, mediated by  $\text{Fe}(\text{CN})_6^{-3/4}$ , and adsorption of Cr(VI) to the Cr(III) oxy/hydroxide. We have also reported that Cr(VI) adsorbs spontaneously to hydrated  $\text{Cr}(\text{OH})_3$ , and the product is the yellow Cr(III)/Cr(IV) mixed oxide with its characteristic  $860 \text{ cm}^{-1}$  Raman band. The absence of this band over phases AlCuMg and Al<sub>2</sub>CuMg implies that Cr(III)/Cr(IV) mixed oxide is prevented from forming either because Cr(VI) is not reduced to Cr(III), or because Cr(VI) is not adsorbing to Cr(III). The latter case is unlikely, since Cr(VI) spontaneously adsorbs to Cr(III) oxy/hydroxide. The most likely cause of the absence of Cr(III)/Cr(IV) mixed oxide over phases 1 and 2 is inhibition of the reduction of Cr(VI) to Cr(III).

The reduction of Cr(VI) to Cr(III) during CCC formation is strongly dependent upon redox mediation by ferricyanide, in which  $\text{Fe}(\text{CN})_6^{-3}$  is reduced by Al to  $\text{Fe}(\text{CN})_6^{-4}$ , then Cr(VI) is reduced to Cr(III) by  $\text{Fe}(\text{CN})_6^{-4}$ . If  $\text{Fe}(\text{CN})_6^{-3}$  reduction were inhibited on IMCs compared to the Al matrix, Cr(III) and CCC formation would be slower on IMCs. There is evidence that the occurrence of such an inhibition phenomenon is reasonable.  $\text{Fe}(\text{CN})_6^{-3}$  is known to adsorb to Cu, Ni, Pt, etc., with partial decomposition, to form chemisorbed cyano species, and possibly Prussian Blue, an Fe-CN-Fe polymer. The  $2172 \text{ cm}^{-1}$  band observed after exposure of pure copper to  $\text{Fe}(\text{CN})_6^{-3}$  indicates deposition of a cyano species on copper, even without aluminum or chromium present. Adsorbed  $\text{Fe}(\text{CN})_6^{-3}$  species decreases the electron transfer rate for  $\text{Fe}(\text{CN})_6^{-3/4}$  on platinum electrodes, to the point of complete deactivation in severe cases. Taken together, these observations support the hypothesis that  $\text{Fe}(\text{CN})_6^{-3}$  adsorbs to copper rich regions on the ingot surface, possibly with some decomposition to form a Cu-CN linkage or a Fe-CN-Cu bridging group. The resulting deposit inhibits electron transfer between the surface and solution phase  $\text{Fe}(\text{CN})_6^{-3/4}$ , thus decreasing Cr(III) generation and CCC formation.

If this model is correct, then pretreatment of the alloy surface with  $\text{Fe}(\text{CN})_6$  might affect CCC growth, since redox kinetics with the  $\text{Fe}(\text{CN})_6^{-3}$  in the Alodine bath might be inhibited. The results of Figure 10 indicate the profound effect of  $\text{Fe}(\text{CN})_6^{-3}$  on CCC formation, even when the pretreatment occurred several days before Alodine exposure. A CCC was not observed on any phase, and the positive potential shift during Alodine treatment implies inhibition of reduction by the surface. Observations on the ingot pretreated with  $\text{Fe}(\text{CN})_6^{-3}$  are completely consistent with a mechanism based on inhibition of CCC formation by a CN containing film which forms more rapidly on copper-rich IMCs. The behavior of IMCs in 2024-T3 is largely consistent with the

observations on the multiphase ingot. The  $860\text{ cm}^{-1}$  Raman intensity on the  $\text{Al}_6(\text{Cu},\text{Mn},\text{Fe})$  and S phase inclusions is lower than on the aluminum matrix.

There are several important implications that arise from these results. First, the low concentration of Cr(VI) over the IMCs may constitute a defect in the coating that can lead to localized corrosion. If Cr(VI) is the active protective agent, the unprotected IMC may act as a site for pit initiation or filiform corrosion. Second, the absence of chromate over IMCs may significantly affect the local charge density, changing it from a neutral or anionic region expected for adsorbed chromate or Cr(III)/Cr(VI) mixed oxide to a cationic site expected for hydrated Cr(III) or Al(III) oxides. A cationic site may attract chloride and stimulate corrosion. Third, the adsorbed cyanide and/or ferricyanide may significantly affect electron transfer kinetics at IMCs. We have already hypothesized that adsorbed cyanide inhibits  $\text{Fe}(\text{CN})_6^{3/4}$  kinetics during CCC formation, but it may also affect "field" reactions such as oxygen reduction or Al oxidation. The effects of cyanide modification of IMCs on electron transfer kinetics are currently unknown, but are likely to be substantial.

### **Plans for next year.**

We have identified alternative accelerators while investigating ferricyanide mediation, and we will examine CCC films made with these accelerators. If the role of ferricyanide in Alodine is only as an accelerator (as the data indicate), then a mediator which does not "protect" intermetallic phases should be fairly easy to find. We will examine CCC films made with alternative mediators on both the intermetallic ingot and on 2024-T3. Possibilities include  $\text{Fe}^{+3/4/2}$ , or even organic redox centers such as methyl viologen. The criteria for a successful mediator include a redox potential between that of Cr(VI)/Cr(III) and Al/Al(III), and fast redox kinetics with aluminum metal and chromate.

### **References.**

- 1) L. Xia, R.L. McCreery, J. Electrochem. Soc., 145, 3083 (1998).
- 2) Alodine 1200S Material Data Safety Sheet, Parker+Amchem, Henkel Corporation, 32100 Stephenson Highway, Madison Heights, MI November, 1987.
- 3) N.J. Newhard, Metal Finishing, p. 49, July (1972).

**Table I.** Atomic Composition from AES of Five Phases from Mixed Phase Ingot

	%Al	%Cu	%Mg	Phase
Phase 1	36.7	29.9	33.5	AlCuMg
Phase 2	48.4	22.3	23.6	Al <sub>2</sub> CuMg
Phase 3	52.2	11.3	36.5	Al <sub>5</sub> CuMg <sub>4</sub>
Phase 4	72.8	6.1	21.1	Al-Cu-Mg SS
Phase 5	88.2	0.7	11.2	Al-Mg SS

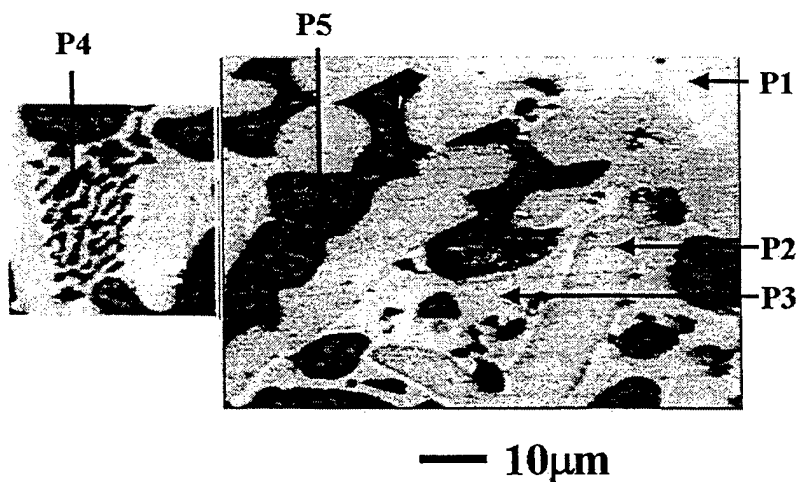


Figure 1: Optical Image of the  $\text{Al}_x\text{Cu}_y\text{Mg}_z$  phases present on the ingot.

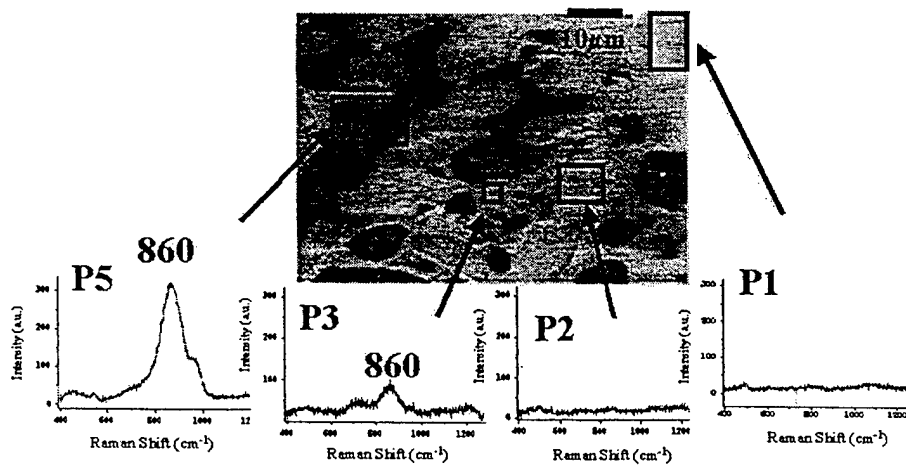


Figure 2: Average box phase spectra for the Alodine treated ingot. From left P5, P3, P2, P1. Phase 4 is not shown.

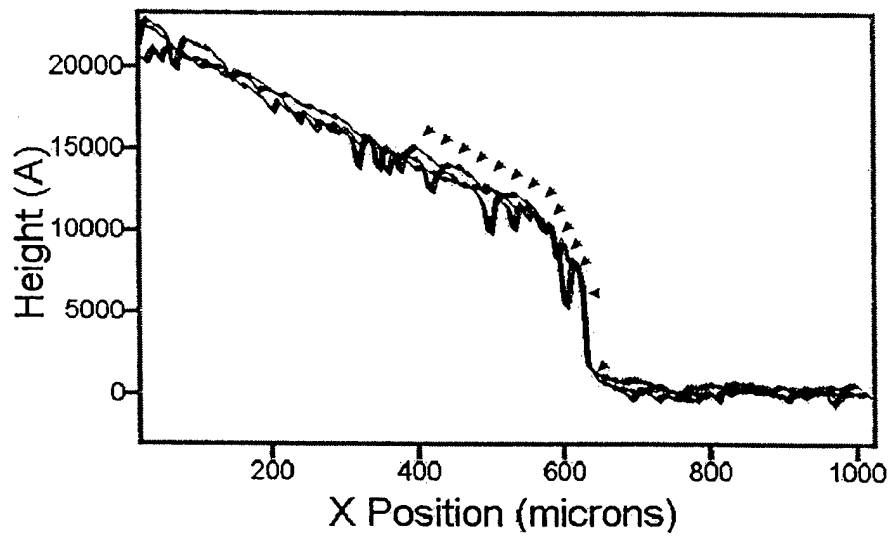


Figure 3: Three profilometry scans of epoxy mounted 2024 Sample 10 that has been Alodine treated for 1 minute. Sample 10 was polished metallographically, followed with  $0.05\mu\text{m}$  alumina on Buehler cloth and drying before Alodine treatment. The approximate Raman sampling point locations along the profile are indicated with arrows.

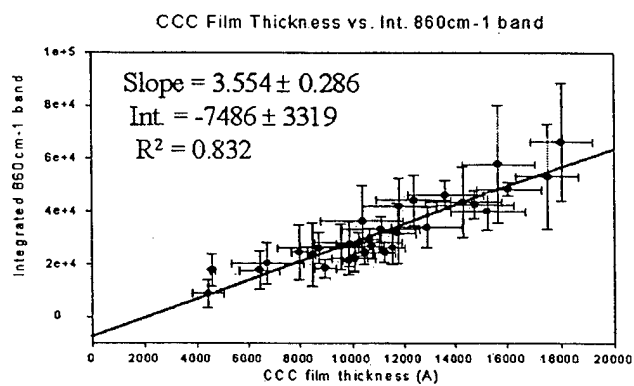


Figure 4: CCC thickness vs. the integrated 860cm<sup>-1</sup> Raman band. CCC thickness is obtained via profilometry of 2 different Alodine treated epoxy mounted 2024 samples.

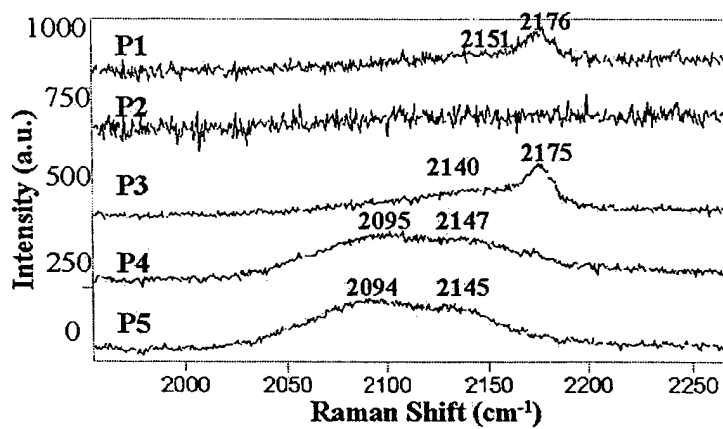


Figure 5: Average phase spectra zoomed in for CN Raman region. A 3 minute Alodine treatment was used.

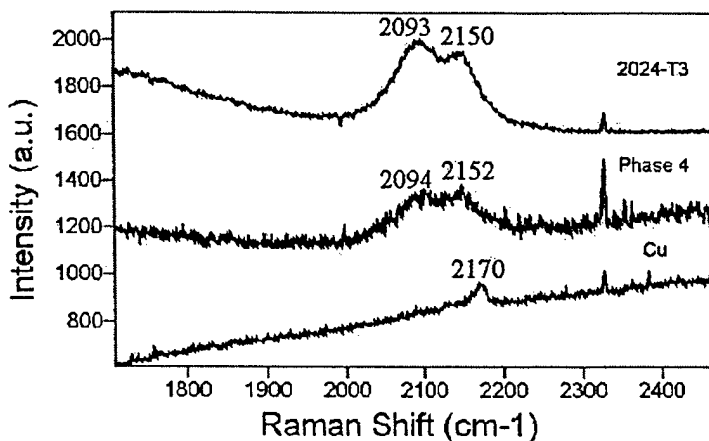


Figure 5b: Cyanide region bands of Alodine treated bulk 2024, Phase 4, and Cu. 514.5nm, 50x objective, 1800 line grating centered at 2100 cm<sup>-1</sup> for all spectra. 2024 and P4 were integrated for 25 s. x 2, with 2.85mW and 2.5mW respectively. Cu was integrated for 75 s. x 2 with 2.5mW. 2024, P4 and Cu had 10, 3 and 6 points spatially averaged. 2024 and P4 were treated for 5 minutes, Cu for 10 minutes. A nitrogen peak is present at 2328 cm<sup>-1</sup>.

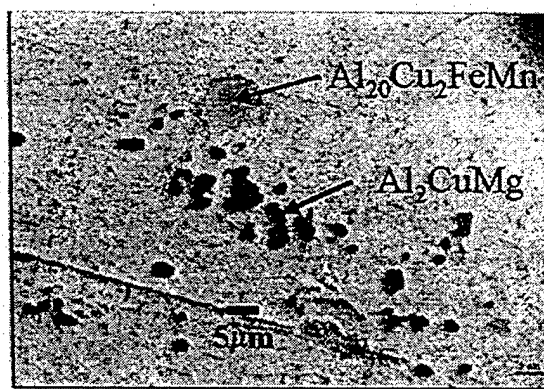


Figure 6: Optical image of the intermetallics on AA 2024-T3 Alloy. The larger lighter inclusions are depressed,  $\text{Al}_{20}\text{Cu}_2\text{FeMn}$ . The smaller darker ones are S-phase,  $\text{Al}_2\text{CuMg}$ .

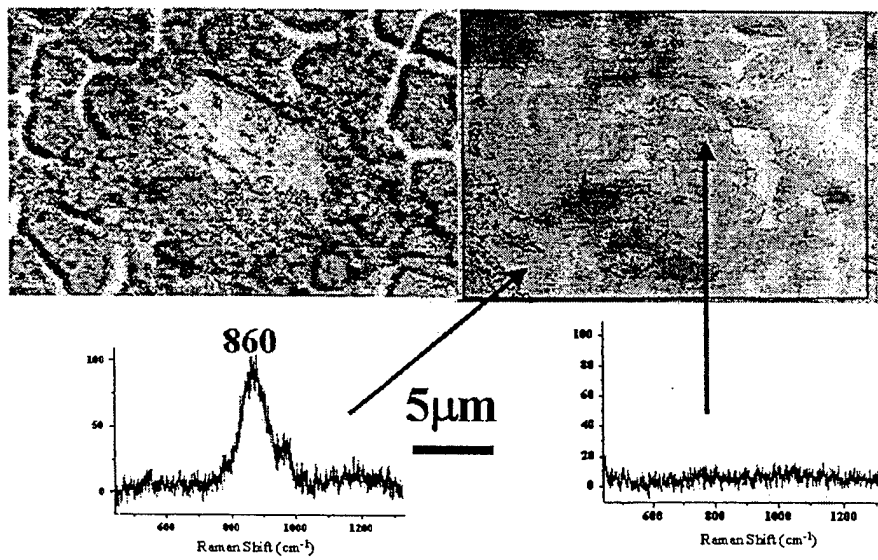


Figure 7:  $860\text{cm}^{-1}$  Raman map of a “depressed”  $\text{Al}_{20}\text{Cu}_2\text{FeMn}$  IMC on 2024 alloy, 100x objective, 100 s. x 2 per X row avg., 5-10mW at sample, 1800 line grating centered at  $900\text{cm}^{-1}$ , 15 x 13 grid, 514.5nm.

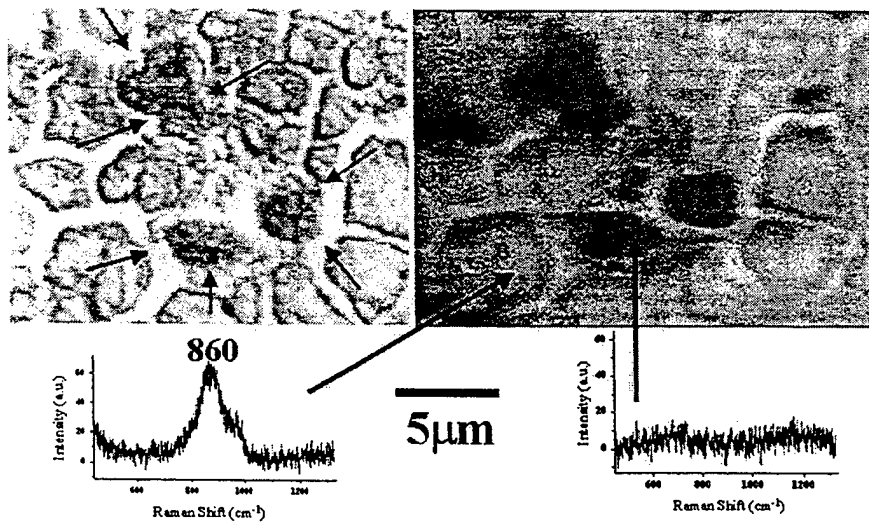


Figure 8: Raman  $860\text{cm}^{-1}$  map of S-phase intermetallics on 2024. A 17 x 18 grid was used.

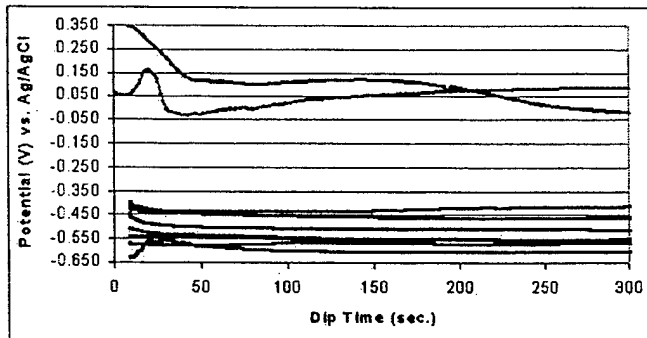


Figure 9: Ingot open circuit potential in Alodine solution. The lower 8 plots are normal runs after water polishing, centered around -51.5mV vs. Ag/AgCl. The top 2 plots are open circuit potentials after treatment with \*Alodine solution (including all Alodine components except Cr). The top 2 plots average endpoint is 26mV.

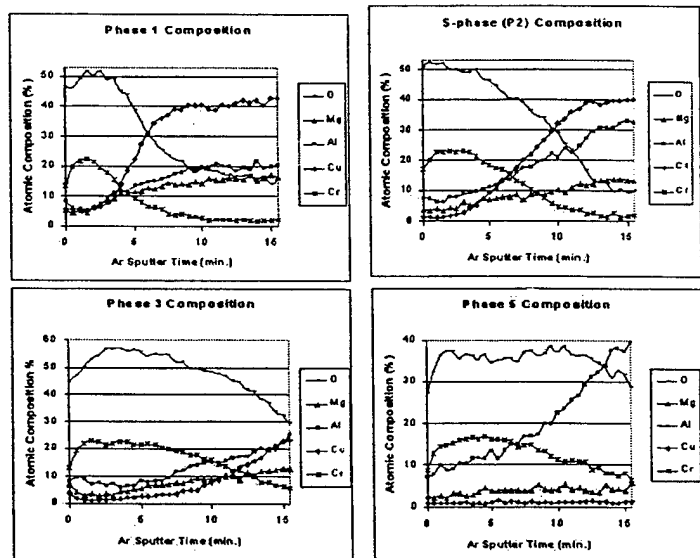


Figure 10: AES depth profiles of 3 second Alodine treatment on P1, P2, P3 and P5.

## **Measurement of Intermetallic Electrochemistry**

A. Sehgal, R. Leard, R.G. Buchheit, Department of Materials Science and Engineering, Ohio State University, 477 Watts Hall, 2041 College Rd., Columbus, OH 43210. Tel. (614) 292-6085, FAX (614) 292-9857, buchheit.8@osu.edu.

### **Abstract**

A comprehensive survey of intermetallic electrochemistry is currently underway. Twenty-one intermetallic compounds have been identified for synthesis and study. These compounds represent the most prevalent compounds found in high strength Al alloys. The information developed in this survey will be used to understand the role of microstructure in local dissolution phenomena during chromate metal finishing and chromate coating background. Two methods are being pursued for the study of IMCs. First, intermetallic compounds are being synthesized in bulk form so that conventional surface analytical and electrochemical techniques can be used for their study. Bulk IMC crystals are being prepared by casting and heat treating. To date, a range of IMCs have been successfully synthesized. Second, we are using a specially constructed electrochemical microprobe to make measurements on crystals as small as a 1  $\mu\text{m}$  in diameter. This enables measurement of IMC particles in real alloys and enables measurement of electrochemical behavior due to changing IMC composition in larger cored particles.

### **Intermetallics Study**

A variety of intermetallic compounds have been synthesized in bulk form to support a variety of experiments. IMCs synthesized are indicated in Table I. This table reports the open circuit potential reported for the IMC in aerated chloride solutions. Specific details of IMC electrochemistry can be found in other sections of this report.

### **Microcapillary cell development.**

A microelectrochemical cell, based on an earlier design (1), has been constructed to study electrochemical behavior of IMCs (Figures 1 – 3). This novel instrumentation permits accurate positioning of a micro-capillary on a metal surface. The contact area can be as small as a few square micrometers. Using this equipment, we will be able to study formation and breakdown of conversion coatings on individual intermetallic particles in high strength Al alloys. The equipment consists of a optical metallograph, specially outfitted so that one of the objective lenses is replaced with a glass microcapillary electrochemical cell, a high sensitivity potentiostat capable of pA current resolution, and a video imaging system. The video imaging capability enable the experimenter to locate a site suitable for analysis. The cell is then rotated into position and contacted with the surface site. Electrochemical measurements are then made.

Electrochemical measurements (cyclic voltammetry) on bulk intermetallics ( $\theta$  phase/Al<sub>2</sub>Cu), pure Al and Cu to characterize the effect of Alodine solution chemistry on formation of chromate conversion coatings (CCC).

## References

1) Suter, Thomas, Ph. D. Thesis, number 11962, ETH Zurich, 1997.

**Table I.** Al-based intermetallic compounds that have been synthesized and are under study in our laboratories. Open circuit potential measurements are also reported.

Phase	Environment	$E_{corr}$ (mV <sub>sce</sub> )	$E_{pk}$ (mV <sub>sce</sub> )
Al <sub>6</sub> Mn	Pitting in 0.5 M NaCl	-990	-573
	Pitting in 0.1 M NaCl	-630	-200
	Pitting in 0.05 M NaCl	-723	-688
Al <sub>2</sub> CuMg	Active dissolution/ dealloying in 0.5 M NaCl	-930	-
Al <sub>3</sub> Mg <sub>2</sub>	Passivity/breakdown in 0.5 M NaCl, pH = 3.3 - 13.5	-1262	-927
	Passivity/breakdown in 0.05 M NaCl	-1193	-885
Al <sub>2</sub> Cu	Dealloying in 0.05 M NaCl	-585	-541
Al <sub>7</sub> Cu <sub>2</sub> Fe	Passivity breakdown in 0.05 M NaCl	-537	-505
Al <sub>3</sub> Fe	Acitive dissolution in 0.1 M NaCl	-600	-300
MgZn <sub>2</sub>	Active dissolution in 0.05 M NaCl	-1000	-1000

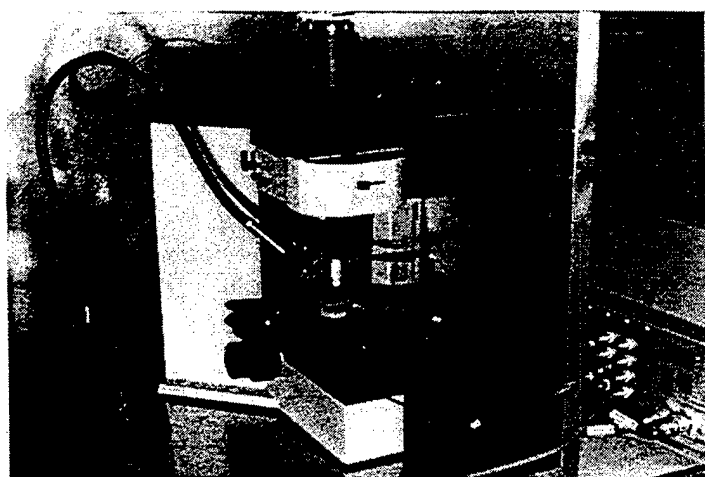


**Figure 1.** Microelectrochemical cell mounted on an optical metallograph and in a Faraday cage.

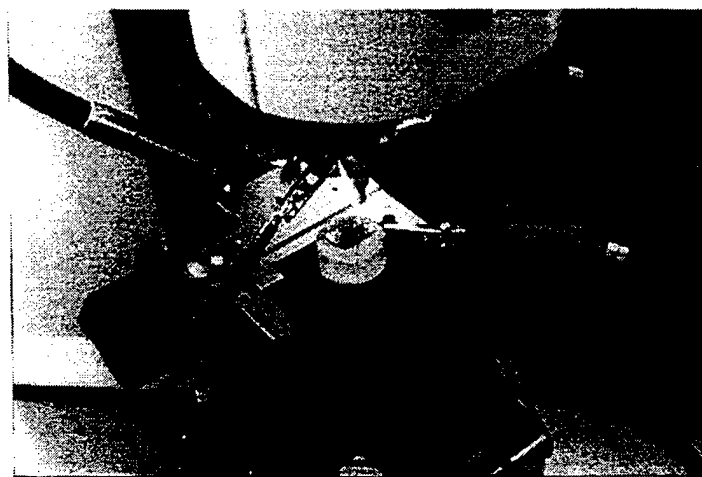


**Figure 2.** The microelectrochemical cell placed on a sample.

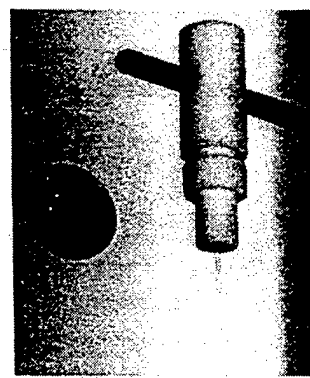


**Figure 3.** The microelectrochemical cell and glass microcapillary.

# **Thermal Stability and Aging Characteristics of Chromate Conversion Coatings on Aluminum Alloy 2024-T3**

V. Laget<sup>a</sup>, C. Jeffcoate<sup>b</sup>, H.S. Isaacs<sup>b</sup>, R.G. Buchheit<sup>a</sup> a) Dept. of Materials Science and Engineering, Ohio State University, Columbus, OH 43210, b) Dept. of Applied Science, Brookhaven National Laboratory, Upton, NY 11973.

## **Abstract**

XANES and electrochemical impedance spectroscopies were used in parallel to correlate the amount of Cr(VI) in chromate conversion coatings (CCC) on Al 2024 and their corrosion resistance in order to understand the degradation mechanisms upon aging or heating. Cr(VI) species appear to be immobilized for temperatures higher than 80°C due to dehydration. CCC are shown to be dynamic in the first month of aging with no significant dehydration. Another degradation mechanism involving chemical changes is to be considered.

## **Introduction**

Chromate conversion coatings (CCCs) are commonly used on all types of aluminum alloys in manufactured products ranging from aircraft to automotive components. These thin coatings (0.1 to 2  $\mu\text{m}$ ) are used as stand-alone corrosion resistant coatings, and as pre-treatments for painting. CCCs appear to provide both passive barrier protection by preventing an aggressive environment from contacting the alloy substrate, and active corrosion protection, in which the coating is able to self-repair. Active corrosion protection, also known as "self-healing", is a unique phenomenon exhibited by CCCs (1-4). It is thought to be related to a reservoir of labile Cr(VI) species (chromate or dichromate) located at the outer regions of the coating. Cr(VI) species can be released into the attacking solution and migrate to locally corroding areas to inhibit further damage. The inhibiting action involves reduction of Cr(VI) to insoluble Cr(III), which enables formation of a protective passive barrier film.

One of the key elements in the self-healing nature of CCCs is the stability and the mobility of the Cr(VI) reservoir. If this reservoir decomposes, or the release mechanism cannot be effective anymore, a major component of the corrosion resistance is lost. Gallacio et al. showed that loss of corrosion resistance occurs under salt fog testing at temperatures in excess of 75°C (5). At the same temperatures, they observed a dramatic decrease of the Cr(VI) amount released in corrosive solutions.

Effects of long term aging (> 24 hours) in ambient atmospheres at ambient temperatures are less clear but it is generally believed that corrosion resistance may also be lost (6, 7). Glass showed that the amount of Cr(VI) released in solution decreases by a factor 10 in one month (8).

Understanding the mechanisms and kinetics of the corrosion protection degradation with time and temperature has practical implications for the application and use of the coatings. The relationship between dehydration of the CCCs and the decrease of the amount of Cr(VI) released in solution is now commonly acknowledged. An organic coating covering the CCC during aging (8) and heating (9) treatments has been shown to limit this decrease. Also, corrosion resistance is not lost for coatings heated up to 100°C in a steam chamber (5). Dehydration leads to formation of micro-cracks across the surface and it is generally believed that the whole amount of Cr(VI) species is reduced in the self-healing process, in order to repair the damage (7).

In this work, we report X-ray absorption near edge structure (XANES) determination of Cr(VI) content in the CCCs upon heating and aging treatments and evaluate its relationship with corrosion resistance. We show that other mechanisms linked with dehydration or chemical changes should be also taken into account.

## Experimental

Coating Preparation. Panels of Al 2024-T3 (Cu 4.5%, Mg 1.5 % and Mn 0.6%) were cleaned in an alkaline bath ( $\text{Na}_2\text{SiO}_3$  32 g/l,  $\text{Na}_2\text{CO}_3$  48 g/l) at 65°C for 2 minutes, rinsed, deoxidized in a commercial Sanchem 1000 bath at 55°C for 3 minutes, rinsed and then finally treated in an Alodine 1200S chromating bath at room temperature for 1 to 3 minutes, rinsed and air-dried for 24 hours (hardening time). Alodine 1200S contains chromic acid (50-60%), fluoro salts (30-50 %) and  $\text{K}_3\text{Fe}(\text{CN})_6$  as an accelerator (10-15%) (4, 10).

Heating treatments were carried out during 15 minutes up to 500°C. For the aging study, samples were left in ambient laboratory atmosphere (20-25°C, 30-50% RH) for times up to 2 months.

TGA/DTA. Thermal analysis was performed with a SEICO model 320 on powders freshly scraped from the panels (coating time = 20 minutes). Measurements were made from RT to 550°C under air (flow 100 ml/min) with a heating rate of 5°C/min.

X-ray Absorption Spectroscopy. Cr(VI)/Cr ratio was determined by XANES at the Brookhaven National Laboratory on beam line X19A following well established procedures (2, 11). Reflected fluorescent intensity was recorded with a 13-element detector at the Cr K edge ( $E_0 = 5989$  eV) on samples tilted at 45° to the incident beam. Spectra were background subtracted and normalized so that the absorption coefficient, defined as fluorescent intensity over incident intensity is equal to 1 at  $E = 6050$  eV. A good estimation of the ratio of Cr(VI) over total Cr is then directly given by the height of the pre-peak.

Corrosion Measurements. The coating corrosion resistance,  $R_c$ , was determined by electrochemical impedance spectroscopy (EIS) with a EG&G PAR 273 potentiostat

coupled to a Solartron 1255 frequency response analyzer and Zplot software. Samples were left 24 hours in NaCl 0.5M before measurements. Panels were used as working electrodes whereas a platinum grid and a saturated calomel electrode were used as auxiliary and reference electrodes, respectively. The real and imaginary components of the impedance were recorded at the open circuit potential, using an a.c. perturbation of 10mV amplitude for frequencies ranging from 0.01 to 10000 Hz.  $R_c$  was deduced by integrating the imaginary component of the impedance (12). A good correlation is generally observed between EIS and salt spray testing (13-14).

Auger Electron Spectroscopy. AES was performed with a PHI-Perkin/Elmer 680 apparatus associated with Ar ion gun for depth profiles in order to get an estimation of the thickness and to follow the depth repartition of the elements C, O, Al (KLL peaks) and Cr (LMM peak) inside the coatings. The interface was defined as the moment when the aluminum metallic peak (at 1395 eV) dominated the oxide peak (at 1387 eV). Measurements were made with a 10kV 1nA electron beam, a sputtering rate of 27 nm/min and on sample areas without any cracks.

## Results and Discussion

### Heating Study

Fig. 1 shows the TGA/DTA measurements made on CCC powders up to 550°C. The compound suffers a total weight loss of 48 % in three distinct steps in agreement with a previous report (15). A first endothermic process occurs at ca. 80°C, corresponding to the loss of water molecules (18% weight loss). The second process is strongly exothermic and occurs at 300°C. A noticeable odor of NH<sub>3</sub> and HCN was reported (15), suggesting the decomposition of the ferri/ferro-cyanide groups incorporated in the coating bath as accelerator. At 450°C, the third weight loss is observed, associated with an exothermic peak of variable intensity depending on sample. This transformation is referred in the literature as the onset of  $\alpha$ -Cr<sub>2</sub>O<sub>3</sub>, also called "glow phenomenon"(16). It has been shown to be very sensitive to the chemical environment (16, 17).

The initial composition of the coating is often referred as a hydrated chromium oxide consisting, according to XPS results, in a variable mixture of Cr<sub>2</sub>O<sub>3</sub>.nH<sub>2</sub>O, CrOOH or Cr(OH)<sub>3</sub> (7, 18, 19). Both Cr<sub>2</sub>O<sub>3</sub>.nH<sub>2</sub>O and Cr(OH)<sub>3</sub> have been reported to decompose upon dehydration to a CrOOH intermediate form (20, 21). Loss of water is observed by condensation of the hydroxyl group in CrOOH at 250°C (21). This decomposition is a slightly endothermic process, very often hidden by more energetic transformations and thus is not observed in our measurements. CCCs are amorphous in the entire range of studied temperatures. The first X-ray diffraction diagram is obtained at 600°C, corresponding well to partially crystallized Cr<sub>2</sub>O<sub>3</sub>. Coating thickness measurements determined by AES profiles show a strong decrease up to 100°C and no significant variation after 100°C. A one-minute coating CCC was measured varying from 350 nm to 200 nm during the dehydration process.

The correlation between the Cr(VI)/Cr ratio determined by XANES and the corrosion resistance is showed on Fig. 2. Regarding the variation of the curves, two zones of study may be defined, below or above a certain temperature between 250 and 300°C, where clearly two behaviors are observed. This critical temperature may be associated with the second decomposition process observed in TGA/DTA at 300°C.

The Cr(VI)/Cr ratio does not show an abrupt decrease at 80°C, which might be expected to explain the decrease of Cr(VI) release in solution. Instead, it exhibits a slow and progressive decrease from 32% to 20% up to 250°C, showing that a significant part of the chromate was reduced with temperature (a 10-12 % value is generally obtained for a pure Cr(III) compound (2)). The variation of the corrosion resistance is quite different;  $R_c$  decreases by two orders of magnitude at 80°C. It seems that the corrosion resistance value is strongly related with the release of the Cr(VI) species and hence the self-healing effect. Both are very low between 80 and 200°C whereas a relatively high amount of Cr(VI) (26 to 32 %) is still present inside the coating. This clearly shows that the reduction of the Cr(VI) species is not the main factor of the corrosion degradation. Cr(VI) species appear to be immobilized suggesting that chemical changes inside the coating due to moderately elevated temperature prevent their release.

The temperature at which those changes are observed corresponds to the first transformation measured by TGA, associated with dehydration. Water molecules could be directly involved in the mechanism of release of chromates in solution. A mechanism of release based on Raman spectroscopy and requiring water molecules to break covalent Cr(VI)-O-Cr(III) bonds has been suggested by McCreery et al (22). This would be in good agreement with previous works cited in the introduction, which show the importance of dehydration.

Above 250°C, the Cr(VI)/Cr ratio exhibits a strong increase and its value at 400°C is comparable to the one measured at room temperature. Clearly, a Cr(III) oxidation process is triggered. The corrosion resistance increases in parallel, showing a good correlation between the two parameters. After 400°C, the CCC is getting close to a  $\text{Cr}_2\text{O}_3$  composition and both Cr(VI) content and  $R_c$  decrease again.

The oxidation of Cr(III) to Cr(VI) or even possibly to intermediate valency such as IV or V, is a surface phenomenon well known from work on chromium-based catalysts (16, 20, 21, 23, 24). The exact nature of the intermediate compound has not been yet clearly established but it seems to depend on the Cr(III) starting compound and his chemical environment (25). Several works suggest that it could be a mixed valency (III and VI) oxide such as the chromium chromate  $\text{Cr}_2(\text{CrO}_4)_3$  (21, 24). The mechanism of release of chromates is expected to be different (not requiring any water molecules) from the one existing at temperatures below 250°C. The Cr(VI) species are present at the surface of the coating and hence, could easily be released in the self-healing process.

The evolution of the corrosion resistance with temperature was also measured for a CCC on Al 1100 panels (99% Al, 1% Fe, Cu, Si) to assess any influence of the alloy composition on heating. The comparison with CCC on Al 2024 is shown Fig. 3. The corrosion resistance of coated Al 1100 panels does not decrease around 250°C, suggesting insensitivity to dehydration.  $R_c$  starts to decrease only after 300°C when the coating is tending towards its Cr(III) oxide final form. This stability may be only due to the fact that Al 1100 is much less sensitive to corrosion than Al 2024. Indeed, the high content of copper in Al 2024 enhances its strength but also its corrosion sensitivity by local galvanic action. Nevertheless, specific interaction between CCC and intermetallic particles in Al 2024 has been observed. CCC is not uniform all over the surface but thinner on the Cu-rich particles (26, 27). Hagans and Haas observed a strong presence of Fe on those particles suggesting the formation of a Cu-ferrocyanide complex (26). Regarding our results, CCC degradation may be also dependent of the alloy composition. The details of its mechanism are not yet resolved.

### Aging Study

The same type of study was performed on samples aged in air to check their stability and determine whether the same mechanisms of degradation as those involved with moderately elevated temperatures were to be considered. XANES was performed on a sample aged for 5 months and the Cr(VI)/Cr ratio was measured to be 31 %. This value is very close to the one obtained on a fresh sample (32%), showing that no significant reduction of the chromates occurs upon aging. TGA/DTA was also performed on sample aged for two months and surprisingly, the total weight loss and the weight loss related to dehydration remain the same, respectively 48 % and 20 %. This would show that dehydration can not be the leading factor to explain the decrease of the amount of Cr(VI) released in solution in the first month of aging. Some of the hydroxide groups may decompose at lower temperatures, distorting the hydration rate measured by TGA. Although the plateau between the two weight loss events is less clear for an aged sample compared to a fresh one, the differential of the TGA (DTG) for the first weight loss remains very well centered around 80°C, suggesting that only water molecules from hydration are taken into account. Previous XPS study of the oxygen peak shows similar results: Kearns et al. did not observe any significant change in dehydration after 35 days, compared to a 24-hour old sample (28).

The evolution of the corrosion resistance on samples aged up to 2 months is shown Fig. 4 for two coating thicknesses. For 1 minute coating time samples,  $R_c$  decreases after 20 days from values between 2 and  $3 \times 10^6$  ohms.cm<sup>2</sup> to values in the order of  $5 \times 10^4$ . No significant changes were observed for 3 minutes coating time samples. In this last case, the good stability of the corrosion resistance may be explained by the fact that a low but possibly sufficient Cr(VI) amount can be released in solution for the self-healing process. For thinner coatings, less chromates are available and their immobilization appears to result in the total loss of the corrosion protection properties. More tests remain to be done to check this behavior.

Coating thickness exhibits a different evolution from that expected regarding the study with temperature : instead of decreasing, it increases markedly with time, from 400 to 650 nm during the first month (1 minute coating time sample), indicating some chemical change inside the coating. Then it remains steady between 600 and 650 nm. It is interesting to note that both the decrease of the Cr(VI) released in solution and the increase of the thickness occur in the first month (8). After this limit, both show little change. A correlation between the two parameters is to be considered, as if the chemical changes were responsible of the immobilization of the chromates. Those changes require further investigation. Among them, we observed by AES than the thickness of the inner layer where the Al-Cr mixed oxide is detected increased strongly, from 150 to 300 nm. Thus, an oxidation of metallic aluminum will explain partially the increase of the total thickness. Many important chemical and physical changes are observed during the first 24 hours of the coating life, which are also the setting and hardening time of the coating (28). The first month period could be a prolongation of those changes, on a smaller scale.

## Conclusions

Reduction of Cr(VI) species has been observed between RT and 250°C. Nevertheless, our results show that it is not the main factor of degradation of the corrosion resistance above 80°C. Dehydration seems to cause immobilization of the chromates, which can not be released anymore in the "self-healing" process. Some influence of the alloy composition on the degradation mechanism has been observed but remains to be fully resolved.

No significant reduction of the Cr(VI) species or dehydration have been detected with time under ambient conditions. The immobilization of the Cr(VI) species due to chemical changes other than dehydration is to be considered. The increase of the thickness during the first month suggests that CCCs are still dynamic. Aluminum oxidation has been observed at the interface metal/coating. The mechanisms of chromates immobilization upon aging may be related to those changes but remain to be determined.

## Acknowledgements

This work is supported by the Army Research Office and the Strategic Environmental Remediation and Development Program under contract no. DACA-72-99-C-0002.

## References

1. P.L. Hagans and C.M. Haas, ASM Handbook, Vol. 5, p. 405, ASM international, Metals Park, OH (1994)
2. M.W. Kendig, A.J. Davenport and H.S. Isaacs, Corros. Sci., **34**, 41 (1993)
3. J. Zhao, G. Frankel and R.L. McCreery, J. Electrochem. Soc., **145**, 2258 (1998)
4. F.W. Lytle, R.B. Gregor, G.L. Bibbins, K.Y. Blohowiak, R.E. Smith and G.D. Tuss, Corros. Sci., **37**, 349 (1995)
5. A. Gallacio, F. Pearlstein and M.R. D'Ambrosio, Met. Finish., Aug., 50 (1966)
6. L.F.G. Williams, Surf. Technol., **7**, 113 (1978)
7. A.E. Hughes, R.J. Taylor and B.R.W. Hinton, Surf. Interf. Anal., **25**, 223 (1997)
8. A.L. Glass, Mat. Protect., July, 26 (1968)

9. F. Pearlstein and M.R. D'Ambrosio, Plating, **55**, 345 (1968)
10. Material Safety Data Sheet for Alodine 1200S
11. J.K. Hawkins, H.S. Isaacs, S.M. Heald, J. Tranquada, G.E. Thompson and G.C. Wood, Corros. Sci., **27**, 391 (1987)
12. M. Kendig and F. Mansfeld, Corros., **39**, 466 (1983)
13. R.G. Buchheit, M. Cunningham, H. Jensen, M.W. Kendig and M.A. Martinez, Corros., **54**, 61 (1998)
14. G.M. Treacy, G.D. Wilcox and M.O.W. Richardson, Surf. Coat. Technol., **114**, 260 (1999)
15. N.J. Newhard, Met. Finish., July, 49 (1972)
16. J.D. Carruthers, K.S.W. Sing and J. Fenerty, Nature, Jan., 66 (1967)
17. V.V. Viktorov, A.A. Fotiev and I.V. Evdokimov, Inorg. Mat., **30**, 82 (1994)
18. J.A. Trevorton and N.C. Davies, Met. Technol., Oct., 480 (1977)
19. K. Asami, M. Oki, G.E. Thompson, G.C. Wood and V. Ashworth, Electrochim. Acta, **32**, 337 (1987)
20. M.I. Zaki and N.E. Fouad, Thermochim. Acta, **95**, 73 (1985)
21. P. Ratnasamy and A.J. Leonard, J. Phys. Chem., **76**, 1838 (1972)
22. L. Xia and R.L. Mc Creery, J. Electrochem. Soc., **145**, 3083 (1998)
23. S.L.M. Schroeder, G.D. Moggridge, T. Rayment and R.M. Lambert, J. Phys. IV, **7**, C2-923 (1997)
24. P.G. Harrison, N.C. Lloyd, W. Daniell, C. Bailey and W. Azelee, Chem. Mater., **11**, 896 (1999)
25. M. Maciejewski, K. Kohler, H. Schneider and A. Baiker, J. Solid State Chem., **119**, 13 (1995)
26. P.L. Hagans and C.M. Haas, Surf. Interf. Anal., **21**, 65 (1994)
27. J.R. Waldrop and M.W. Kendig, J. Electrochem. Soc., **145**, L11 (1998)
28. J.R. Kearns, D. Chidambaram, M.J. Vasquez, G.P. Halada and C.R. Clayton, 3<sup>rd</sup> annual report, p. 179, AFOSR MURI (1999)

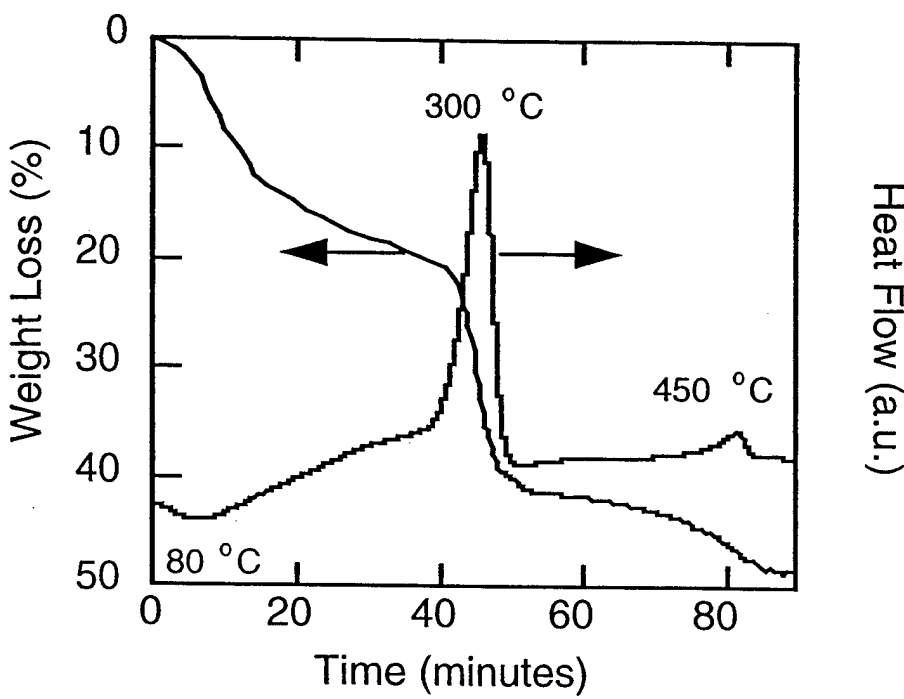


Figure 1: TGA and DTA measurements for Alodine 1200S chromate conversion coating under its powder form.

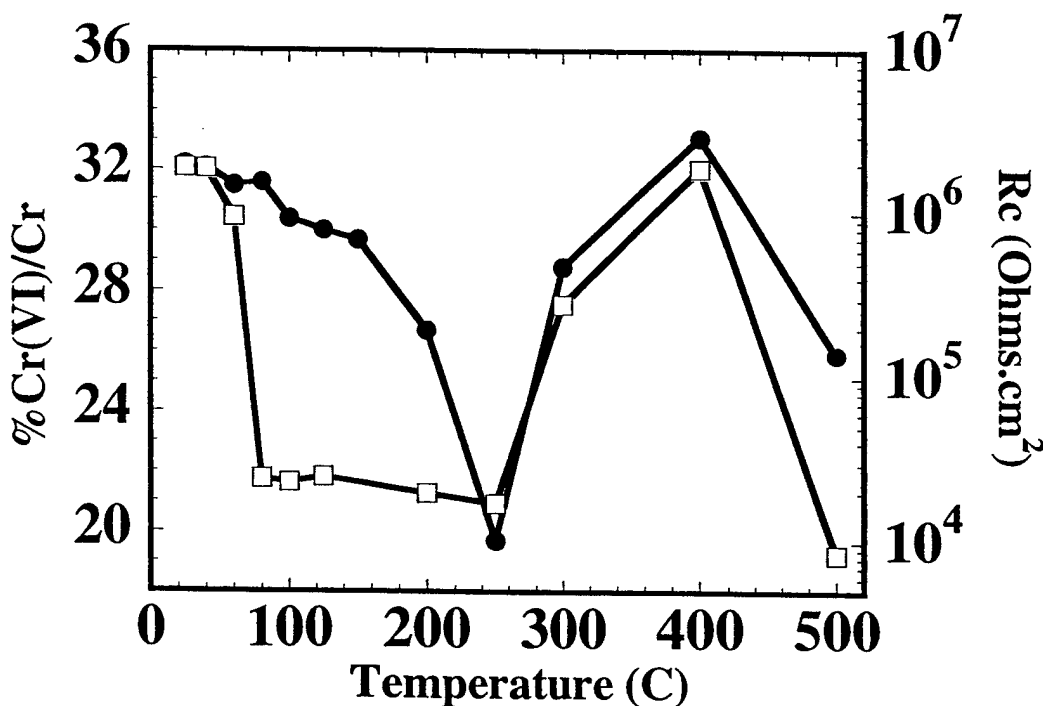


Figure 2: Evolution with temperature of the Cr(VI)/Cr ratio determined by XANES (●) and the corrosion resistance (◻) for CCC with 3 minutes coating time.

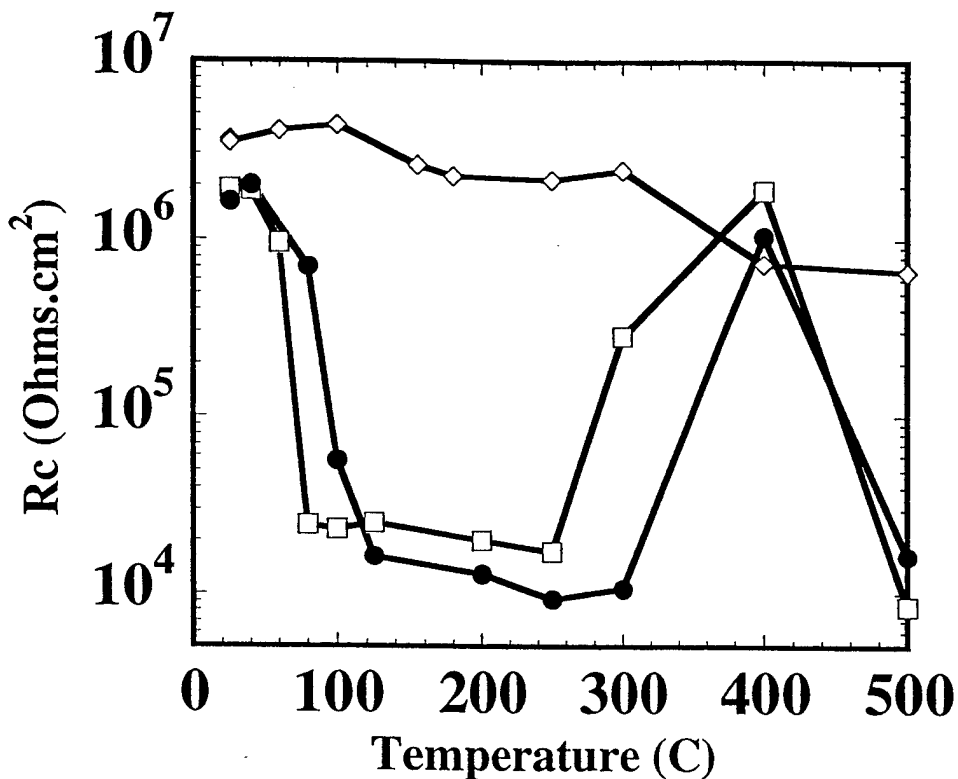


Figure 3: Evolution of the corrosion resistance for CCC on Al 2024, with respectively 1 min (●) and 3 min (◻) coating time, on Al 1100 (■) with 3 min coating time.

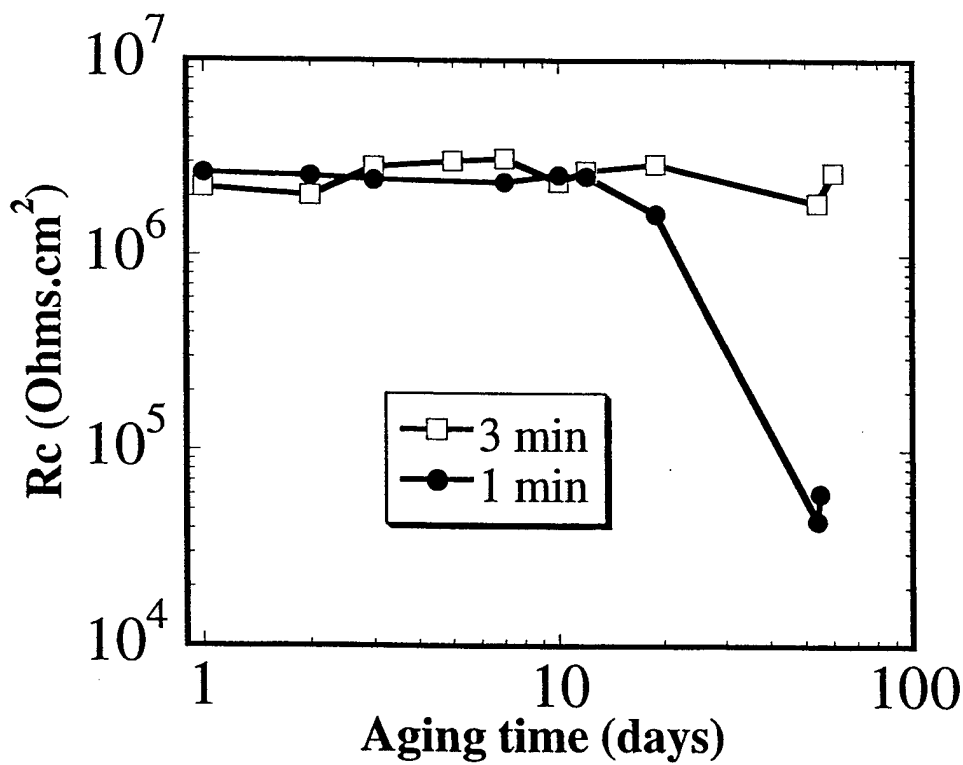


Figure 4: Evolution of the corrosion resistance with aging time for CCC on Al 2024 with 1 min (●) and 3 min (◻) coating time.

## **Vibrational Spectroscopy of Chromate Coatings for Both Characterization and Nondestructive Evaluation**

J. Wu<sup>†</sup>, R.L. McCreery<sup>†</sup>, R. G. Buchheit<sup>††</sup>, <sup>†</sup>Department of Chemistry, <sup>††</sup>Department of Materials Science and Engineering, Ohio State University, Columbus, OH 43210, Tel. (614) 292-2021, mccreery.2@osu.edu.

### **Background**

Raman and Infrared spectroscopy provide information about molecular structure and composition of bulk materials and thin films, with high structural specificity. Raman has provided valuable information about chromate conversion coatings in past efforts, including new structural models and an understanding of chromate storage and release as an active inhibitor (1-5). Raman spectroscopy is also useful for characterizing organic components of coating systems, although this feature has not been exploited in the past. An added feature of Raman Spectroscopy is the possibility of nondestructive evaluation (NDE) of intact coatings in the field, using a hand-held compact spectrometer. The current effort is directed toward molecular characterization of coating systems during application and curing, with the objective being a quantitative, chemically specific monitor of coating composition and quality. In addition, Raman monitoring of changes in the coating during salt spray and UV testing are correlated with traditional, destructive measures of coating integrity and substrate corrosion.

### **Objectives**

1. Establish reference vibrational spectra of common coating materials, particularly SrCrO<sub>4</sub>, CCC's, Epoxy, etc.
2. Observe spectral changes during epoxy curing.
3. Examine changes in spectroscopy of coatings during salt spray testing and UV exposure.
4. Correlate spectroscopic results with traditional impedance observations, to assess Raman spectroscopy for NDE.

### **Procedures**

Coupons of AA 2024-T3 coated by Richard Granata using standard methods were used as samples. They included untreated alloy, alloy + CCC, and alloy + CCC + SrCrO<sub>4</sub>/epoxy (DEFT (40% SrCrO<sub>4</sub>) and 5% SrCrO<sub>4</sub>). CCC's were applied using standard "Alodine" baths, while chromated epoxy was applied as "DEFT" coating according to manufacturer's recommendations. Shell 828 epoxy and 3141 hardener were used as received, and all other chemicals were reagent grade. The salt spray test was ASTM B117-90, operating at 35 °C with 5 wt% NaCl spray and a steady state relative humidity of approximately 95—98%. UV exposure was according to ASTM G53-91,

with a cycle of 8 hr UV (UV-B313 nm bulbs) at 70 °C followed by 4 hr condensation at 50 °C.

Raman spectroscopy was conducted with either 785 nm (Chromex 2000 spectrometer) or 1064 nm (Bruker IFS 66 spectrometer) laser excitation. The instruments are commercially available and were unmodified. Laser power at the sample was typically 50 mW (785nm) or 245 mW (1064 nm), and spectral resolution was 2-6  $\text{cm}^{-1}$ .

Impedance measurements were conducted with a Solartron Model 1255 frequency response analyzer, an EG&G PAR 273 potentiostat and Zplot software. A graphite counter electrode and a Ag/AgCl saturated reference electrode were used. EIS measurements were performed in the frequency range of 100 kHz to 3 mHz. The electrochemical cell consisted of a Teflon cylinder fitted with an O-ring sealed to the panels with a sample area of 0.32  $\text{cm}^2$ .

## Results

Reference spectra for various chromate compounds, epoxy coatings, and a CCC are shown in figures 1-3. Raman provides quite distinct spectra of materials with similar structure, and organic species are easily distinguished from the chromates either in solution or as solids. The peak height is linear with concentration in many situations, particularly for thin films where laser absorption is minimal. Raman spectra are also amenable to library searching, in which "unknown" spectra are compared to reference spectra to identify which coating components. We have demonstrated this capability for pharmaceuticals, in which commercial software rapidly (~3 seconds) and correctly identified organic solids from a library of 312 standard spectra (6). Of immediate relevance is a comparison of Raman spectra for  $\text{SrCrO}_4$ , CCC, and  $\text{SrCrO}_4$ /epoxy coating (DEFT). The  $\text{SrCrO}_4$  is easily observed, as are CCC and epoxy components. Changes in composition and molecular structure become apparent from changes in these spectra with salt spray or UV exposure.

An example of nondestructive monitoring of epoxy curing is shown in figures 4 and 5. The reaction between the epoxy resin and hardener changes the structure of the epoxide ring during curing, leading to a change in the Raman band intensity at 1255  $\text{cm}^{-1}$  (figure 4). The intensity of the 1255  $\text{cm}^{-1}$  band relative to a nearby band which does not change with time (1186  $\text{cm}^{-1}$ ) is shown in figure 5. The 1186 band acts as an internal standard, and changes in the 1255/1186 intensity ratio indicate the extent of the curing reaction. From Figure 5, the reaction appears complete after about 30 hours at room temperature. For coating conditions where the temperature or reagent composition may vary, the Raman spectrum might provide a nondestructive means to monitor curing progress. It should be emphasized that these spectra were obtained with a commercial instrument requiring minimal operator training. A fiber optic probe is available for field operation, with a probe head the size of a common flashlight.

The top spectrum of figure 6 is from a "DEFT" (40%  $\text{SrCrO}_4$  in 828 epoxy) coating on AA2024 alloy pretreated with a CCC. The  $\text{SrCrO}_4$  Raman bands ( $800\text{-}950\text{ cm}^{-1}$ ) and epoxy bands ( $1000\text{-}1700$  and  $2700\text{-}3100\text{ cm}^{-1}$ ) are readily observable, in this case with FT-Raman at 1064 nm. After four days in a salt spray chamber, the epoxy bands are unchanged, but the  $\text{SrCrO}_4$  bands decrease in height by about 20%. The difference spectrum shows that the spectral changes are almost exclusively due to  $\text{SrCrO}_4$  loss. The DEFT film is hydrated by the salt spray (see below), but the epoxy structure changes little. Water is a weak Raman scatterer, so the DEFT spectrum shows little change with salt spray exposure, other than leaching of  $\text{SrCrO}_4$ . Since  $\text{SrCrO}_4$  is one of the active corrosion inhibitors in DEFT/CCC coating, Raman spectroscopy provides a quantitative, nondestructive assessment of inhibitor content.

A technical problem with Raman sampling in the small sample spot ( $\sim 100\text{ }\mu\text{m}$  diameter) usually observed in a given experiment. If there are heterogeneities in the coating from  $\text{SrCrO}_4$  particles or epoxy nonuniformity, small intensity variations occur when different spatial regions on the sample are observed. This leads to the baseline irregularities apparent in the difference spectrum of figure 6. The problem is reduced significantly by spinning the sample so a larger area is observed and heterogeneities are averaged (Figure 7). The same improvement occurs when a line rather than point focus is used, or if the beam is rastered over a larger sample area. These improvements are easily implemented in field applications by addition of a cylindrical lens to the fiber optic probe.

### **Electrochemical Impedance Spectroscopy (EIS)**

EIS was used to monitor salt spray effects on AA2024 samples, in order to monitor coating integrity and associated damage. Figure 8 shows impedance spectra and (Nyquist) plots for epoxy coated AA2024 exposed to salt spray for periods of 0 to 17 days. An example of a fit of the impedance data to a standard model is shown in Figure 9. The coating capacitance ( $C_{\text{coat}}$  - T) and pore resistance ( $R_{\text{pore}}$ ) are of particular interest, since they indicate permeation of the film and water content (7).  $R_{\text{pore}}$  and  $C_{\text{coat}}$  determined from plots similar to those in figure 9 are plotted in figure 10 for a range of salt spray exposure times. The trends shown in figure 10 indicate a decrease in  $R_{\text{pore}}$  as the film is permeated by salt water, and an increase in  $C_{\text{coat}}$  due to higher water content. The samples used to construct figures 8-10 were immersed in 0.5 M NaCl for 9 hours after the salt spray exposure to permit stabilization. Of the impedance results, but this time can be reduced significantly. Similar results are obtained after a 2 hour immersion, and we plan experiments where this stabilization time is reduced to a few minutes (see "future plans").

While EIS provides a good measure of coating status and alloy corrosion, it is time consuming, destructive, and impractical for field use. Since Raman spectroscopy is a possible NDE method applicable in the field, the question arises of how Raman spectral changes correlate with EIS indicators of film integrity and corrosion protection. Figure 11 shows a first attempt at such a correlation, in which a peak ratio from Raman and  $R_{\text{pore}}$  from EIS are plotted vs. salt spray exposure, and it reflects the spectral changes noted in figure 6 and 7. In this case, the  $893/2900$  Raman ratio tracks the loss of  $\text{SrCrO}_4$  relative

to the epoxy matrix.  $R_{pore}$  shows a similar trend, with the largest change occurring during the first day of salt spray exposure. It is likely that both the  $\text{SrCrO}_4$  content and the pore resistance decrease together, because they both depend on permeation of the film by saltwater. The correlation is quite promising, and we are currently refining the spectroscopic precision as well as the timing of the measurements (see "Future Plans").

Figure 11 shows spectral changes that result from UV exposure in a condensing atmosphere. Not only does the  $\text{SrCrO}_4$  level decrease, but there are changes in the epoxy spectrum as well. We expect UV light to photodegrade an organic film, so changes to the epoxy matrix are not surprising. The loss of  $\text{SrCrO}_4$  may be due to either photodegradation or leaching into the condensed water.

We have many more experiments planned for Raman monitoring of UV and salt spray effects on coating, but some initial conclusions are available. The salt spray permeates the DEFT coating, with relatively little effect on the epoxy matrix.  $\text{SrCrO}_4$  slowly dissolves into the salt spray, and its loss may be monitored with Raman. UV exposure appears to degrade the epoxy matrix and cause an accompanying loss of  $\text{SrCrO}_4$ . At least for the salt spray treatment, the Raman results correlate with impedance changes, and Raman may provide a nondestructive probe of the anticorrosion properties of the coating.

## Conclusions

1. Raman spectra of a variety of coatings may be obtained with commercial spectrometers, in a few seconds.
2. Raman spectra can detect molecular changes during epoxy curing.
3. Detailed "fingerprints" from Raman spectroscopy should permit identification of coatings, as well as structural changes during weathering.
4.  $\text{SrCrO}_4$  loss and photochemical epoxy breakdown may be monitored nondestructively and quantitatively with Raman spectroscopy.
5. Raman spectral changes correlate with impedance results, raising the prospect of Raman NDE of integrity, composition, and anticorrosion properties of coating systems.

## References

1. J. Zhao, G. Frankel and R.L. McCreery, "Corrosion Protection of Untreated AA-2024-T3 in Chloride Solution by a Chromate Conversion Coating Monitored with Raman Spectroscopy" *J. Electrochem. Soc.*, **1998**, 145, 2258-2264.
2. L. Xia and R.L. McCreery, "Chemistry of a Chromate Conversion Coating on Aluminum Alloy AA2024-T3 Probed by Vibrational Spectroscopy", *J. Electrochem. Soc.*, **1998**, 145, 3083-3089.

3. L. Xia, E. Akiyama, G. Frankel, R.L. McCreery, "Storage and Release of Soluble Hexavalent Chromium from Chromate Conversion Coatings: Equilibrium Aspects of Cr<sup>VI</sup> Concentration", submitted for publication.
4. J. D. Ramsey, R. L. McCreery "In-situ Raman Microscopy of Chromate Effects on Corrosion Pits in Aluminum Alloy" <http://fluo.univ-lemans.fr:8001/chimie/chimistes.html> *J. Electrochem. Soc.*, **1999**, 146, 4076-4081
5. Lin Xia, Richard L. McCreery, "Structure and Function of Ferricyanide in the Formation of Chromate Conversion Coatings on Aluminum Aircraft Alloy", *J. Electrochem. Soc.*, **1999**, 146, 3696-3701.
6. R.L. McCreery, A.J. Horn, J. Spencer, E. Jefferson, "Noninvasive Identification of Materials inside USP Vials with Raman Spectroscopy and a Raman Spectral Library", *J. Pharm. Sci.*, **1998**, 87, 1-8.
7. F. Mansfeld, M. W. Kendig, S. Tsai, "Evaluation of Corrosion Behavior of Coated Metals with AC Impedance Measurements", *Corrosion-NACE*, **1982**, 38(9), 478-485.

### **Current and Future Plans**

1. Repeat the correlation between Raman spectra and Impedance results (figure 11) with better time resolution after the salt spray. Examine changes occurring within first 24 hours of salt spray, without extended immersion in saltwater.
2. Develop internal Raman standard for absolute quantification of Raman changes, rather than the peak ratios used above. For example, part of each sample could be masked from the salt spray or UV exposure, then the untreated region could act as a standard indication the initial Raman spectrum. A practical application of this approach is the comparison of the spectrum of a protected region of an aircraft (such as the inside of an access panel) to the exposed exterior.
3. Relate impedance results to water uptake in the coatings, by monitoring the dielectric constant of the film.
4. Observe corrosion damage for coated samples exposed to UV and/or salt spray testing for extended periods. Correlate the appearance of pits or the reduction in corrosion resistance to Raman spectral changes.
5. Characterize and quantify changes in film structure and performance during UV exposure, and relate them to observable Raman changes.
6. Test a hand-held fiber optic probe currently available in our lab to NDE of coatings based on Raman spectra.

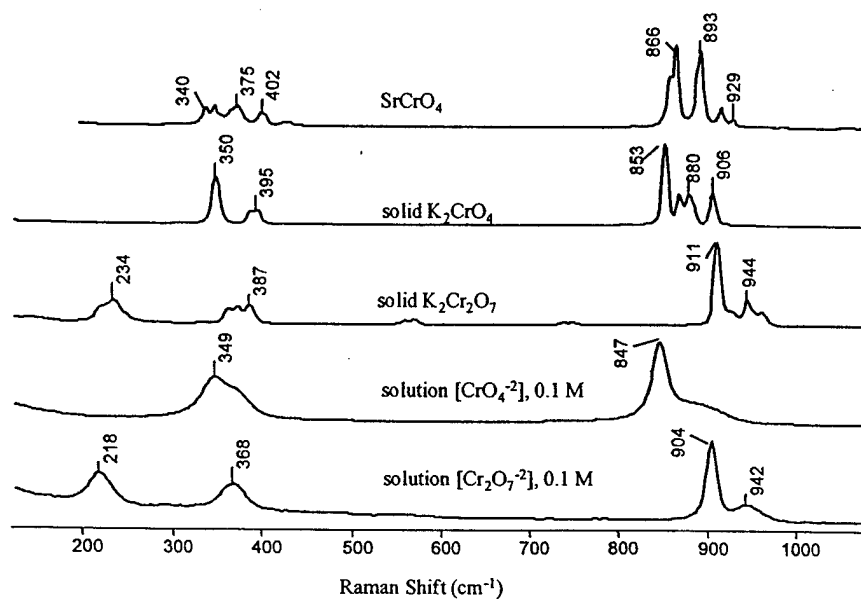


Figure 1 : Reference Raman spectra of chromate compounds. 785 nm, 50 mW, 1-30 second acquisition times. Chromex 2000 spectrometer.

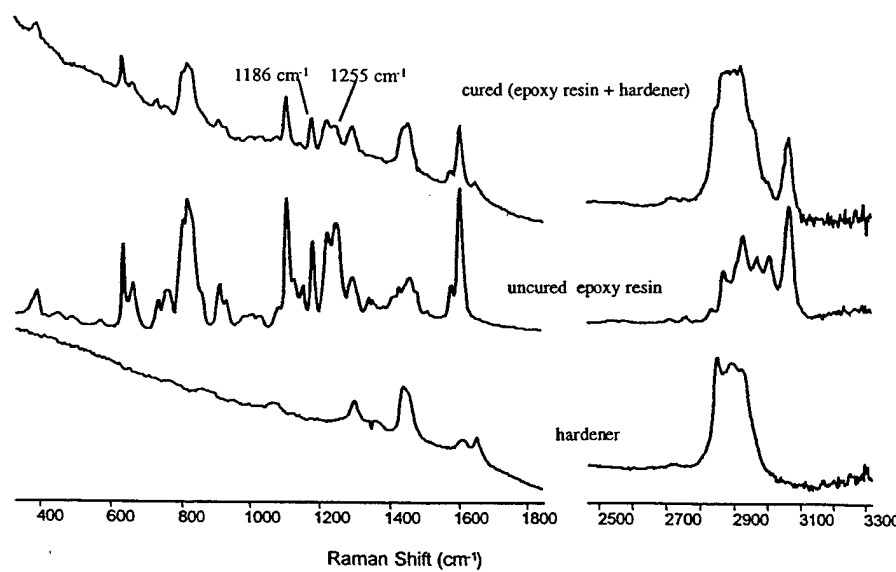


Figure 2 : Reference Raman spectra of epoxy compounds. 785 nm, 50 mW, 1-30 second acquisition times. Chromex 2000 spectrometer.

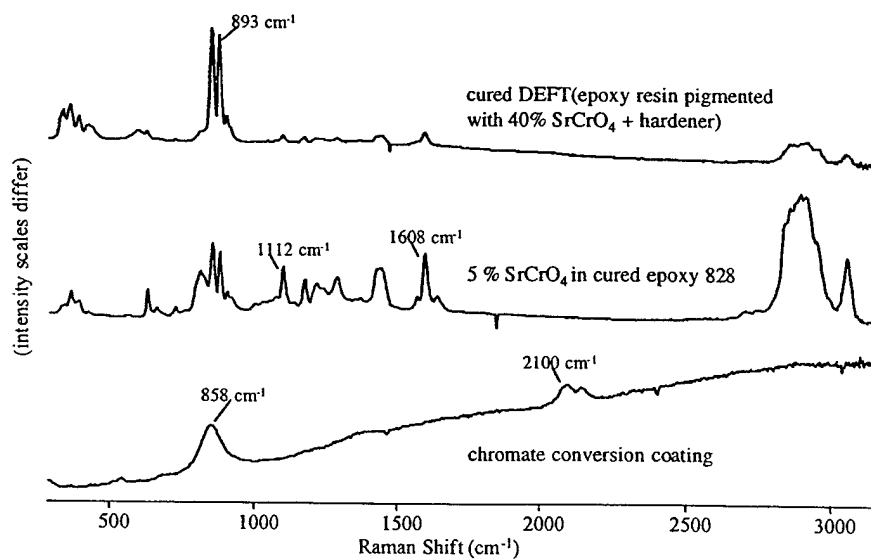


Figure 3 : Reference Raman spectra of chromate coatings.

Comparison of uncured and cured epoxy 828 (Shell).

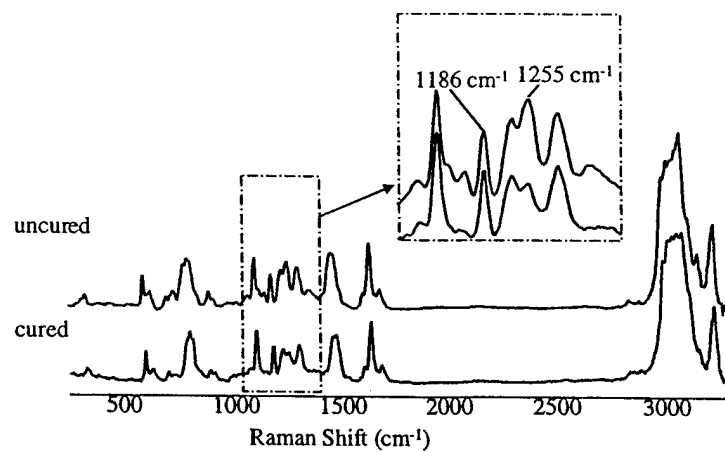


Figure 4 : Raman spectra of freshly mixed and cured (30 hours) 828 epoxy and 3141 hardener.

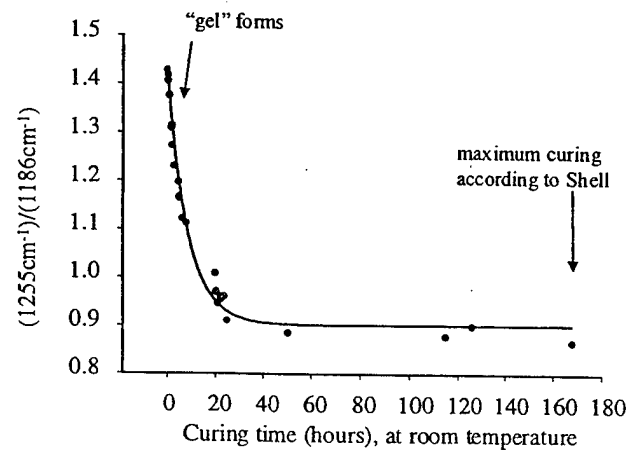


Figure 5 : Ratio of Epoxy ring ( $1255\text{ cm}^{-1}$ ) to backbone ( $1186\text{ cm}^{-1}$ ) Raman peaks during epoxy curing.

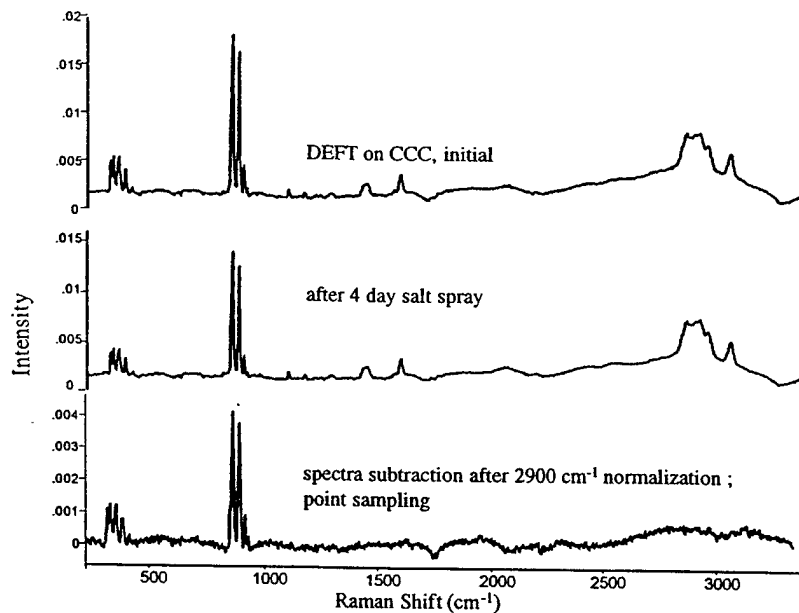


Figure 6 : Changes in Raman spectra of DEFT coating with salt spray exposure. Lower spectrum is difference between upper and lower spectra. Note intensity scale change on lower spectrum. A single point on the sample was observed

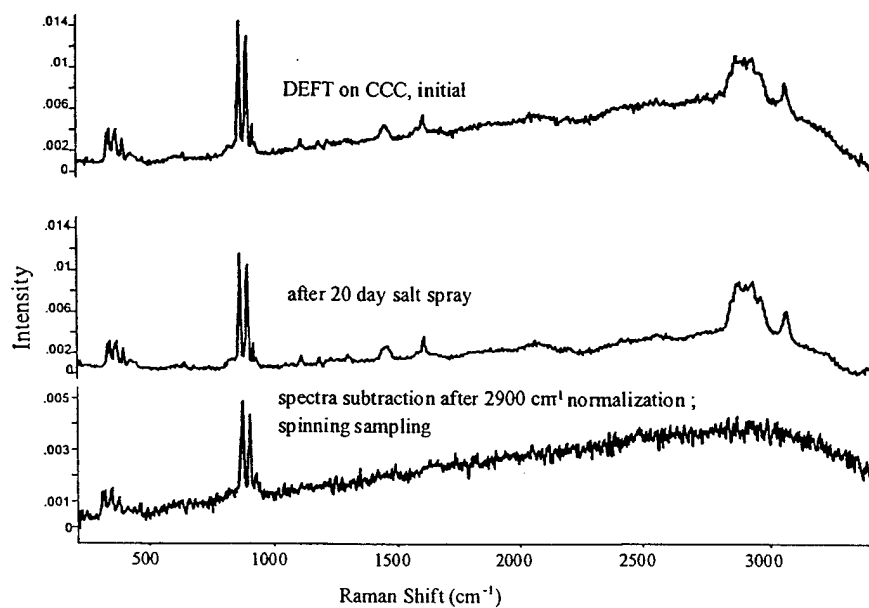


Figure 7 : Same samples as figure 6, but with the sample spinning during spectrum acquisition. 1064 nm, FT-Raman

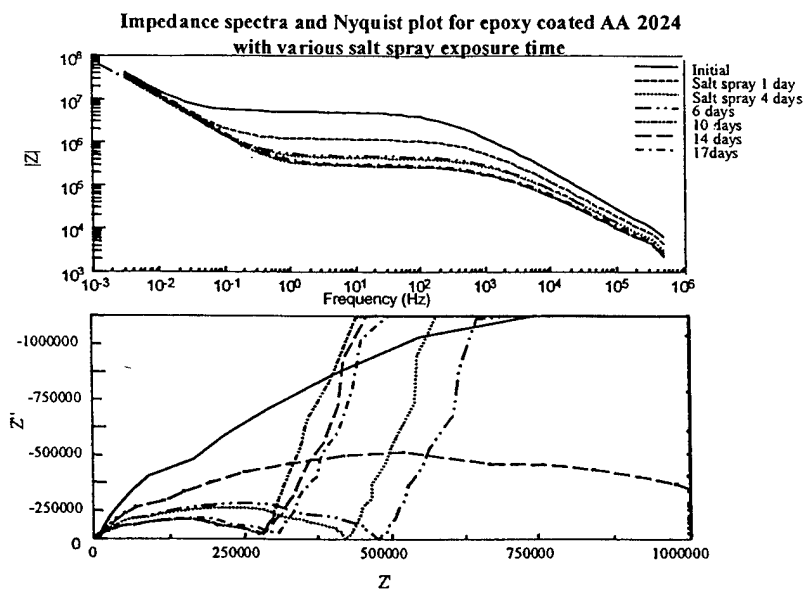


Figure 8 : Impedance results for AA 2024-T3 exposed to varying periods of salt spray.

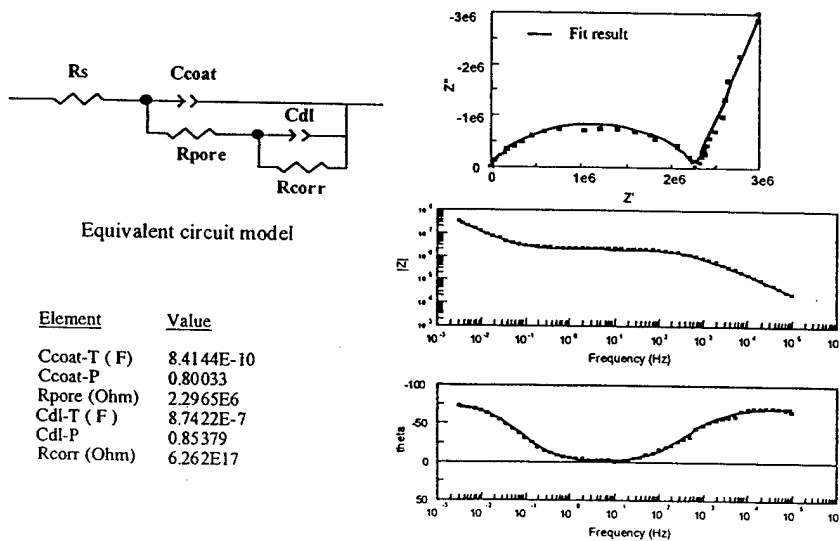


Figure 9 : Equivalent circuit model and a typical fit result of "DEFT" alloy sample. Points are experimental, lines were calculated from the model and parameters at left.

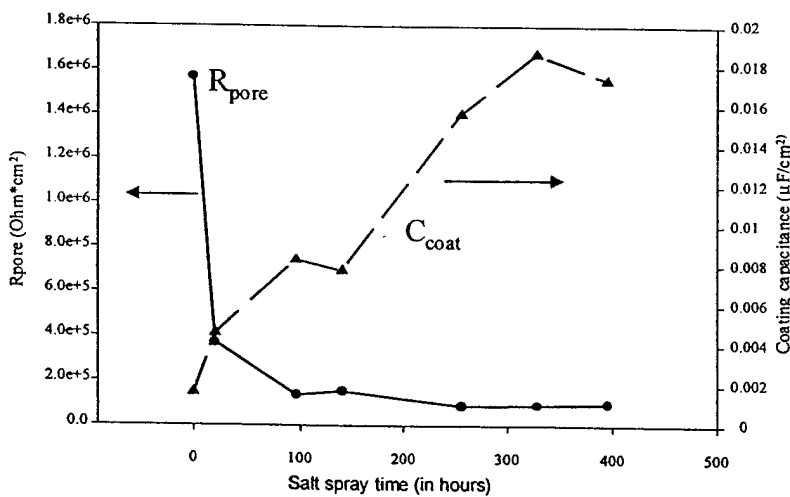


Figure 10 : Pore resistance and coating capacitance from EIS data as a function of salt spray time

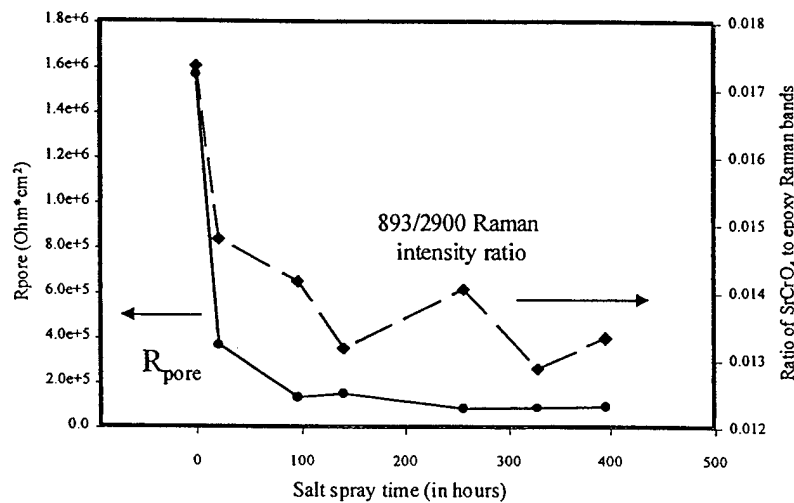


Figure 11 : Correlation of  $\text{SrCrO}_4$  to epoxy Raman peak ratio to  $R_{\text{pore}}$  from EIS as a function of salt spray time

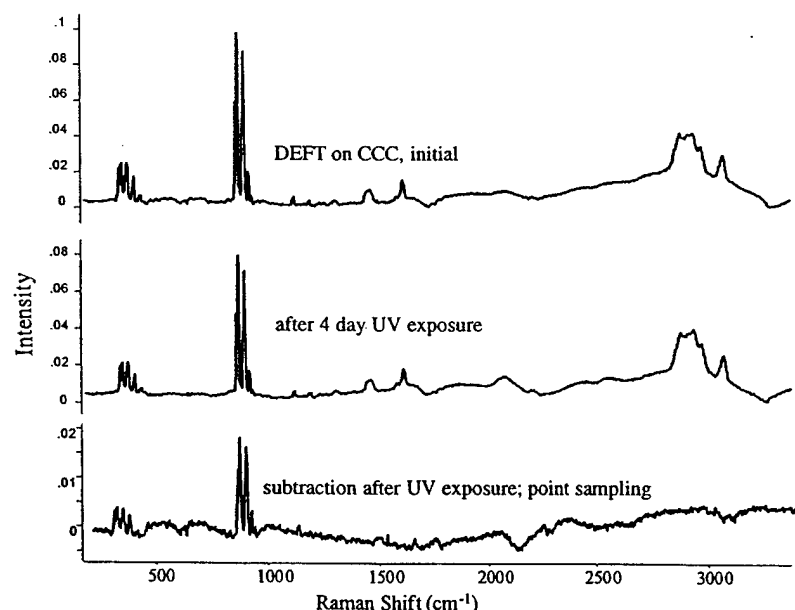


Figure 12 : Raman spectral changes accompanying UV exposure of DEFT/CCC coating on AA2024-T3. Lower spectrum is difference of initial and UV-exposed samples, with intensity scale magnified.

## **Life Prediction Tools for Corrosion Protection**

M.S.Donley, N.N.Voevodin AFRL/MLBT Air Force Research Laboratory  
Materials and Manufactory Directorate, Bld.654 2941 P Street, Wright-Patterson AFB,  
OH, Tel. (937)255-6485, FAX (937)255-2176, Michael.Donley@ml.afrl.af.mil

### **Abstract**

Accurate, predictive, and rapid accelerated corrosion tests are required life prediction tools to validate the expected corrosion protection attributes of new coating systems. Well-designed accelerated test protocols consist of four basic components. These are: 1) specimen preparation, 2) specimen damage by exposure, 3) damage evaluation, and 4) analysis of the results (1). Damage evaluation and analysis of results can be designed to serve as a "proof test" for accepting or rejecting a coating. The results can be also be correlated to field exposure to make the test results and predictor of service life. The objective of this subtask is to develop a rapid, quantitative, and predictive test to measure the corrosion protection properties of an aircraft coating system. The technical approach taken in this subtask is to utilize electrochemical, surface and molecular analyses to investigate early stages of failure and identify mechanisms. A few observations can be made from the initial results. For poor coating systems, the performance degrades fast in all exposure conditions and it doesn't matter how aggressive the environment. For good coating systems, exposure in the Prohesion Cabinet (1 hr wet/1 hr dry) for dry cycle time doesn't allow leached chromates for healing the corrosion sites, so Prohesion appears to be a more aggressive environment for the coating containing chromates, such as Alodine 1200.

### **Background**

New coatings are continuously being developed in order to meet the increasingly stringent regulations on safety, health and environment. Accelerated corrosion tests are required to validate the expected corrosion protection attributes. Standardized tests are prescribed for corrosion resistance, adhesion and electrical contact resistance in the military specifications. Corrosion protection is assessed by salt spray exposure conducted according to ASTM B117 (2). However, test methodology and data interpretation are inseparably linked to all aspects of coating research and development. How well corrosion protection mechanisms, compatibility of coating components, and expected service life are understood depends on test methods and data interpretation. A general solution to the problem of translating this test results into service life performance data as yet not been found.

Well-designed accelerated test protocols consist of four basic components. These are: 1) specimen preparation, 2) specimen damage by exposure, 3) damage evaluation, and 4) analysis of the results . Damage evaluation and analysis of results can be designed to serve as a "proof test" for accepting or rejecting a coating. The results can be also be correlated to field exposure to make the test results and predictor of service life. If, however, the accelerated test environment is sufficiently different from service

m of failure may be changed. Here, meaningful extrapolation

methods do not meet the needs for reliability, accuracy or by B.Appleman in "Survey of Accelerated Test Methods for formance" (3). The most commonly used accelerated salt spray and condensation/humidity testing, along with cular, the salt spray test is heavily relied upon to determine s often equated with corrosion resistance. The developers and er, have not produced evidence that the tests can correlate with ; importantly, predict long-term performance of protective of the studies show that salt spray does not correlate with h marine environments. There is also a lack of evidence that reproducible results from one instrument to another and one n, typical salt spray tests require more than two months time. ental methods for characterizing polymeric materials and g increasingly utilized for coatings evaluation. A few, which i potential for improving the understanding of coatings, trochemical impedance spectroscopy, electron spin resonance, infrared spectroscopy, and infrared thermography (3). Each es a different aspect of the science of evaluating, monitoring, and their application has much promise to improve the thods. In addition, accelerated corrosion tests based on these reduce the required test time.

sk is to develop a rapid, quantitative, and predictive test to ection properties of an aircraft coating system. A fundamental ll degradation processes is necessary. Test attributes include: ealing characteristics discriminating (e.g. can tell good coatings from bad ones) to be used to predict performance in service

en in this subtask is to utilize electrochemical, surface and stigate early stages of failure and identify mechanisms. sed on developing an EIS-based test technique/test protocol for

## Accomplishments

### Electrochemical Impedance Tests for Al 2024-T3 panels with Alodine 1200 Surface Treatment.

The research was performed with qualitative screening evaluation and quantitative analysis of treated aluminum panels. A series of Al 2024-T3 panels were coated by Alodine 1200 at the Coating Technology Integration Office, Wright-Patterson Air Force Base, Ohio. The focus of the evaluation was to investigate the comparative corrosion protection properties of coated panels relative to volume of electrolyte and the area of exposure. The panels were evaluated using Gamry Instruments PC3-300 Potentiostat coupled with CMS100 Corrosion Measurements System framework. Measurements were carried out between 5 kHz and 20 mHz.

The impedance measurements allow direct evaluation of the coating's capacitive and resistive nature while immersed in an electrolyte. From these impedance measurements other characteristics of the sample, such as: passivity of the coating, water uptake within the coating, and diffusion within the coating can be determined. After each experiment the impedance data were displayed as Bode and Nyquist plots (Fig.1, 2). Simple corrosion systems, which are entirely under charge transfer control and uniform corrosion on homogeneous surfaces, can be described by equivalent circuit schematics, as shown in Fig.3 (4,5).

Initial analysis of data follows the simplest circuit model. Three major characteristics of the system were considered:  $R_s$  (electrolyte resistance),  $R_p$  (Polarization resistance),  $C_c$  (coating capacitance). From EIS data, resistance of aluminum 2024-T3 panels treated with Alodine 1200 when immersed in Harrison solution is low,  $\approx 10^3$  Ohm/cm<sup>2</sup>. Solution resistance,  $R_s$ , in all series of test is very low and, therefore, it could be neglected in the circuit analyses. Polarization resistance and coating capacitance were found to depend considerably on the electrolyte volume/exposure area ratio, as well as on the exposure time. In general the polarization resistance decreased and capacitance increased with the higher ratio of electrolyte volume to the exposure area and with the exposure time (Fig.4).

Based on these data, the range of the polarization resistance variation is significant, covering an order of magnitude change in the  $R_p$  with the electrolyte volume/exposure area ratio. One possible explanation for the result is that at the lower electrolyte volumes, the concentration of active chromates leached from the Alodine coating is higher. In the smallest solution volume to surface area ratio test, the coating resistance increased with increasing exposure time (Fig.5). This behavior was not observed in any of the other samples measured, and has been reported as a behavior that indicates self healing in primer-coated metals. For larger electrolyte volume/surface area these leached chromates are distributed in larger volumes.

The diagnostic tests to simulate the rate of chromate free coating development and implementation. High strength Al 2024-T3 was selected as the test substrate. Chromate conversion coatings were again applied at CTIO (Coating Technology Integration Office), using two different procedures of time immersion in the Alodine bath: 1) 90 sec

and 2) 180 sec. Here, the choice of two immersion times would show how it affects corrosion protection properties of the coating. The "3x6" panels were wire wound rod coated with following water-based primers: Mil-P-85582 (Type N), Model Clear (W/B Epoxy), High X-Link (W/B Epoxy), Clear Epoxy with inhibitor Na-Sul 412. A listing of the 8 selected coatings and a make-up of their primer components is presented in Table 1.

Three different exposure conditions were chosen as the environment for the test: Prohesion™ (temperature cycling and alternate wet and dry cycling using dilute Harrison's solution as electrolyte), Salt-Spray (constant spray of 5 wt.% NaCl solution,) and constant immersion in Reg. Harrison's solution. EIS measurements were performed after 1 hr, 170 hrs, 340 hrs and 502 hrs exposure. The impedance data were displayed as Bode and Nyquist plots (Fig.6-13). Visual assessments and correlation with EIS data are provided in Table 2.

The Bode plot is a graphical representation of the impedance modulus, Z-modulus, vs. log of the frequency, log f. If the graph is horizontal (low-frequency plateau), the impedance of the system is independent of frequency and therefore only exhibits resistive behavior. The slope on the graph suggests the presence of the capacitive component in the system. The point on the graph at 3dB below the plateau where the line changes the slope is termed the breakpoint frequency. The impedance modulus represents the total impedance contribution whether it is capacitive, resistive or a combination of thereof. The higher the impedance modulus, the better the protective properties of a given coating system. The Nyquist plot is a graphical representation of real impedance (in phase), vs. imaginary impedance (out of phase).

Analysis of EIS data of coating systems (four different primers) shows that coating with Mil SPEC 85582 Type N Primer had low resistance in all exposure conditions (5%NaCl Salt Spray, Prohesion Cabinet and constant immersion in Reg. Harrison solution (Fig.6-9). If compare electrochemical behavior of this coating for exposure conditions we can conclude that it is more complex in Prohesion Cabinet conditions (Fig.8, 9). As indicated in the plots, a breakdown of the coating occurred 168 hrs after initial exposure. And for the 336hrs and 504 hrs exposure Nyquist plot indicates the diffusion limited processes (Fig.9). Visual signs of corrosion were noticeable on the coatings after exposure in Prohesion Cabinet and Salt Spray Chamber.

Overall, the coating system with clear water based epoxy primer demonstrated better corrosion resistance (Fig.10-12). The low-frequency value stayed between  $1 \cdot 10^7$ - $1 \cdot 10^8$  Ohm·cm<sup>2</sup> after 504 hrs of exposure. For systems tested according Salt Spray and constant immersion protocols, Zmodulus increased after 170 hours compared to the initial values. However, for the Prohesion system, no increase in the low-frequency modulus was observed. Moreover, the increase of Zmodulus appears to be the greatest in the case of the constant immersion, when the system is exposed to large amounts of electrolyte, and appears to be somewhat smaller for the Salt Spray test, in which case the system is exposed to smaller amounts of electrolyte (mist). Finally, the modulus showed no increase after 170 hrs in the Prohesion test, where the exposure conditions alternate between 1 hour salt fog and 1 hour dry cycle. The behavior of the low-frequency

modulus can be rationalized if we consider the relationship between the amount of electrolyte in contact with the surface and the time of contact. In order for chromates to leach out of Alodine to inhibit corrosion, they have to be hydrated first. Constant immersion conditions may accelerate the attack, but at the same time the transport of chromates to the area where corrosion is taking place will be facilitated to the greater degree than in the case of the Salt Spray exposure. Therefore, the chromate inhibition may be faster and more efficient in the case of constant immersion. In Prohesion testing, where only limited amount of electrolyte is available to the system and for shorter time, chromates may fail to work at all, hence the absence of modulus increase in the EIS spectrum. No visual sign for coating system in constant immersion, but for Prohesion and for Salt Spray exposure some signs of moderate corrosion. The results seem to show no correlation with the EIS data. However, upon further investigation, it may be argued that constant immersion systems show no signs of degradation due to the more effective chromate inhibition as described above.

In conclusion, a few observations can be made. For poor coating systems, the performance degrades fast in all exposure conditions and it doesn't matter how aggressive the environment. For good coating systems, exposure in the Prohesion Cabinet (1 hr wet/1 hr dry) for dry cycle time doesn't allow leached chromates for healing the corrosion sites, so Prohesion appears to be a more aggressive environment for the coating containing chromates, such as Alodine 1200.

## References

1. Federal Test method Standard No141C, "Paint, varnish, Lacquer and related Materials Methods of Inspection, Sampling and Testing", Methods 6301.2 "Adhesion (Wet) Tape Test", January (1986).
2. ASTM B117-90, "Standard Method of Salt Spray (Fog) Testing" ASTM, Philadelphia, PA (1990).Bernard R.Appleman, Journal of Coatings Technology, 1990, vol.62, No787.
3. Mansfeld F., Shin H., Greene H. Analysis of EIS data for corrosion processes/ ASTM (PCN) 04-011880-27, ASTM Special Technical Publication, 1993.
4. Principles and prevention corrosion/ Denny A.Jones – 2 nd ed, 1996

**Table 1.** Sample Identification.

Identification Number	CCC	Primer	Exposure Conditions
1-1	Alodine(90sec)	Mil-P-85582 Type N	5%NaCl Salt Spray
1-5	Alodine(90sec)	Model Clear W/B Epoxy	5%NaCl Salt Spray
1-4	Alodine(90sec)	High X-Link W/B Epoxy	5%NaCl Salt Spray
1-7	Alodine(90sec)	Clear Epoxy w/NaSul 412	5%NaCl Salt Spray
4-1	Alodine(180sec)	Mil-P-85582 Type N	5%NaCl Salt Spray
4-5	Alodine(180sec)	Model Clear W/B Epoxy	5%NaCl Salt Spray
4-4	Alodine(180sec)	High X-Link W/B Epoxy	5%NaCl Salt Spray
5-7	Alodine(180sec)	Clear Epoxy w/NaSul 412	5%NaCl Salt Spray
2-1	Alodine(90sec)	Mil-P-85582 Type N	Dil.Harrison Prohesion
2-5	Alodine(90sec)	Model Clear W/B Epoxy	Dil.Harrison Prohesion
2-4	Alodine(90sec)	High X-Link W/B Epoxy	Dil.Harrison Prohesion
2-7	Alodine(90sec)	Clear Epoxy w/NaSul 412	Dil.Harrison Prohesion
5-1	Alodine(180sec)	Mil-P-85582 Type N	Dil.Harrison Prohesion
5-5	Alodine(180sec)	Model Clear W/B Epoxy	Dil.Harrison Prohesion
5-4	Alodine(180sec)	High X-Link W/B Epoxy	Dil.Harrison Prohesion
6-7	Alodine(180sec)	Clear Epoxy w/NaSul 412	Dil.Harrison Prohesion
3-1	Alodine(90sec)	Mil-P-85582 Type N	Reg.Harrison Immersion
3-5	Alodine(90sec)	Model Clear W/B Epoxy	Reg.Harrison Immersion
3-4	Alodine(90sec)	High X-Link W/B Epoxy	Reg.Harrison Immersion
3-7	Alodine(90sec)	Clear Epoxy w/NaSul 412	Reg.Harrison Immersion
6-1	Alodine(180sec)	Mil-P-85582 Type N	Reg.Harrison Immersion
6-5	Alodine(180sec)	Model Clear W/B Epoxy	Reg.Harrison Immersion
6-4	Alodine(180sec)	High X-Link W/B Epoxy	Reg.Harrison Immersion
4-7	Alodine(180sec)	Clear Epoxy w/NaSul 412	Reg.Harrison Immersion

**Table 2.** Correlation between visual observation and EIS data.

COATING SYSTEM	CONSTANT IMMERSION Harrison's Solution		PROHESION CABINET Dilute Harrison's Solution		SALT FOG CHAMBER 5% Sodium Chloride	
	Visual	EIS Data (after 504 hrs)	Visual	EIS Data (after 504 hrs)	Visual	EIS Data (after 504 hrs)
Primer: MIL SPEC 85582 Type N CCC: Alodine (90) Alodine (180)	OK, Single Blister OK, No Blisters	Fair Fair	OK, No Blisters OK, No Blisters	Fair Fair	Blisters OK, No Blisters	Fair Fair
Primer: Clear W/B Epoxy Primer CCC: Alodine (90) Alodine (180)	OK, Hazy Spots Corrosion Spots	Good Fair	OK, No Blisters OK, No Blisters	Good Good	OK, No Blisters OK, No Blisters	Good Good
Primer: High X-Link Clear Primer CCC: Alodine (90) Alodine (180)	OK, Lt. Hazy Spots OK, Lt. Hazy Spots	Good Fair	OK, No Blisters OK, No Blisters	Good OK	OK, No Blisters OK, No Blisters	Good Fair
Primer: Clear Primer w. Na-Sul Alodine (90) Alodine (180)	OK, Hazy Spots Corrosion Spots	Good Good	OK, No Blisters OK, No Blisters	Fair Fair	OK, No Blisters OK, No Blisters	Good Good

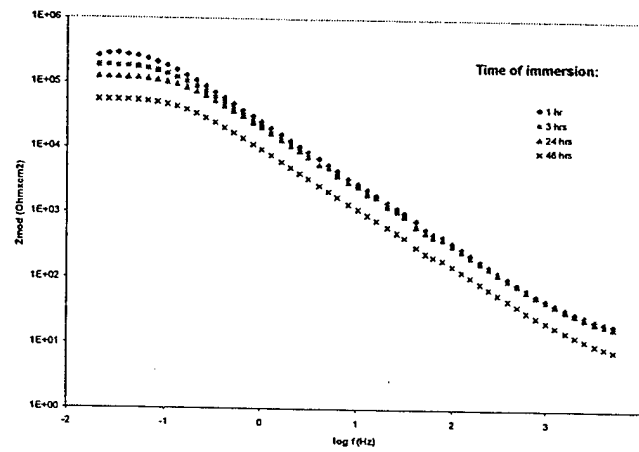


**Figure 1.** Bode plot of Al 2024-T3 substrate coated Alodine 1200 after constant immersion in Reg. Harrison solution (ratio volume/area: 100ml/10cm<sup>2</sup>).

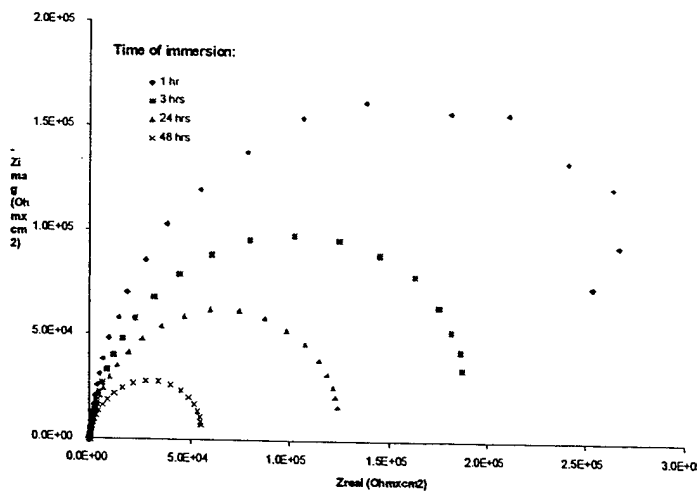


**Figure 2.** Nyquist plot of Al 2024-T3 substrate coated Alodine 1200 after constant immersion in Reg. Harrison solution (ratio volume/area: 100ml/10cm<sup>2</sup>).

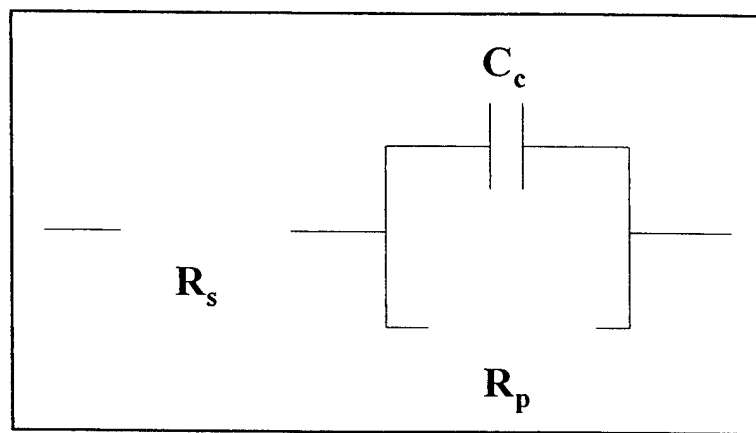


**Figure 3.** Equivalent Circuit Schematics.

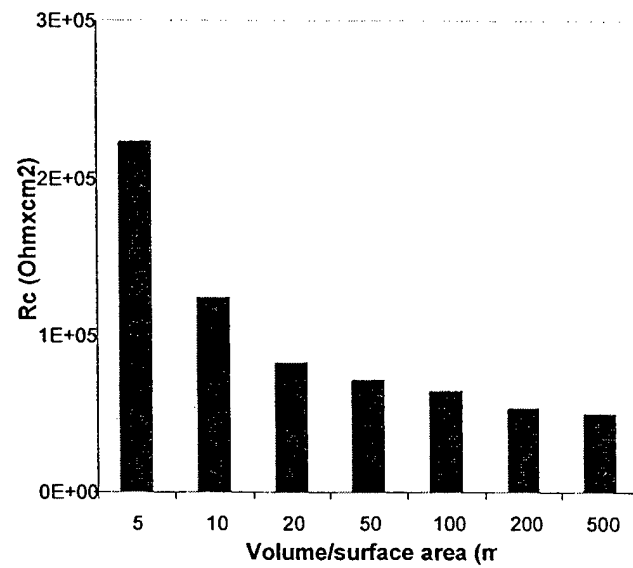


**Figure 4.**  $R_c$  vs Ratio volume to surface area (exposure time - 24 hrs).

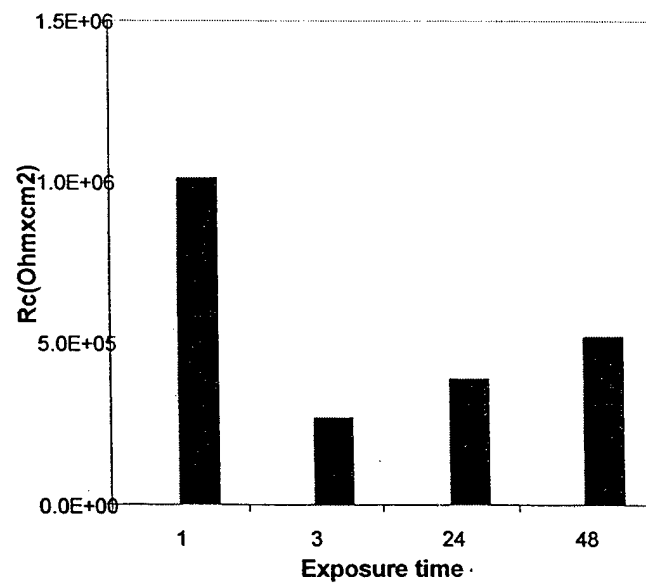


**Figure 5.**  $R_c$  vs Exposure time (ratio volume to surface area - 5 ml/cm<sup>2</sup>).

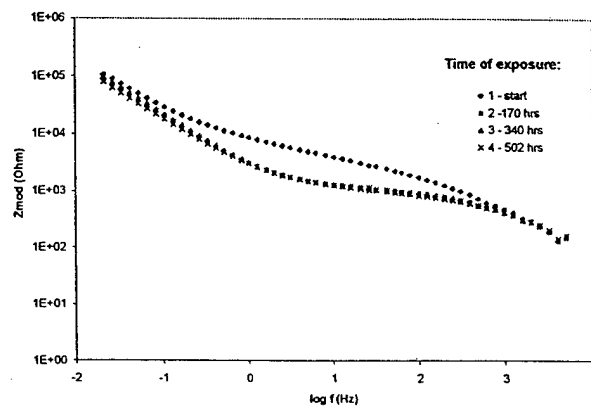


**Figure 6.** Bode Plot of Coating System 1-1: Alodine(90)+ MIL-P-85552 in 5% NaCl Salt Spay.

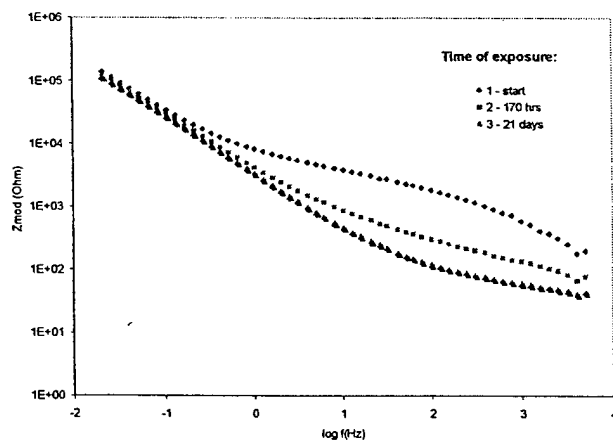


**Figure 7.** Bode Plot of Coating System 3-1 Alodine(90)+MIL-P-85582 in Reg.Harrison Constant Immersion.

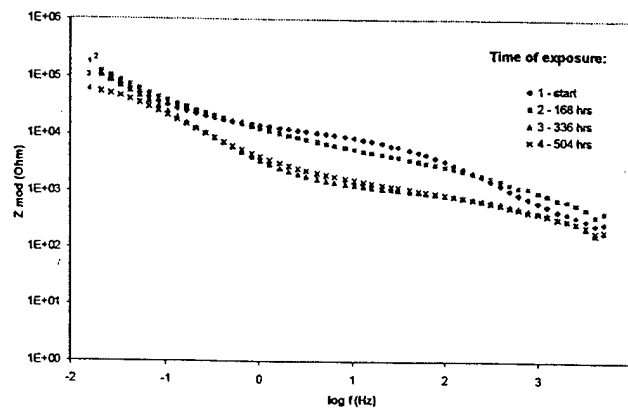


**Figure 8.** Bode Plot of Coating System 2-1 Alodine(90)+MIL-P-85582 in Prohesion Cabinet.

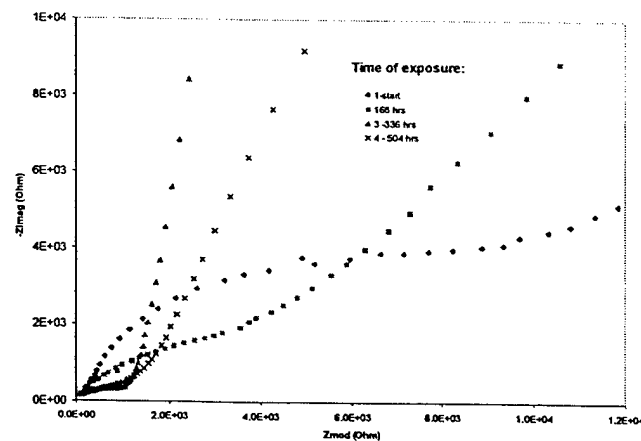


**Figure 9.** Nyquist Plot of Coating System 2-1 Alodine(90)+MIL-P-85582 in Prohesion Cabinet.

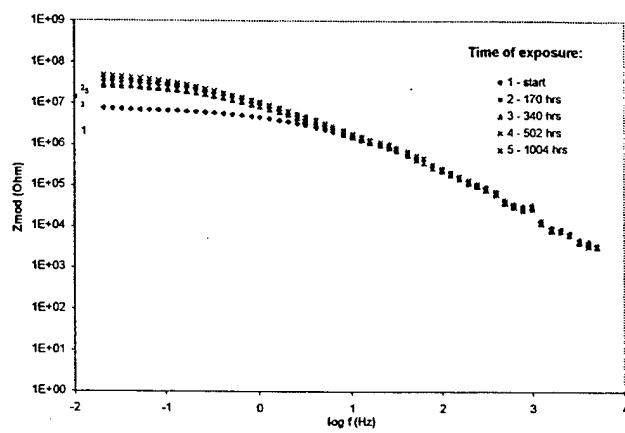


**Figure 10.** Bode Plot of Coating System 2-1 Alodine(90)+Clear W/B Epoxy Primer in Salt Spray Chamber.

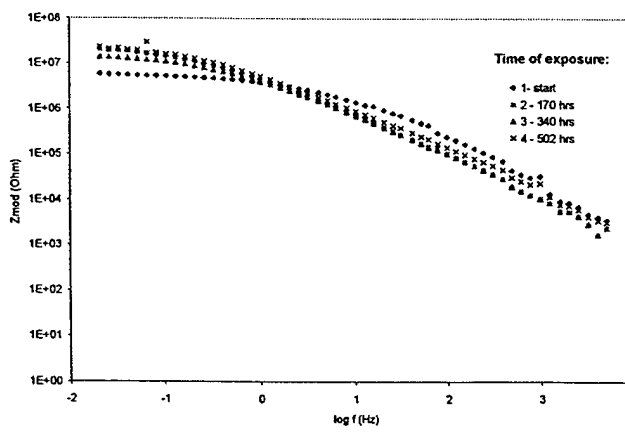


**Figure 11.** Bode Plot of Coating System 4-5 Alodine(180) + Clear W/B Epoxy Primer in Salt Spray Chamber.

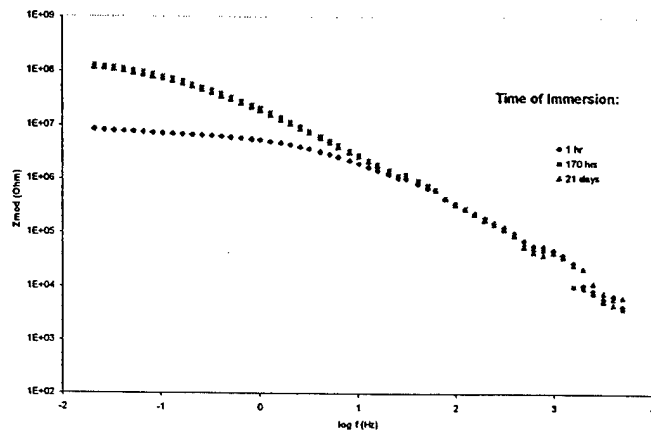


**Figure 12.** Bode Plot of Coating System 3-5 Alodine(90)+Epoxy Primer Clear W/B Epoxy Primer in Reg.Harrison constant immersion.

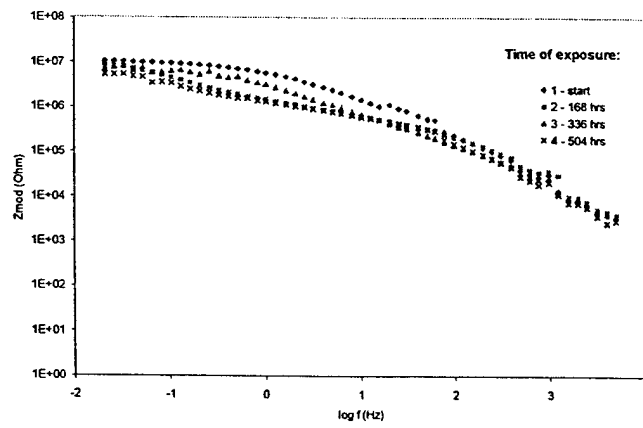


**Figure 13.** Bode Plot of Coating System 2-5 Alodine(90)+Epoxy Primer Clear W/B Epoxy Primer in Prohesion Cabinet.

## **Advanced Diagnostic Methods**

J. H. Beatty , P. F. Buckley, Metals and Ceramics Research Branch, Weapons and Materials Research Directorate, Army Research Laboratory, Tel: (410) 306-0869, Fax: (410) 306-0829, [jbeatty@arl.mil](mailto:jbeatty@arl.mil)

### **Background**

Chromate conversion coatings have been extensively employed in the preparation of aluminum surfaces prior to paint application for use in corrosive environments such as are seen in military service. Prior to determining a more environmentally benign solution to the hexavalent chrome present in chromate solutions it must be determined how chromate conversion coatings have been able to perform satisfactorily. There are two suspected mechanisms of protection. One is the corrosion inhibitive qualities inherent in the chromate conversion coating, another is the rough surface formed which may allow for greater adhesion of the primer and topcoat. Both these mechanisms play a role in prolonging the life of the coated aluminum system in a corrosive environment. However, it is necessary to delineate their respective contributions to the success/failure of the coated aluminum system in order to create a environmentally acceptable replacement with comparable performance. Although numerous studies have successfully discovered the mechanisms of corrosion inhibition [1-5], very little has been done to delineate the adhesion effect .

### **Objective**

Delineate the influence of adhesion from the influence of corrosion on the failure of chromate conversion coated aluminum systems.

### **Technical Approach**

There is data available on the performance of chromated aluminum armor alloys in various accelerated corrosion tests [6-8]. The Army has been interested in aluminum armor alloys such as 2519, 5083 and 7039. Accelerated test methods such as ASTM B117 and GM 9540P have been used. Additionally, both dry and wet adhesion data are also available for chromated aluminum alloys. These data were revisited to examine the adhesion performance on the respective alloys in comparison to the corrosion performance as tested in accelerated testing environments.

Additionally, a more precise method must be developed to purposely distinguish the adhesion ability from the corrosion inhibitive ability of chromated aluminum. Wet adhesion, cathodic disbonding, peel testing and electrochemical impedance spectroscopy (EIS) will all be preformed after immersion in various solutions of different degrees of corrosivity. The resultant data matrix should enable differentiation between pure adhesion and pure corrosion related mechanisms as well as discovery of any coupling between the mechanisms.

## Accomplishments

Approximately 20 panels each of 2519, 5083, 6061 and 7039 aluminum were prepared. Half the panels were treated with Alodine 1200 and half were grit blasted to a 2-4 mil profile. The grit blasted surface was assumed to provide good adhesion properties without any extra corrosion resistance per se. The chromate conversion surface was assumed to provide some combination of improved adhesion and corrosion resistance. All panels were subsequently coated with Mil-P-53022 Primer and Mil-C-46168 topcoat.

Salt fog testing in accordance with ASTM B117 [9], MIL-C-81706 [10] and MIL-C-5541E [11] was used. The solution was the standard 5% NaCl. Painted panels (3 each) for each conversion coating/alloy combination were exposed for 2000 hours of saltfog. These panels were "X" scribed using a standard carbide tipped hardened steel scribe. Figure 1 shows a representative photo of initial specimen appearance after scribing (all the painted panels appeared visually identical before testing). Periodic observations were made and damage was assessed chronologically using a series of ratings based upon scribe corrosion, blistering, and any delamination or lifting of the paint from the substrate (Table 1.) Final detailed ratings for the 2000 hour duration were assessed using ASTM D1654A which quantitatively measures the damage caused by pitting or delamination outwards from the scribe (Table 2.)

A cyclic corrosion test chamber (CCTC) was used to evaluate painted test panels. For each alloy/conversion coating combination tested, 5 panels primed and topcoated were subjected to CCTC testing. As in saltfog, the panels were "X" scribed. The scribed panels were placed into the chamber and tested using GM Standard Test 9540P, Method B [12] to provide a more realistic accelerated environmental test than conventional salt fog. The standard 0.9% NaCl, 0.1%CaCl<sub>2</sub>, .25% NaHCO<sub>3</sub> test solution was used. In addition, standard plain carbon steel calibration coupons described in GM Standard Test 9540P and supplied by GM were initially weighed and subsequently monitored for mass loss at intervals set by the specification. The 9540P test consists of 18 separate stages which include the following: saltwater spray, humidity, drying, ambient, and heated drying. The environmental conditions and duration of each stage for one complete 9540P cycle are given in Table 3. Again, the panels were photographed or digitally scanned prior to testing, upon significant observations, and at the suspension of the testing (120 cycles). As with B117 saltfog, damage was assessed both chronologically and at the conclusion of exposure using the same methods.

Paint adhesion for both primed and topcoated panels was determined using a wet adhesion test (Method 6301 of standard MIL-C-81706 [13].) In this test, a standard adhesive tape is used to check adhesion on painted specimens after soaking for 24 hours in deionized water. After soaking, each panel is removed and then quickly dried. Two parallel scribes one inch apart are made within the first minute after removal. Tape is uniformly applied across the scribes and then immediately removed. Upon removal, any evidence of paint separation is noted by visual observation of both the panel and the tape. MIL-C-81706 describes adhesion based on a pass or fail system. To receive a "pass" rating, there must be no separation of the paint from the substrate or between layers of the paint. Additionally, a more detailed rating in accordance with ASTM D-3359A [14] was used (Table 4.)

Dry adhesion in accordance with ASTM D-3359B [14] was performed. This method employs a 6 X 6 grid of perpendicular scribes spaced at 2 mm intervals. Standard tape as similarly used in wet adhesion is uniformly applied over the cross-hatched area and then immediately removed. Once again, upon removal, any evidence of paint separation is noted by visual observation of both the panel and the tape. The rating method for ASTM D-3359B is described in detail. (Table 5)

Results for the GM 9540P testing (Figure 1.) show little difference between chromated and grit blasted specimens for the 5083 alloy. However, the chromating resulted in marked improvement for the 2519 and 7039 alloys. The 6061 alloy performed equally well with grit blasting and chromating. Results from the ASTM B117 test (Figure 2.) show significant difference between grit blasted and chromated performance. This may be due to the constant wet condition of this test where a corrosion inhibitor is necessary. GM 9540P may interrogate adhesion more severely due to its cyclic nature without as severe corrosion conditions as B117. This would be more favorable to a pretreatment that provided some adhesion promotion with no corrosion retardation. One might argue that the dominant failure mechanism for 5083 and 6061 in the GM 9540P test is loss of adhesion while the failure mechanisms for 2519 and 7039 are a combination of adhesion reduction and corrosion.

The wet adhesion results (Figure 3.) are virtually identical for the grit blasted versus the chromated specimens. The dry adhesion results (Figure 4.) show little difference for the grit blasted versus chromated 7039 while showing slight improvement for the grit blasted 5083 over the chromated 5083. All the dry adhesion results for the 6061 alloy are very poor.

The results seem to indicate that the copper containing alloys show improved corrosion resistance and adhesion for the chromated specimens over the grit blasted specimens. The 5083 and 6061 alloys show less difference between the two treatments except in the case of extended testing under constant wet conditions as present in the ASTM B117 test. Also, one might conclude from the GM 9540P and the adhesion results that grit blasting is an adequate pretreatment for 5083 aluminum. Although these results indicate that chromating has a significant adhesion effect, more extensive testing is needed to better quantify this effect.

Wet adhesion, cathodic disbonding, peel testing and electrochemical impedance spectroscopy (EIS) will all be performed on the test panels mentioned previously after immersion in various solutions of different degrees of corrosivity. This will be done to better distinguish the respective influences of adhesion and corrosion resistance on the longevity of chromated aluminum alloys under corrosive conditions.

## References

1. P. Schmutz and G.S. Frankel, "Characterization of AA 2024-T3 by Scanning Kelvin Probe Force Microscopy", *J. Electrochem. Soc.*, 145, 2285 (1998).
2. P. Schmutz and G.S. Frankel, "Corrosion Study of AA 2024-T3 by Scanning Kelvin Probe Force Microscopy and In Situ AFM Scratching", *J. Electrochem. Soc.*, 145, 2295 (1998).
3. J. Zhao, G.S. Frankel, and R.L. McCreery, "Corrosion Protection of Untreated AA 2024-T3 in Chloride Solution by Chromate Conversion Coating Monitored with Raman Spectroscopy", *J. Electrochem. Soc.*, 145, 2258 (1998).
4. L. Xia and R.L. McCreery, "Chemistry of a Chromate Conversion Coating on Aluminum Alloy AA2024-T3 Probed by Vibrational Spectroscopy", *J. Electrochem. Soc.*, 145(1), L11 (1998).
5. K. Shimuzu, G.M. Brown et al, "Ultramicrotomy- A Route Towards the Enhanced Understanding of the Corrosion and Filming Behaviour of Aluminum and Its Alloys", *Corrosion Science*, V40, No. 7, 1049, (1998).
6. B. Placzankis, J. Beatty, J. Kelley, L. Krebs, "Evaluation of Non-Chromate Conversion Coatings on Aluminum Armor Alloys" NACE Paper No. 532, 1997Our NACE Paper.
7. B. E. Placzankis, C. E. Miller and J. H. Beatty, "Accelerated Corrosion Analysis of Aluminum Armor Alloy 2519 With Nonchromate Conversion Coatings for DoD Applications", Proceedings 1999 Corrosion Technology Symposium, Louisville, KY, (1999).
8. B. E. Placzankis, C. E. Miller and J. H. Beatty, "Accelerated Corrosion Analysis of Aluminum Armor Alloys With Nonchromate Conversion Coatings for DoD Applications", Proceedings 1999 TriService Corrosion Conference, Myrtle Beach, SC, in press (1999).
9. ASTM B117 - 90. "Standard Method of Salt Spray (Fog) Testing." ASTM, Philadelphia, PA. 1990.
10. MIL-C-81706. "Chemical Conversion Materials for Coating Aluminum & Aluminum Alloys." 30 June 1970. Including Interim Amendment 5. 13 November 1979.
11. MIL-C-5541E. "Chemical Conversion Coatings on Aluminum & Aluminum Alloys." 30 November 1990.
12. General Motors Engineering Standards, Accelerated Corrosion Test, GM9540P, (July 1991) pp.1-5.
13. Federal Test Method Standard No. 141C. "Paint, Varnish, Lacquer and Related Materials, Methods of Inspection, Sampling and Testing." Method 6301.2 "Adhesion (Wet) Tape Test." January 24, 1986.
14. ASTM D-3359. "Standard Test Methods for Measuring Adhesion by Tape Test." ASTM, Philadelphia, PA. 1987

**Table 1.** Chronological Accelerated Corrosion Test Rating Method for Painted Test Panels.

<u>Pass:</u>
P0 = no damage
P1 = white products in scribe from exposed substrate (no blisters)
<u>Fail:</u>
F1 = Blistering on edges of scribe
F2 = Blistering on remaining non-scribe area
F3 = Scribe and non-edge blisters
F4 = Total failure (a) Excessive large blisters. (b) Rupturing of blisters

**Table 2.** Corrosion Damage Assessment ASTM D1654A.

Millimetres	Rating of Failure at Scribe (Procedure A)	
	Representative Mean Creepage From Scribe	Rating Number
Over 0	0	10
Over 0 to 0.5	0 to 1/64	9
Over 0.5 to 1.0	1/64 to 1/32	8
Over 1.0 to 2.0	1/32 to 1/16	7
Over 2.0 to 3.0	1/16 to 1/8	6
Over 3.0 to 5.0	1/8 to 3/16	5
Over 5.0 to 7.0	3/16 to 1/4	4
Over 7.0 to 10.0	1/4 to 3/8	3
Over 10.0 to 13.0	3/8 to 1/2	2
Over 13.0 to 16.0	1/2 to 5/8	1
Over 16.0 to more	5/8 to more	0

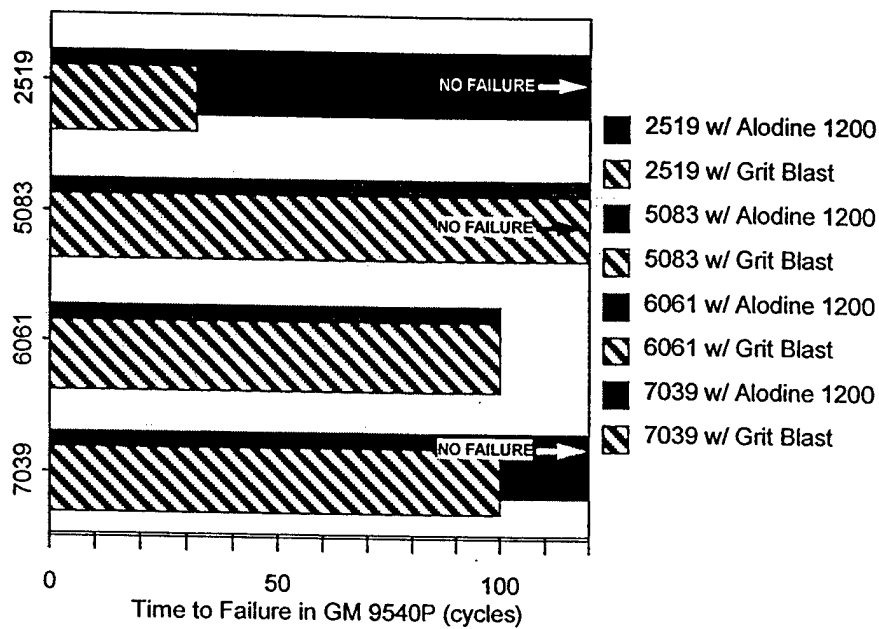
**Table 3.** GM 9540P Cyclic Corrosion Test Details.

Interval	Description	Interval Time(min.)	Temperature (°C)
1	Ramp to Salt Mist	15	25
2	Salt Mist Cycle	1	25
3	Dry Cycle	15	30
4	Ramp to Salt Mist	70	25
5	Salt Mist Cycle	1	25
6	Dry Cycle	15	30
7	Ramp to Salt Mist	70	25
8	Salt Mist Cycle	1	25
9	Dry Cycle	15	30
10	Ramp to Salt Mist	70	25
11	Salt Mist Cycle	1	25
12	Dry Cycle	15	30
13	Ramp to Humidity	15	49
14	Humidity Cycle	480	49
15	Ramp to Dry	15	60
16	Dry Cycle	480	60
17	Ramp to Ambient	15	25
18	Ambient Cycle	480	25

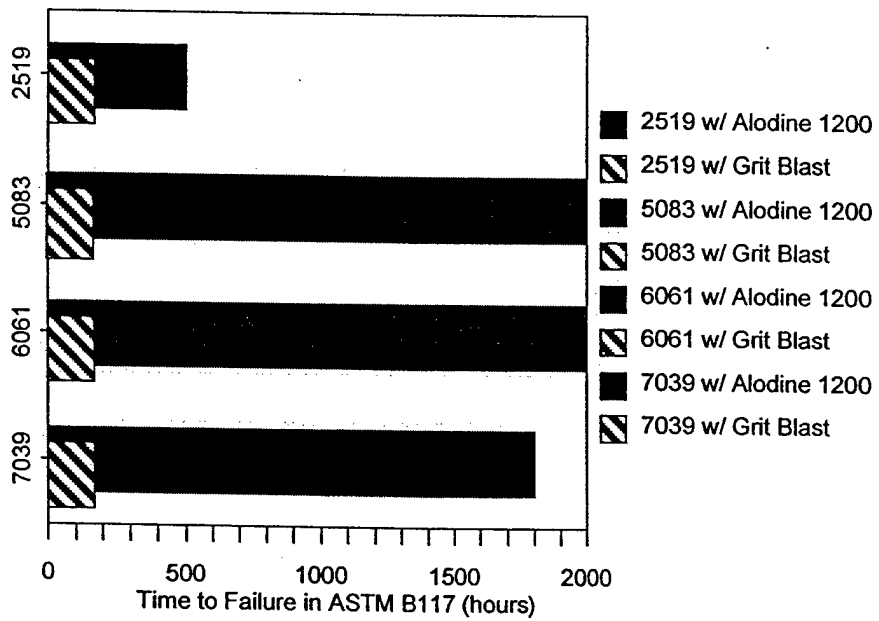
**Table 4.** Wet Adhesion Rating – Method ASTM D-3359A.

Rating	Description of Coating After Tape Removal
Method A - Wet Adhesion	
5*	No peeling or removal. (*Passes Military Performance Criteria)
4	Trace peeling or removal along scribes.
3	Jagged removal along scribes up to 1/16 in. (1.6 mm) on either side.
2	Jagged removal along most of the scribes up to 1/8 in. (3.2 mm) on either side.
1	Removal from most of the area between the scribes under the tape.
0	Removal beyond the area of the scribes.

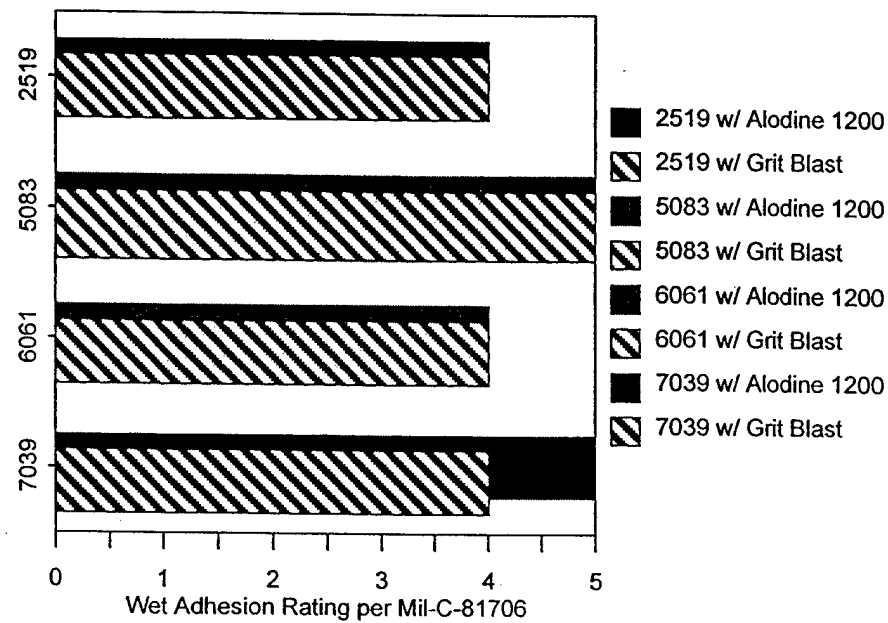
**Table 5.** Dry Adhesion Rating – ASTM D-3359B.

**Figure 1.** Time to failure as described in Table 1 for various coated aluminum panels exposed in GM 9540P testing.



**Figure 2.** Time to failure as described in Table 1 for various coated aluminum panels exposed in ASTM B117 testing.



**Figure 3.** Wet adhesion values for various coated aluminum panels according to ASTM D-3359A.

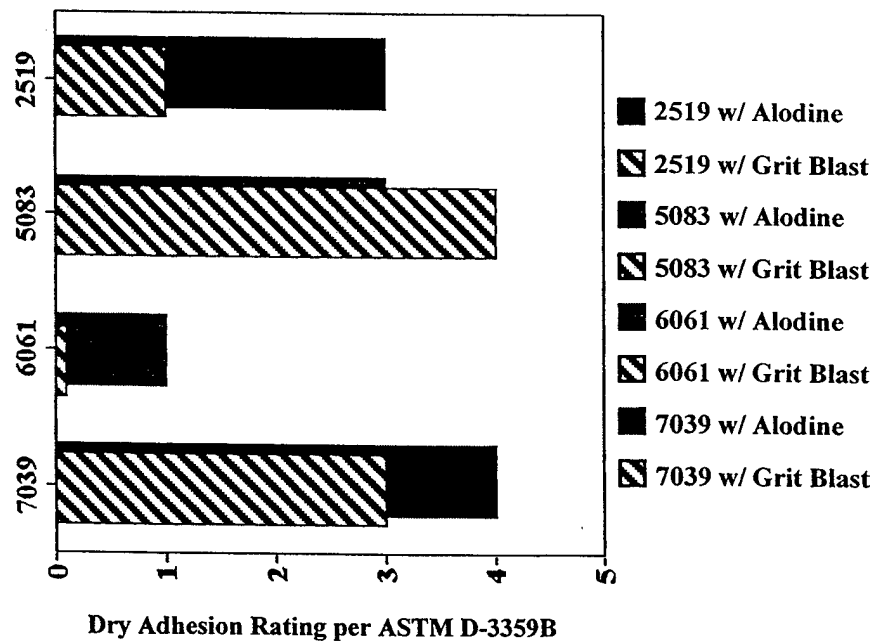


**Figure 4.** Dry adhesion values for various coated aluminum panels according to ASTM D-3359A